

Theoretical investigation of catalyst stability and deactivation

Zur Erlangung des akademischen Grades eines
DOKTORS DER NATURWISSENSCHAFTEN
(Dr. rer. nat)

von der KIT-Fakultät für Chemie und Biowissenschaften
des Karlsruher Instituts für Technologie (KIT)

genehmigte
DISSERTATION

von

Elisabeth Maria Dietze

1. Referent: Prof. Dr. Felix Studt
2. Referent: Prof. Dr. Olaf Deutschmann
Tag der mündlichen Prüfung: 09.12.2019

Abstract

Oxide supported noble metal nanoparticles are commonly used as industrial heterogeneous catalysts, for example in automotive exhaust-gas after-treatment systems. To improve their lifetime is highly important to reduce natural resource exploitation. The catalyst lifetime is limited by catalyst deactivation, in particular through sintering. In this thesis, both, the thermodynamic stability of supported nanoparticles as well as their deactivation kinetics through sintering are investigated.

First, the thermodynamic stability of pure unsupported metal nanoparticles is studied. Density functional theory (DFT) is used to examine cuboctahedral, octahedral and cubic nanoparticles of the late transition metals as well as Al and Mg in order to identify their stability as a function of size. A simple model is developed that not only includes the surface energies as in the commonly used Wulff construction but additionally accounts for energies related to edges and corners. Importantly, this model only requires the bulk cohesive energy and the surface energies of the fcc(111) and fcc(100) surfaces, which are used to extrapolate to lower coordination numbers. It is found that the model estimates the stability of nanoparticles with a mean absolute error of only 0.09 eV/atom.

To understand how the support influences the stability of metal nanoparticles, numerous metal/oxide interfaces are investigated using DFT. It is found that for a given oxide, variations in adhesion energies with different metals can be described by the adsorption energy of atomic oxygen on the corresponding metal surfaces, thus forming scaling relations similar to those used for adsorbates on metal surfaces. Variations between different oxides can be analyzed through the number of interfacial oxygen atoms that form metal-oxygen bonds. This descriptor can often be derived from the structure of the clean oxide surfaces. Adhesion of the studied interfaces, which is dominated by metal-oxygen bonds, is thus well described by a single scaling relation, using two descriptors, one for the metal and one for the oxide surface.

To describe the kinetics of sintering for particle migration and coalescence, a kinetic Monte Carlo (kMC) based model is introduced that simulates migration of differently sized Pt nanoparticles on quartz with point defects. Diffusion constants are taken from 3D-lattice DFT-based kMC from the literature. The effects of temperature, particle-size, particle-concentration and support defects are studied. To investigate the competitive effects of the two different sintering mechanisms, particle migration and coalescence and Ostwald ripening, the latter is simulated through a mean-field model within the kMC model. Under elevated temperatures and oxygen in the gas phase, Ostwald ripening, mediated by mass transfer of volatile PtO_2 between Pt particles, is found to be the dominating sintering mechanism for the investigated Pt supported on quartz catalyst.

The used mean-field model for gas phase mediated Ostwald ripening is based on assumptions for macroscopic diffusion. Here, much smaller length scales are involved, because diffusion occurs between nanoparticles. Therefore, a kMC model is developed that explicitly simulates the diffusion of single atoms or molecules in the gas phase that result from collisions with a background gas. This model accurately reproduces ideal gas properties such as the diffusion constant. In model applications, the gas phase mediated mass transfer is studied as a function of the distance between the involved surfaces. If these distances are within the mean free path, typically a micrometer or lower, continuum models based on Fick's laws deviate from the explicit simulation. The gas phase kMC model is adapted to simulate gas phase mediated Ostwald ripening to evaluate the used mean-field model and its limitations. Generally the results obtained either using the mean-field model or the kMC model are similar. Only in limiting cases, as equally sized nanoparticles, the models diverge.

Kurzfassung

Edelmetall Nanopartikel auf Oxid-Trägern werden in der Industrie als heterogene Katalysatoren genutzt, zum Beispiel in Auto-Abgaskatalysatoren. Es ist wichtig, die Lebenszeit dieser Nanopartikel zu erhöhen, um Umweltausbeutung zu verhindern. Die Katalysatorlebenszeit ist allerdings begrenzt, da durch Sintern eine Katalysator-Deaktivierung hervorgerufen wird. In dieser Doktorarbeit wird sowohl die thermodynamische Stabilität der Nanopartikel auf Trägern untersucht, als auch die Sinterungskinetik.

Im ersten Teil wird die thermodynamische Stabilität von reinen Edelmetall-Nanopartikeln untersucht. Um die Stabilität von kuboktaedrischen, oktaedrischen und kubischen Nanopartikeln, bestehend aus Übergangsmetallen und Al und Mg zu untersuchen, wird die Dichtefunktionaltheorie (DFT) genutzt. Es wird ein einfaches Modell entwickelt, welches nicht nur die Beiträge der Oberflächen berücksichtigt, wie in Wulff's Konstruktion, sondern auch die von Ecken und Kanten. Besonders ist, dass nur die Kohäsionsenergie und die Oberflächenenergien der fcc(111) und fcc(100) Oberflächen notwendig sind, um auch Oberflächenatome mit niedriger Koordinationszahl zu beschreiben. Mit dem entwickelten Modell kann die Stabilität von Nanopartikeln mit einem mittleren absoluten Fehler von 0.09 eV/Atom berechnet werden.

Um zu verstehen, wie die Stabilität der Nanopartikel zusätzlich durch den Oxid-Träger beeinflusst wird, wurden zahlreiche Metall/Oxid Grenzflächen mit Hilfe von DFT untersucht. Wird nur ein einzelnes Oxid betrachtet, so kann die Abweichung in der Adhäsionsenergie verschiedener Metalle mit der Adsorptionsenergie von Sauerstoff auf den Metalloberflächen beschrieben werden. Dies ist ähnlich zu Skalierungsbeziehungen, welche für die Beschreibung von Adsorbaten auf Metalloberflächen verwendet werden. Die verschiedenen Oxide unterscheiden sich in ihrer Sauerstoffatomanzahl auf der Oberfläche. Dies kann als Deskriptor genutzt und von reinen Oxidoberflächen bestimmt werden. Insofern kann die Adhäsion der untersuchten Grenzflächen, welche von Metall-Sauerstoff-Bindungen dominiert werden, durch eine universelle Skalierungsrelation beschrieben werden, mit einem Deskriptor für das Oxid und einem für das Metall.

Um die Kinetik von Sinterung zu beschreiben, wurde ein auf Kinetik Monte Carlo (kMC) basierendes Modell entwickelt. Dieses beschreibt die Teilchenbewegung und -verschmelzung am Beispiel von Pt Nanopartikeln auf Quarzoberflächen mit Defektstellen. Die notwendigen Diffusionskonstanten wurden aus der Literatur entnommen und basieren auf einem 3D-Gitter DFT/kMC Modell. Untersucht wurde der Einfluss von Temperatur, Teilchengröße, Teilchenkonzentration und Oberflächendefekten. Um die konkurrierenden Sinterungsmechanismen Teilchenbewegung und -verschmelzung sowie Ostwald-Reifung zu beschreiben, wurde ein adaptives kMC Modell entwickelt, in dem die Ostwald-Reifung mittels eines Mean Field Modells beschrieben wird. Bei hohen Temperaturen und Sauerstoff in der Gasphase ist Ostwald-Reifung, bei der über die Gasphase PtO_2 zwischen den Pt Nanopartikeln übertragen wird, der dominante Sinterungsmechanismus für das untersuchte Pt/Quarz System.

Das bisher genutzte Mean Field Modell für Ostwald-Reifung basiert auf Annahmen, welche für die makroskopische Diffusion gültig sind. Im Falle von Nanopartikeln ist die Längenskala allerdings deutlich kleiner. Daher wurde ein kMC-Modell entwickelt, mit dessen Hilfe die Diffusion von einzelnen Atomen oder Molekülen in der Gasphase unter Berücksichtigung von Kollisionen mit dem Hintergrundgas simuliert werden kann. Dieses Modell reproduziert die Eigenschaften eines idealen Gases, wie dessen Diffusionskonstante. Um das kMC-Modell zu testen, wird die Diffusion zwischen zwei Oberflächen abhängig von deren Abstand untersucht. Ist der Abstand kleiner als der mittlere freie Weg des untersuchten Atoms in der Gasphase, dann kommt es zu Unterschieden zwischen dem kMC-Modell und Ergebnissen, berechnet mit Kontinuitätsgleichungen basierend auf den Fickschen

Gesetzen. Im Anschluss wurde das kMC-Modell weiterentwickelt, um Ostwald-Reifung über die Gasphase zu simulieren und um die Limitierungen des bisher genutzten Mean Field Modells einschätzen zu können. Im Allgemeinen stimmen die Ergebnisse, welche mit den beiden Modellen erhalten werden überein. Nur in Grenzfällen kommt es zu Abweichungen, zum Beispiel bei gleichgroßen Nanopartikeln.

Table of contents

Abstract	i
Kurzfassung	ii
Table of contents	v
1 Introduction	1
1.1 Industrial importance of heterogeneous catalysts	1
1.2 Catalyst deactivation	2
1.2.1 Theoretical description of catalyst deactivation	3
1.2.2 Experimental detection	6
1.2.3 Concepts to improve catalyst stability	8
1.3 Scope of this thesis	8
2 Methods	11
2.1 Introduction	11
2.2 Quantum mechanical treatment of nanoparticles and surfaces	11
2.3 Density functional theory	12
2.4 Kinetic Monte Carlo	16
3 Thermodynamic stability of metal nanoparticles	19
3.1 Introduction	19
3.2 Computational details	19
3.3 Shape and size effect for the example of Pt	24
3.4 Wulff construction	25
3.5 Pure metal nanoparticle stability model	26
3.5.1 Formalism	26
3.5.2 Results	28
3.6 Conclusions	30
4 Support effects on nanoparticle stability	31
4.1 Introduction	31
4.2 Computational details	31
4.2.1 Interface models	31
4.2.2 DFT parameters	34
4.2.3 Role of van der Waals interactions	36
4.2.4 Calculation of adhesion energies	37
4.3 Effect of adhesion on nanoparticle stability	39
4.4 Model to predict adhesion energies	41
4.5 Conclusions	44

5	Combined simulation of Ostwald ripening and particle migration	45
5.1	Introduction	45
5.2	Particle migration	45
5.2.1	Particles on defect-free support	48
5.2.2	Effect of defects	49
5.3	Combined simulation	50
5.3.1	Extension of the kMC algorithm for particle migration	50
5.3.2	Results and Discussion	51
5.4	Conclusions	53
6	Gas phase diffusion model for Ostwald ripening	55
6.1	Introduction	55
6.2	Gas phase diffusion model	55
6.2.1	Method	55
6.2.2	Parameter convergence for the example of self diffusion of Ar	59
6.2.3	Diffusion between parallel walls	62
6.2.4	Diffusion between two spheres	66
6.2.5	Conclusions	68
6.3	Explicit modeling of Ostwald ripening	68
6.3.1	Ostwald ripening in a closed system	71
6.3.2	Conclusions	73
7	Final conclusions and outlook	75
8	Bibliography	77
9	Appendix	91
9.1	Extended data of thermodynamic stability of nanoparticles	91
9.2	Extended data for adhesion energy calculation	95
	List of Abbreviations	107
	Acknowledgements	108
	List of publications	109
	Eidesstattliche Erklärung	111

1 Introduction

A catalyst is defined as substance which advances a reaction by opening an additional reaction path, which has a reduced activation energy, E_a . Two different types of catalysts are distinguished, homogeneous, where the catalyst is in the same phase as the reactants and heterogeneous, where they are in different phases.¹ This thesis deals with heterogeneous catalysts.

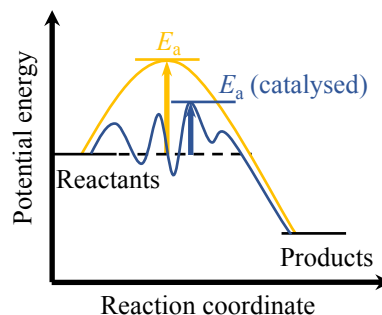


Figure 1.1: Reduction of activation energy E_a with catalyst (blue) compared to E_a without catalyst (yellow).

1.1 Industrial importance of heterogeneous catalysts

Oxide supported metal nanoparticles are commonly used as heterogeneous catalysts in industrial processes and are employed in more than 90% of chemical manufacturing processes^{2,3}. Their advantage over homogeneous catalysts is that they are easily separable from the reaction products. One important application is exhaust-gas emission control, of which a prominent example is automotive exhaust-gas after-treatment, but also coal-fired power plants⁴. Figure 1.2a shows the CO and NO_x emission of the last 30 years in Germany. Although the emission was reduced substantially, in the last 10 years the reduction in emission stagnated. To reduce emission of gases harmful for the environment, in exhaust-gas after-treatment there are mainly three important reactions: CO oxidation, NO_x reduction and hydrocarbon oxidation. Supported noble metal catalysts were found to be most active for these reactions. Underlying the importance of these catalysts, at the moment more than 50% of platinum and palladium and 80% of rhodium world's annual demand⁵ is used for their production. Figure 1.2b visualizes a typical exhaust-gas converter used in cars. Normally, the converter consists of a monolytic, alveolar ceramic or metal substrate which carries the catalytic active substance. To increase the specific surface area of the catalytic active substances, (noble metals, oxides and/or zeolites) they are impregnated on a washcoat⁶.

However, not only the activity and the selectivity towards the desired chemical reactions are significant to design suitable catalysts. Deactivation of catalysts, meaning the loss of their catalytic activity and/or selectivity over time, leads to challenging problems in their applications. The time scales of the deactivation processes are very different and can reach from a few seconds in the case of cracking catalysts to several years in ammonia synthesis^{7,8}. The deficiency in catalyst lifetime for these catalysts in application is compensated by an increased loading of noble metal material to ensure the desired catalyst performance^{9,10} over the whole lifetime. Thus, increasing the lifetime of exhaust-gas after-treatment catalysts is highly desirable to reduce the high demand of noble metals^{7,11}.

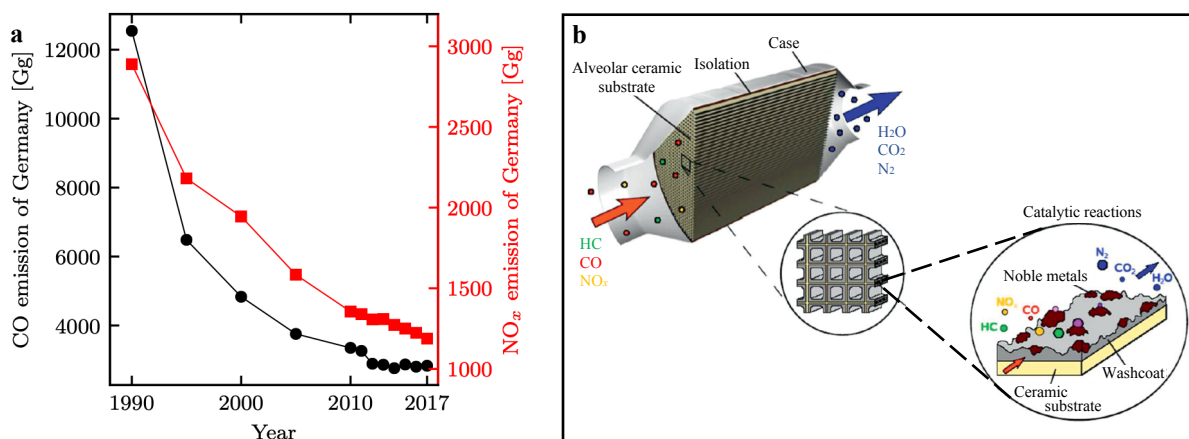


Figure 1.2: (a) CO (black line, left axis) and NO_x (red line, right axis) emission of Germany¹². (b) Reproduction from ref. 6, Copyright (2013), with permission from John Wiley and Sons: Composition of a typical exhaust-gas catalysator.¹³

1.2 Catalyst deactivation

Catalyst deactivation is caused by various chemical, mechanical and thermal processes^{7,11,14} or a combination of these. The advantage of using nanoparticles in heterogeneous catalysts is the increase in surface area per weight compared to macroscopic particles with extended surfaces. At the same time, the high surface area causes that smaller particles are less stable than larger ones. Sintering leads to the growth of larger nanoparticles by reducing the number of small nanoparticles. There are two different mechanism resulting in the observed sintering behavior, particle migration and coalescence, where entire nanoparticles diffuse over the support and form larger particles upon collision and Ostwald ripening, where fragments (atoms or molecules) from a nanoparticle dissociate. These fragments can either migrate over the gas phase or the support upon merging with another nanoparticle. These two mechanism are visualized in Figure 1.3a and b respectively, in a schematic way.

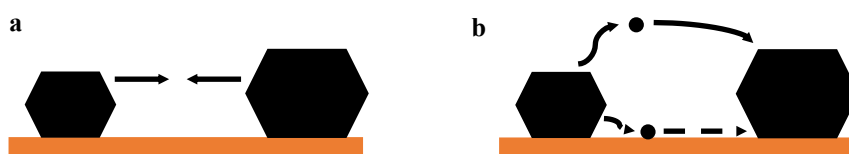


Figure 1.3: Schematic visualization of the two sintering mechanism: (a) particle migration and coalescence and (b) Ostwald ripening.

The overall effect, the loss of surface area, of these two sintering mechanism is the same, but the understanding which of these mechanism occurs in which catalytic system is important to develop strategies to prevent sintering. Ostwald ripening and particle migration and coalescence can be described theoretically and observed experimentally. Important results from the literature will be discussed in the following, with a focus on the exhaust-gas catalyst platinum.

1.2.1 Theoretical description of catalyst deactivation

Nanoparticle stability

Generally, the Gibbs-Thomson relationship is used to describe the particle size dependent stability. For the equilibrium pressure of a droplet with radius r , p_r follows:

$$p_r = p_0 \exp\left(\frac{2\gamma V_m}{rRT}\right), \quad (1.1)$$

with p_0 , the equilibrium pressure of an extended surface, γ the surface energy, V_m the molar volume, T the temperature and R the gas constant. For solid particles, it is assumed that the particle is in its equilibrium configuration according to Wulff's construction¹⁵. From this follows the exponential function:

$$\exp\left(\frac{\gamma V_m}{RT} \frac{\partial A}{\partial V}\right), \quad (1.2)$$

where $\partial A/\partial V$ is the quotient of the change in surface to volume. Using the simplification of spherical crystals:

$$V = \frac{4}{3}\pi r^3, \quad A = 4\pi r^2 \quad (1.3)$$

gives:

$$\frac{\partial A}{\partial V} = \frac{2}{r} \quad (1.4)$$

which was used in eq. (1.1). Using an effective radius $r = 2(\partial V/\partial A)$ for not dissociating compounds eq. (1.1) can be written as the first part of eq. (1.5) with c_0 the monomer concentration on the surface of an infinitely large particle. Generally the exponent in eq. (1.5) is small towards 1 and can be expanded as series from which follows:

$$c_r = c_0 \exp\left(\frac{2\gamma V_m}{rRT}\right) \approx c_0 \left[1 + \frac{2 \cdot \gamma V_m}{rRT}\right]. \quad (1.5)$$

The equilibrium concentration, c_r is the monomer concentration on the surface of a particle, at which the particle neither grows or shrinks. The approximation of the series expansion is not valid for particle sizes < 3 nm, but Wagner¹⁶ states that this particle sizes are not relevant for the observed behavior.

Eq. (1.5) can be also written for the chemical potential $\mu(r)$ of a nanoparticle with radius r :

$$\mu(r) = \mu_{\text{bulk}} + \frac{2\gamma V_m}{r}, \quad (1.6)$$

with μ_{bulk} , the chemical potential of the bulk material ($r \rightarrow \infty$). As already pointed out by Wagner¹⁶, also Campbell and coworkers¹⁷⁻²⁰ found that the Gibbs-Thomson equation is not a good approximation in the limit of small particles.

Parker et al.¹⁹ analyze the limitations of the series expansion in eq. (1.5) in detail. They particularly question the assumption of constant γ over all particle sizes, especially for $r < 3$ nm. It is suggested to use either a function $\gamma(r)$ or a different expression for the chemical potential. Nanoparticles with $r < 3$ nm have a larger fraction of low coordinated surface atoms compared to larger nanoparticles. Thus γ is expected to increase strongly with decreasing particle size.

To take into account metal/support adhesion, E_{adh} , Hemmingson and Campbell²¹ introduced a more accurate formula:

$$\mu(r) = \mu_{\text{bulk}} + (3\gamma - E_{\text{adh}}) \frac{V_m}{r}. \quad (1.7)$$

Both, eq. (1.6) and (1.7) show that larger particles, with lower chemical potential are thermodynamically preferred over smaller particles with higher chemical potential. In eq. (1.7), strong metal/support adhesion lead to an increase of the chemical potential and thus a thermodynamic stabilization of the particles. Beside the metal/support interaction, also local strain in the metal particles or different growth velocities depending on the crystal facets might change this stability-size correlation.

Ostwald ripening

The classical ripening model was developed by Lifshitz and Slyozov²² and by Wagner¹⁶ motivated by the formation of grains in a super-saturated solution. They used the Gibbs-Thomson equation after which small droplets have a higher vapor pressure or solubility in the surrounding medium than larger droplets. Thus, a transport of matter from the small droplets towards the larger ones is observed. Assuming an initial particle size distribution (PSD) of droplets in the form of a narrow Gaussian function, Lifshitz, Slyozov²² and Wagner¹⁶ derived equations that describe the time development of the PSD function, the mean particle size and the total number of particles. They assumed that the agglomeration of the droplets themselves and their spatial distribution is negligible. Eq. (1.5) in the series expansion form was used. In the model, two limiting cases were identified. In the first case, mass transport is diffusion limited and in the second case reaction limited. The change in molar number \dot{n} of one particle with the surface A was defined as:

$$\dot{n} = -4\pi r^2 k(c_r - c'_r), \quad (1.8)$$

with c'_r the actual concentration on the particle surface and k the velocity constant of the mass transfer, which can be either inhibited or not. In the case of $k\bar{r} \gg D$ (with \bar{r} the mean particle radius and D the diffusion constant) the mass transport is diffusion limited and the time evolution of $\bar{r}(t)$ is proportional to:

$$\bar{r}(t) \propto t^{1/3} \quad (1.9)$$

The case $k\bar{r} \ll D$ is reaction limited and the time evolution of $\bar{r}(t)$ is proportional to:

$$\bar{r}(t) \propto t^{1/2}. \quad (1.10)$$

Lifshitz, Slyozov²² and Wagner¹⁶ pointed out that because of the different powers in eq. (1.9) and eq. (1.10) the growth mechanisms could be experimentally distinguished, but in principle both mechanisms could be equally relevant, which was observed by Wynblatt and Gjostein²³. They concluded that experimental results²⁴ does not agree with the proposed range of the exponent, because values larger than 4 were observed and also a time dependence of the exponent.

Thus, Wynblatt and Gjostein²³ revisited the Ostwald ripening model described previously. Instead of distinguishing between diffusion and reaction limited Ostwald ripening, Wynblatt and Gjostein²³ distinguished between three different diffusion cases: vapor phase diffusion, substrate surface diffusion and substrate volume diffusion. Because the substrate volume diffusion is not likely to dominate the Ostwald ripening, they didn't considered this diffusion process further. Wynblatt and Gjostein²³ found that in the case of vapor phase diffusion the time evolution of $\bar{r}(t)$ is proportional to:

$$\bar{r}(t) \propto t^{1/2} \quad (1.11)$$

and in the case of substrate surface diffusion:

$$\bar{r}(t) \propto t^{1/4}. \quad (1.12)$$

For sinter resistant exhaust-gas after-treatment catalysts, it is crucial to investigate the kinetics of Ostwald ripening especially for platinum and to some extent rhodium, because they form volatile oxides^{25,26}. The volatile oxides are especially formed under high temperatures and oxidizing conditions as found in exhaust-gas converters. Thus the diffusion of metal oxide molecules over the gas phase is a likely sinter mechanism.

In the case of platinum, PtO₂ is a relatively stable volatile oxide²⁶. To create PtO₂, a metal atom in form of an oxide has to be transferred into the gas phase. The required energy can be approximated from the reaction enthalpy of:



Thus the equilibrium pressure of PtO₂ in the gas phase is given by the equilibrium constant K of eq. (1.13) and the pressure of oxygen p_{O_2} :

$$p_{\text{PtO}_2} = K \times p_{\text{O}_2}. \quad (1.14)$$

The equilibrium pressure p_{eq} can be used similarly to the equilibrium concentration c_r in eq. (1.5). Plessow and Abild-Pedersen²⁷ investigated in detail Ostwald ripening of Pt nanoparticles via volatile PtO₂ based on the model derived by Wynblatt and Gjostein²³. They assume that the number of PtO₂ molecules hitting the particle surface A follows from the ideal gas law:

$$J = A \times \frac{p}{\sqrt{2\pi m k_B T}} \quad (1.15)$$

and that the flux of O₂(g) molecules is not limiting the formation of PtO₂(g). In the model of Wynblatt and Gjostein²³, an uniform background pressure p_b exists which is generally different from the equilibrium pressure of a particle of radius r , $p_{\text{eq}}(r)$. Plessow and Abild-Pedersen²⁷ derive the total flux of PtO₂ molecules of a particle of radius r as:

$$J(r)_{\text{tot}} = \frac{S \times A(r)}{\sqrt{2\pi m k_B T}} (p_b - p_{\text{eq}}(r)). \quad (1.16)$$

Steady-state conditions are assumed, meaning that the total flux between all particles and the gas phase is 0: $\sum_r J(r)_{\text{tot}} = 0$. Thus they define the general background pressure p_b as:

$$p_b = \frac{\sum_r A(r) \times p_{\text{eq}}(r)}{\sum_r A(r)}, \quad (1.17)$$

implying mass conservation of Pt. The described approach is used to simulate the evolution of PSDs with time for different temperatures. It is not only applicable for the simulation of gas phase ripening of platinum, but can also be used for other metals which form volatile oxides.

Particle migration

The simulation of migration and coalescence requires a diffusion constant for the whole nanoparticle on the support. In addition, experiments demonstrated that for example defects²⁸ or differences in particle concentrations^{29,30} influence the sintering behavior. Because of different nanoparticle sizes, diffusion constants are generally size dependent. Also, the shape of the nanoparticles, and the interaction between the support and the nanoparticle facet on which the nanoparticle is supported varies depending on the exposed surface^{31,32}. Thus, studies either employ empirical or assumed diffusion constants or only study the trends in particle migration^{33–35}. To investigate particle migration with first principle methods as density functional theory (DFT) is limited to small particle sizes due to the increasing complexity with increasing particle size.^{36–41}

The first approach was to use the Brownian motion⁴² of the adatoms of clusters to describe the motion of an entire nanoparticle, because a small displacement of one adatom leads to a small shift in the center of mass of the entire particle and thus multiple of this shifts lead to particle diffusion. This was first derived by Sutherland⁴³, Smoluchowski⁴⁴ and Einstein⁴², for which reason particle migration and coalescence is also referred to as Smoluchowski ripening. Following the treatment of diffusion of adatoms by Morgenstern et al.⁴⁵, Khare et al.⁴⁶ and Jak et al.¹⁸ the diffusion constant of a hemispherical particle can be written as:

$$D_c(r) = \frac{3V_m^2 \rho_{\text{adatom}} D_{\text{adatom}}}{\pi r^4} \quad (1.18)$$

with ρ_{adatom} , the adatom density of the particle surface and D_{adatom} the diffusion constant of the adatoms over the cluster surface. With the assumptions that ρ_{adatom} is independent of r and in the case of hemispherical nanoparticles the following power law can be found^{47,48} similar to the ones for Ostwald ripening:

$$\bar{r}(t) \propto t^{1/7}. \quad (1.19)$$

Based on single atom movements on nanoparticles, Li et al.⁴⁹ proposed a kinetic Monte Carlo (kMC) model which aims to understand the sintering behavior of individual platinum nanoparticles of various sizes, temperatures and adhesion energies. They used DFT to derive rate constants to describe the particle migration implemented in a 3D kMC model and a metal coordination based approach to describe the local diffusion of individual atoms. Their observed diffusion process can be described by a lattice-hop model:

$$D = l^2 \frac{k_B T}{h} \exp(-G_a/k_B T), \quad (1.20)$$

in which the diffusion constant D can be expressed through a usually temperature dependent free energy of activation G_a . l is the lattice parameter ($l=2.89 \text{ \AA}$ in the case of platinum), k_B the Boltzmann constant and h Planck's constant. Li et al.⁴⁹ observed that the size dependent activation energy for diffusion $E_a(n)$ is temperature independent. They fit the free energy of activation $G_a(n)$ with the following expressions for particles of size n :

$$G_a(n) = c_1 + c_2 \times \log(n) \quad (1.21)$$

with $c_1 = 0.474 \text{ eV}$ and $c_2 = 0.334 \text{ eV}$ being constants. Li et al.⁴⁹ observed an increase of the particle diffusion constant with increasing temperature and an increase of the free energy of activation for the diffusion with particle size. An increase in the adhesion energy between particle and support lead also to an increased free energy of activation. Similar observations were made by Lai and Evans⁵⁰. Additionally they observed local minima in the size dependent diffusion constant, which they found to correspond to mainly closed-shell nanoparticles depending on the adhesion energy.

1.2.2 Experimental detection

Experimentally it is difficult to study and distinguish Ostwald ripening and particle migration and coalescence. Usually sintering is noticed by a reduction of catalyst activity. Easiest to probe is for particle migration and coalescence and its absence by comparing images, from for example transmission electron microscopy (TEM), during the experiment^{51,51-54}. Examples for the direct observation of particle migration and coalescence are in Pd on TiO₂ observed with scanning tunneling microscopy (STM) by Jak et al.¹⁸ and Pt on Al₂O₃ by Sushumna and Ruckenstein⁵⁵. Although they clearly identify particle migration and coalescence, Ostwald ripening couldn't be excluded entirely, especially for very small clusters, consisting only of a few atoms. Also they state that it is difficult to determine diffusion constants for modeling the studied systems, because the support structure is complex. To reduce the complexity of real catalysts, typically model catalysts are used. Their advantage is the

possibility to study the effect of different initial PSDs, supports and gas phase compositions in a well defined environment. Typically TEM experiments are used to study the PSD of model catalysts.^{17,19,52,56,57} Advances in in-situ TEM give the possibility to follow the evolution of the PSD under reaction conditions. This is also demonstrated in Fig. 1.4a where in-situ TEM images are shown, taken from Simonsen et al.⁵⁸ for a Pt/SiO₂ model catalyst at 650°C in 10 mbar air. Fig. 1.4b shows the corresponding evolution of the PSD. This time resolved measurements give the possibility to study the growth and shrinking of nanoparticles individually and give good opportunities to probe the developed kinetic models. Additionally to TEM, atomic force microscopy (AFM) and STM can be used to analyze the height to diameter ratio of the probe nanoparticles or to measure the PSD.

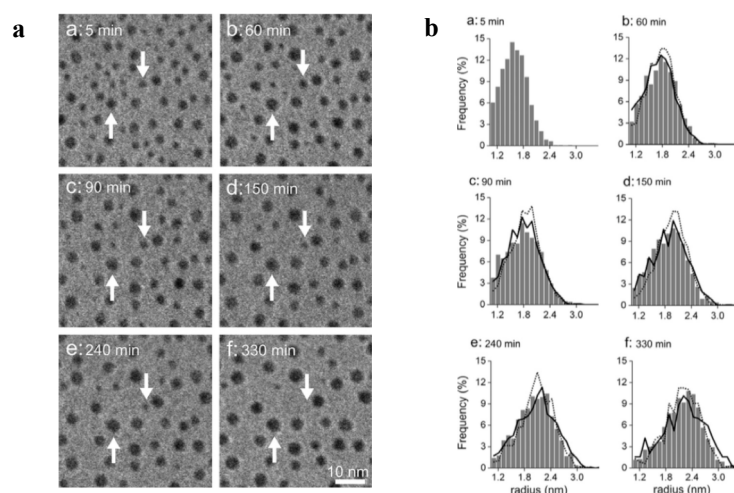


Figure 1.4: Reprinted from ref. 58, Copyright (2011), with permission from Elsevier: (a) (a–f) Time-lapsed TEM images recorded in situ at the same area of the Pt/SiO₂ model catalyst during exposure to 10 mbar air at 650°C. The images are 50 × 50 nm² sections of the full TEM images of size 130 × 130 nm². The denoted times are relative to the time at which the temperature reached 650°C. To guide the eye, arrows indicate examples of a growing and of a decaying particle. (b) (a–f) Time-lapsed particle size distributions obtained from the static TEM images. The static TEM images were recorded in situ of different areas of the Pt/SiO₂ model catalyst during the exposure to 10 mbar air at 650°C. Prior to the static TEM image acquisition, the areas were unexposed to the electron beam. The number of measured particles included in each distribution is (a) 1593, (b) 2059, (c) 1101, (d) 1225, (e) 1095, and (f) 1134. The lines indicate histograms simulated based on the interface-controlled (solid) and diffusion-controlled (dotted) ripening models.

In regard of exhaust-gas after-treatment catalysts, platinum supported on alumina^{51,59–64} or α -quartz^{28,51,58,65–68}, and palladium supported on alumina^{69–73} catalyst are extensively studied. In most cases no particle migration and coalescence could be directly observed, leading to the conclusion that Ostwald ripening might be the dominating sintering mechanism. To validate this conclusion usually kinetic models^{27,74,75} are used to simulate the measured PSD. For Ostwald ripening a PSD with tail towards small particles is expected and for particle migration and coalescence no small particles. Already Lifshitz, Slyozov²² and Wagner¹⁶ proposed that the shape of the PSD implies the dominating sintering mechanism and to use this was long expected. It is motivated by the different time evolution exponents in eqs. (1.9), (1.10), (1.11), (1.12) and (1.19). To verify this method, Datye et al.⁷⁶ performed a variety of experiments with Pd/Al₂O₃(silica) and Pt/Al₂O₃ model catalysts under conditions where either Ostwald ripening or particle migration and coalescence might be expected and measured the PSD using TEM. They concluded that in general the PSD can not be used to distinguish between the different sintering mechanisms. Their observed PSDs for Ostwald ripening do not generally show tails towards small particles which is justified with that very small particles might undergo particle migration and coalescence or are intrinsically unstable¹⁸. In the case of high metal loading and broad PSDs, tails to larger particle sizes are observed which in

the case of Ostwald ripening is not explainable with the theoretical models. Also Jak et al.¹⁸ concluded that it is not possible to distinguish between the sintering mechanisms from measured growth laws.^{74,75}

1.2.3 Concepts to improve catalyst stability

To improve catalyst lifetime, mainly two types of approaches can be chosen to hinder sintering: a physical or a chemical approach. Goodman et al.¹⁴ define the chemical approach to hinder sinter by changing the catalyst chemistry on an atomic scale. This implies modifying the structure of the catalyst and/or its environment. One example would be to change the metal phase by alloying. This was demonstrated for example in PtRh supported on barium-hexa-aluminate catalysts⁷⁷ or Pt/Pd bimetallic materials^{78–80}. To modify the electronic environment, organic support functionalization^{81–83} or engineered metal-support interactions could be used. Oxide supports affect the catalytic activity of metal particles in many ways, by changing their electronic structure^{84–86}, by directly participating in reactions at the metal-oxide interface^{87–94} or by enhancing deactivation through encapsulation in the so-called strong metal support interaction (SMSI) effect^{95–98}. The most basic effect, however, is the energetic stabilization at the metal-oxide interface that determines the particle shape and is crucial in slowing down sintering and thus maintaining the active state of the catalysts^{11,17,99–102}. Here, the support can influence the stability with respect to sintering in two ways. On one hand, the kinetics of Ostwald ripening and particle migration and coalescence depend sensitively on the adsorption and diffusion of metal atoms on the support^{40,49,103–106}. On the other hand, metal-support interaction determines the stability of metal nanoparticles. This in turn modifies the size-dependence of the chemical potential of the metal and therefore the driving force for sintering.²⁰

The physical approach contains geometric modifications of the supporting materials or the introduction of physical barriers to hinder sintering. Thus support materials with a high surface area increase the inter metal particle distance¹⁰⁷ and thus increase the time scale for particle migration and coalescence which was for example shown for Pt/silica materials.¹⁰⁸ Another possibility would be to use narrow PSDs to reduce Ostwald ripening.²⁷ Also, partially embedded nanoparticles or overlayers to protect the active phase are intensively investigated.^{109–112}

1.3 Scope of this thesis

The aim of this thesis is to gain a deeper understanding of the thermodynamic stability of metal nanoparticles and the stabilization effects of oxide supports in heterogeneous catalysts. Therefore DFT based kinetic modeling is used to focus on the different contributions of particle migration and coalescence and Ostwald ripening.

Chapter 3 presents a detailed DFT study on the thermodynamic stability of metal nanoparticles. Anchoring nanoparticles on a support leads to an increase in stability against sintering through particle migration. Ultimately, the driving force for sintering is the thermodynamic stability of nanoparticles compared to the bulk structure. A simple model which is based on DFT calculations is derived to predict the thermodynamic stability of metal nanoparticles in general and is verified by comparison to DFT calculations of nanoparticles.

Chapter 4 investigates the adhesion energy between various transition metals and oxide supports commonly used as catalytic systems using DFT. The adhesion energy characterizes the strength of interaction between a metal and support and is therefore suitable to describe the possible effect of stabilization of the metal oxide on the metal nanoparticles. The focus is on developing scaling relations to predict stabilities of unknown materials.

Chapter 5 presents a combined study of vapor phase Ostwald ripening and particle migration and coalescence using an adaptive kMC scheme to combine the mean-field model for Ostwald ripening with the kMC model of particle migration and coalescence. Using this combined sintering study for the example of platinum on quartz gives detailed insights into the experimental conditions under which each sintering mechanism is dominating.

Section 1.2.3 is partially reproduced from ref. 31.

Chapter 6 is dedicated to the development of a kMC model to describe the diffusion of atoms and molecules through the gas phase. In a second step, this model is used to benchmark the mean-field model for Ostwald ripening and to investigate its limitations.

2 Methods

2.1 Introduction

To understand multi-atomic systems, the electronic ground-state energy and structure can be investigated using density functional theory (DFT). With DFT it is possible to calculate the atomic configurations resulting from geometry optimizations, representing minima at 0 K. Using the harmonic approximation to describe the vibration of atoms gives the possibility to calculate the Gibbs free energy. Thus equilibrium constants of reactions can be obtained. To determine the barrier of a reaction, the transition state can be calculated using the nudged elastic band¹¹³ or dimer method^{114,115}. The obtained barriers for a reaction can be used to calculate rate constants. These rate constants give the possibility to bridge from static DFT calculations to kinetic simulations. In this chapter, the basic theory of the in this thesis employed methods DFT and kinetic Monte Carlo (kMC) is introduced.

2.2 Quantum mechanical treatment of nanoparticles and surfaces

The equation of motion used in quantum chemistry is the time-dependent Schrödinger equation:

$$\hat{H}(\mathbf{r},t)\Psi(\mathbf{r},t) = i\hbar\frac{\partial}{\partial t}\Psi(\mathbf{r},t) \quad (2.1)$$

with \hat{H} the Hamilton operator which defines the particles the system consists of and how these particles interact with each other and external potentials and their kinetic energy. Ψ is the wave function describing the state of the system. If Ψ is known, all measurable properties of a system can be calculated. $\hbar = h/2\pi$ is the reduced Planck constant, t the time and \mathbf{r} the position vector containing all positions of N particles in the system. Because the main interest in quantum chemistry are stationary states instead of the explicit time development of a system, \hat{H} is assumed to be independent of t . Thus the Schrödinger equation can be separated in a time dependent and time independent part:

$$\Psi(\mathbf{r},t) = \Psi(\mathbf{r}) \cdot \exp\left(\frac{-iEt}{\hbar}\right) \quad (2.2)$$

with E , the energy of the system.

The Hamilton operator contains the interactions of electrons (index: e) and nuclei (index: N) of a system in form of contributions from the kinetic energy (\hat{T}) and the potential interaction energy (\hat{V}):

$$\hat{H} = \hat{T}_e + \hat{T}_N + \hat{V}_{ee} + \hat{V}_{eN} + \hat{V}_{NN} \quad (2.3)$$

Born-Oppenheimer-approximation

In the Born-Oppenheimer-approximation¹¹⁶ it is assumed that the electrons instantaneously react to changes of the atomic positions. That is plausible, because nuclei are three order of magnitudes heavier than electrons, thus in comparison to electrons very slow. Thus it is assumed that the wave function $\Psi(\mathbf{R}, \mathbf{r})$, depending on the nuclear coordinates \mathbf{R} and electron coordinates \mathbf{r} , can be written as product of the nuclear and electron wave function:

$$\Psi(\mathbf{R}, \mathbf{r}) = \Psi^{\text{nuc}}(\mathbf{R}) \cdot \Psi^{\text{electron}}(\mathbf{r}, \{\mathbf{R}\}), \quad (2.4)$$

where the curly brackets indicate that Ψ^{electron} depends parametrically on \mathbf{R} . With $\hat{T}_N = 0$ and $\hat{V}_{NN} = \text{constant}$ the electronic Schrödinger equation can be written as:

$$[\hat{T}_e + \hat{V}_{ee} + \hat{V}_{eN}] \Psi^{\text{electron}}(\mathbf{r}, \{\mathbf{R}\}) = E_e \Psi^{\text{electron}}(\mathbf{r}, \{\mathbf{R}\}) \quad (2.5)$$

and

$$E_{\text{tot}} = E_e + \underbrace{\langle \hat{V}_{NN} \rangle}_{\text{constant}}. \quad (2.6)$$

E_{tot} is the total energy.

Under the assumption that \hat{T}_N has no impact on Ψ^{electron} , a Schrödinger equation for the nuclei can be formulated which is solved to calculate vibration spectra:

$$[\hat{T}_N + \hat{V}_{NN} + E_e(\mathbf{R})] \Psi_{\text{nuc}}(\mathbf{R}) = E \Psi_{\text{nuc}}(\mathbf{R}). \quad (2.7)$$

2.3 Density functional theory

DFT is not focusing on finding the wave function Ψ , but instead the electron density $\rho(\mathbf{r})$. The basis of DFT is the first theorem of Hohenberg and Kohn¹¹⁷ which states, that the external potential is a unique functional^a of the electron density, $E[\rho(\mathbf{r})]$. The external potential is here defined as the potential induced by the atomic nuclei. Thus knowing the nuclei positions implies knowing all system properties. The number of electrons N_e can be calculated as the integral of the electron density:

$$N_e = \int \rho(\mathbf{r}) d\mathbf{r}. \quad (2.8)$$

The second theorem of Hohenberg and Kohn¹¹⁷ says, that for any ansatz of the density $\tilde{\rho}(\mathbf{r})$, the functional $E[\tilde{\rho}(\mathbf{r})]$ is larger or equal to the ground state energy:

$$E[\tilde{\rho}(\mathbf{r})] \geq E[\rho_0(\mathbf{r})]. \quad (2.9)$$

The central problem of DFT is that the exact functional $E[\rho(\mathbf{r})]$ is unknown.

Kohn and Sham developed the so called Kohn-Sham (KS) theory¹¹⁸. Key is the introduction of a reference system containing only non-interacting fermions (particles with half-integer spin, e.g. electrons), but with the same ground state density as the interacting system. Non-interacting systems have the advantage that their ground state wave function can be constructed exactly as Slater determinant. The Slater determinant is a special way of constructing the wave function which full fills the Pauli principle. The Pauli principle defines that two or more identical fermions can not occupy the same quantum state simultaneously. The kinetic energy $T_S[\rho]$ of the non-interacting system can be calculated as the expectation value of the Slater determinant. It follows that the energy functional can be split into two parts, one known, the other unknown. The known part consists of the kinetic energy $T_S[\rho]$ of non-interacting electrons, the classical part of the Coulomb term $J[\rho]$ and the attraction of the nuclei and electrons, $E_{Ne}[\rho]$. The unknown part, the kinetic energy of interacting fermions is assumed to be small compared to $T_S[\rho]$. It is summarized in the so called exchange-correlation term $E_{XC}[\rho]$ together with the exchange and correlation contributions to the electron-electron interaction. The total DFT energy functional can be written as:

$$E_{\text{DFT}}[\rho] = T_S[\rho] + E_{Ne}[\rho] + J[\rho] + E_{XC}[\rho] \quad (2.10)$$

^a A functional is a function of a function, e.g. $g[f(x)]$.

To use DFT in practice, $E_{XC}[\rho]$ is approximated.

Approximate exchange-correlation functionals

Usually, exchange-correlation functionals are constructed as sum of individual exchange and correlation functionals (E_X and E_C):

$$E_{XC} = E_X + E_C. \quad (2.11)$$

The oldest and simplest approximation is the so-called local density approximation (LDA)^{119–121}. It is derived from the homogeneous electron gas which has a constant density. A homogeneous electron gas is a system with an infinite number of electrons in an infinite extended uniform, positively charged background, which leads to a overall neutral charge. In this case the exchange-correlation functional only depends on the local density:

$$E_{XC}^{LDA}[\rho] = \int f[\rho(\mathbf{r})]d^3\mathbf{r}. \quad (2.12)$$

It was calculated by Ceperley and Alder¹²² and analytically analyzed by Vosko, Wilk and Nusair¹²³.

The generalized gradient approximation (GGA) was introduced to improve on LDA. Additionally, to the density dependence of E_{XC} it also includes the first derivative with respect to space of the density:

$$E_{XC}^{GGA}[\rho] = \int f[\rho(\mathbf{r}), \nabla\rho(\mathbf{r})]d^3\mathbf{r}. \quad (2.13)$$

Typical functionals are BLYP^{124,125} and PBE^{126–128}. In addition, also the second derivative with respect to space can be included. This type of functionals is called meta-GGA (e.g. TPSS¹²⁹). Another possibility is to include Hartree-Fock (HF) exchange to reduce the self-interaction error. The self-interaction error is caused by the interaction of an electron with itself, because the approximated exchange energy does not completely cancel the self-interaction contribution in the Coulomb energy. So called hybrid functionals are for example B3LYP (20% HF exchange)^{130–132} or PBE0 (25% HF exchange)¹³³. To include dispersion corrections an additional term is added to the energy. This is typically marked by “-D” or “-vdW” in the functional name, e.g. the Bayesian error estimation functional (BEEF-vdW)¹³⁴.

Van-der-Waals interaction

Van-der-Waals (vdW) interactions (also called London dispersion interactions) describe interactions between uncharged, closed shell systems which are not directly bonded^{135,136}. Due to the motion of electrons, local dipoles are created in an atom which can induce another dipole in the neighboring atoms. If two atoms are very close, vdW interactions are repulsive because of the repelling forces between the negatively charged electrons. For intermediate distances, the induced dipole-dipole interactions are attractive. Theoretically this attraction varies as the inverse sixth power of the distance between two atoms. It becomes zero for very large distances. The general functional form is:¹³⁷

$$E_{vdW}(r_{AB}) = E_{repulsion}(r_{AB}) - \frac{C^{AB}}{(r_{AB})^6} \quad (2.14)$$

with E_{vdW} the vdW energy, r_{AB} the distance between two atoms A and B, $E_{repulsion}$ the repulsive energy and C^{AB} a constant.

There exist different possibilities to include dispersion corrections into DFT calculations. One is to use perturbation theory to calculate the intra-molecule electron correlation based on the DFT calculation, so called DFT symmetry-adapted perturbation theory (DFT-SAPT)¹³⁸. Another possibility is to use vdW functionals, which directly include dispersion corrections, like the ALL-functional¹³⁹ or VV09-functional¹⁴⁰.

In this thesis, semi-empirical dispersion-corrected functionals are used, where a modification is added to e.g. GGA functionals. In principle three levels of dispersion correction from the DFT-D (D1¹⁴¹, D2¹⁴² and D3¹⁴³) kind exist, of which DFT-D3 is used. The correction for the dispersion E_{disp} is added to the energy of the pure functional, $E_{\text{KS-DFT}}$:¹⁴³

$$E_{\text{DFT-D3}} = E_{\text{KS-DFT}} - E_{\text{disp}}, \quad (2.15)$$

with $E_{\text{disp}} = E^{(2)} + E^{(3)}$. The more important two body term $E^{(2)}$ is given by:¹⁴³

$$E^{(2)} = \sum_{AB} \sum_{n=6,8} s_n \frac{C_n^{AB}}{r_{AB}^n} f_{d,n}(r_{AB}). \quad (2.16)$$

The first sum is over all atom pairs AB , C_n^{AB} the dispersion coefficients of order $n = 6, 8$ and s_n scaling factors, which are adjusted for $n > 6$ and equal unity for $n = 6$. In principle also higher orders could be included. The coefficients C_n^{AB} for the D3-correction were obtained by Grimme et al.¹⁴³ using time-dependent KS-DFT^b. Damping functions $f_{d,n}$ are used to determine the range of the dispersion function and to avoid double-counting effects for intermediate distances or singularities for small distances r_{AB} . Commonly either, a so called zero-damping function proposed by Chai and Head-Gordon¹⁴⁵ or the Becke and Johnson (BJ)^{146,147} damping function is used. In Figure 2.1 the dispersion correction for two argon atoms depending on the chosen damping function is shown. It can be seen that zero-damping and BJ-damping mainly diverge for $r_{AB} \rightarrow 0$. In the case of zero-damping the dispersion correction approaches zero for $r_{AB} \rightarrow 0$, but the BJ-damping leads to a constant contribution to the total energy. Grimme et al.¹⁴⁸ concluded that the choice of the damping function does not influence the results significantly.

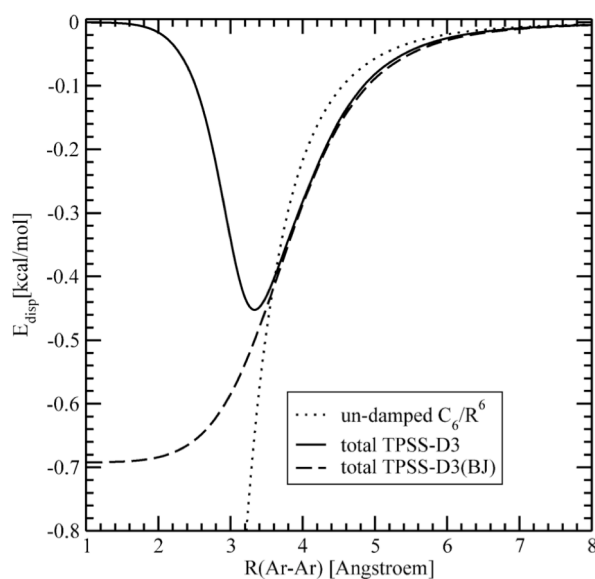


Figure 2.1: Reprinted from ref. 148, Copyright (2011), with permission from John Wiley and Sons: Dispersion correction for two argon atoms (including sixth- and eight-order terms, dispersion coefficients from ref. 143) with the zero- and BJ-damping methods in comparison the un-damped $-C_6 \cdot R^{-6}$ term.

^b Time-dependent KS-DFT¹⁴⁴ is used to calculate the time-dependent response of a system to e.g. an electronic or magnetic field.

Basis set

Atomic orbitals are approximated numerically using localized basis sets. In the linear-combination-of-atomic-orbitals (LCAO) approach, an orbital ψ_i is described by a linear combination of one-electron basis functions ϕ_μ , of Slater¹⁴⁹ or Gaussian¹⁵⁰ type:

$$\psi_i(\mathbf{r}_j) = \sum_{\mu} C_{i\mu} \phi_{\mu}(\mathbf{r}_j). \quad (2.17)$$

To model extended systems like surfaces, usually a unit cell with periodic boundary conditions is used. To describe the periodicity correctly it seems obvious to use functions of infinite range: plane waves. According to Bloch's theorem¹⁵¹, in a periodic potential, each electronic wave function can be written as a product of the lattice periodic part: $u(\mathbf{k}, \mathbf{r} + \mathbf{R}) = u(\mathbf{k}, \mathbf{r})$ and a plane wave: $\exp(i\mathbf{k}\mathbf{r})$:

$$\psi(\mathbf{k}, \mathbf{r}) = \exp(i\mathbf{k}\mathbf{r}) \cdot u(\mathbf{k}, \mathbf{r}). \quad (2.18)$$

Expanding the lattice periodic part in plane waves with wave vectors \mathbf{G} in reciprocal space gives:

$$\psi_j(\mathbf{k}, \mathbf{r}) = \sum_{\mathbf{G}} c_{j,\mathbf{k},\mathbf{G}} \cdot \exp(i(\mathbf{k} + \mathbf{G})\mathbf{r}). \quad (2.19)$$

with $c_{j,\mathbf{k},\mathbf{G}}$ expanding coefficients. In practice only a finite number of plane waves can be used. That is sufficient, because there exist only discrete \mathbf{G} because of the lattice periodicity and the coefficients of small kinetic energy are usually most important.¹³⁷ The cut-off energy of the plane waves corresponds to the highest kinetic energy of all basis functions and determines the number of basis functions:

$$E_{\text{cut-off}} = \frac{\hbar^2}{2m} |\mathbf{G}_{\text{max}}|^2 \quad (2.20)$$

Thus the convergence of the calculated total energy can be systematically investigated by increasing $E_{\text{cut-off}}$.

Pseudopotential method

The strength of plane waves is the description of delocalized electrons, but in the core region of an atom the wave function is rapidly oscillating. To describe these rapid oscillations, a very high cut-off energy would be necessary, implying that a large number of plane waves would have to be used. Because these core electrons usually do not contribute to chemical bonds, especially for heavy elements in the periodic table, they are described using pseudo potentials and only the valence electrons are modeled explicitly using plane waves.

In the so called projector augmented wave (PAW) method^{152,153}, formally all electrons are considered. It is illustrated in Figure 2.2. Rapid oscillation of a function is shown within the atomic sphere and slow variation in the interstitial region between two atoms.

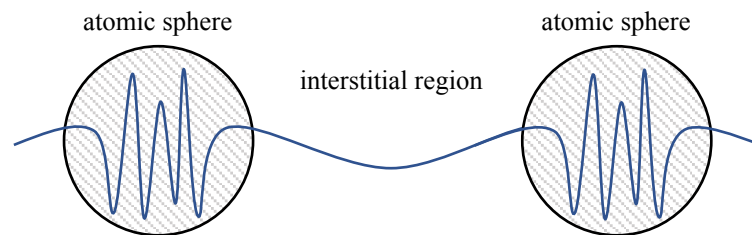


Figure 2.2: Schematic visualization of the separation in atomic sphere and interstitial region in the PAW.

Formally, the PAW wave function is written as a valence term expanded in a plane wave basis plus a contribution from the region with the core radius of each nucleus. The contribution from the core region is expanded as the difference between two sets of densities, one arising from the atomic orbitals, the other a set of nodeless pseudo-atomic orbitals. These are necessary to adjust the wave function of the core to different chemical environments.¹³⁷ The PAW potentials used¹⁵³, are constructed for isolated atoms, but in principle they could be adjusted during e.g. DFT calculations.

2.4 Kinetic Monte Carlo

As mentioned in the introduction, kMC is employed to investigate the dynamics of a system using rate constants, obtained for example with DFT. The Markov approximation^{154,155} is used, where a system in a stable configuration i jumps into configuration j , independent of the configuration the system was in before i . The probability density function $P_i(t)$ to find the system in state i is evaluated over the time t . This time evolution can be described using a master equation of the form¹⁵⁶:

$$\frac{dP_i(t)}{dt} = - \sum_{j \neq i} k_{ij} P_i(t) + \sum_{i \neq j} k_{ji} P_j(t), \quad (2.21)$$

with the sums over all states j of the system. The first term of the equation describes the probability to jump from state i into state j with the rate k_{ij} , thus decreasing the probability to find the system in state i at time t . The second term describes the probability to jump from j to i with rate k_{ji} which increases $P_i(t)$. It might be still possible to find the analytical solution to the master equation of a two configurational system, but the complexity increases with the number of configurations. Thus a numerical solution is found instead by calculating trajectories which propagate the system forward in time. In the end, the average over the calculated trajectories has to yield the probability density function $P_i(t)$ for all states i fulfilling eq. (2.21)¹⁵⁶. The trajectories consist of a sequence of jumps between the possible system configurations. The master equation determines the random selection of the next hopping step and the time, after which this step occurs. The time after which the next step occurs is called escape time t_{escape} and is mainly determined by the rate constants of the system. The system time is advanced by $t \rightarrow t + t_{\text{escape}}$. For a hop from state i to j with rate k_{ij} , t_{escape} would be calculated according to:

$$\Delta t_{\text{escape}} = - \frac{\ln(\rho)}{k_{ij}} \quad (2.22)$$

with ρ being a random number between 0 and 1.

First reaction method

In principle only one process (or jump) per time step is accessible. Thus it would be intuitive to calculate for every possible process t_{escape} and chose the one with smallest t_{escape} . This method is called first reaction method and is also known as discrete event simulation¹⁵⁷. The disadvantage of this method is that at every time step, t_{escape} has to be recalculated and the list of processes searched for the minimum, which leads to a linear scaling of the algorithm with the number of processes.¹⁵⁸

Bortz-Kalos-Lebowitz method

A more efficient kMC algorithm is the conventionally used Bortz–Kalos–Lebowitz (BKL) algorithm. Also for this algorithm all possible processes N of the system are first identified and the rate constants k_i calculated for each process. The sum over all rate constants gives the total rate constant k_{tot} :

$$k_{\text{tot}} = \sum_{i=1}^N k_i. \quad (2.23)$$

But instead of calculating all t_{escape} , the executed process q is chosen with a random number $\rho_1 \in (0, 1]$ according to:

$$\sum_{i=1}^q k_i \geq \rho_1 k_{\text{tot}} \geq \sum_{i=1}^{q-1} k_i. \quad (2.24)$$

The system time is advanced by:

$$\Delta t = -\frac{\ln \rho_2}{k_{\text{tot}}}, \quad (2.25)$$

with $\rho_2 \in (0, 1]$ being a second random number. This reduces the number of random numbers from N (one per process in the first reaction method) to two per time step. The BKL algorithm is visualized schematically in Figure 2.3.

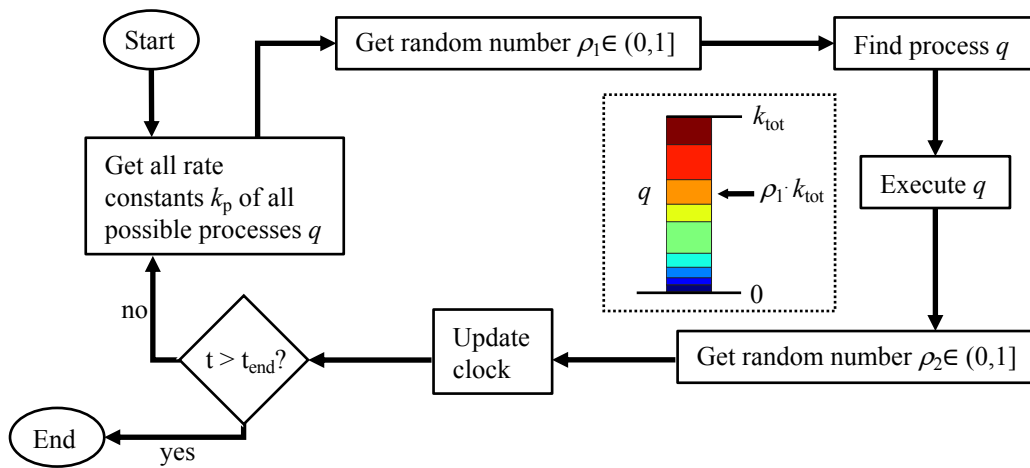


Figure 2.3: Schematic visualization of the Bortz-Kalos-Lebowitz method, adapted from K. Reuter¹⁵⁶. The inset visualizes eq. (2.24) with different possible processes in different colors.

It can be imagined that from e.g. two processes the one dominantly chosen with eq. (2.24) is the one with the higher rate constant. Also, although in eq. (2.25) the advancement of the system time is independent of t_{escape} , it is still dominated by the process with the highest rate constant, because the time is indirectly proportional to the rate constants. In consequence the maximum time step length is limited by the fastest process.

3 Thermodynamic stability of metal nanoparticles

3.1 Introduction

Supported Pt nanoparticles are used in a range of processes, with emission control being one of the most important applications^{159,160}, in which the size and shape of the particles not only influences the activity but also the stability of the catalyst^{57,161–163}. Therefore, the size and shape dependence of the thermodynamic stability of bare Pt nanoparticles is investigated in detail first and results of the density functional theory (DFT) calculations are compared to the widely used Wulff construction model (WC)¹⁵. The stability of nanoparticles that are typically only a few nanometers in diameter is dictated by the kinetics of the sintering processes,^{14,68,108} and the stability can be greatly improved through a stabilization of the nanoparticles on the support^{3,96}. This can be achieved through e.g. anchoring of the nanoparticles on defects of oxidic supports or changing the chemical environment of the supports, for example with functionalized organic molecules⁶⁸. Ultimately, however, the main driving force for sintering is given by the thermodynamic stability of the nanoparticles, which increases with particle size since the ratio of thermodynamically less stable surface atoms to bulk atoms decreases. In the literature, several models to estimate the size-dependency of the thermodynamic stability of nanoparticles are proposed^{164–167}, but a simple model which is easily transferable to different metals is still missing. Therefore a simple model is introduced that enables to derive the stability of metal particles. The model is verified through DFT calculations of mono metallic nanoparticles of late transition metals as well as Al and Mg ranging from 0.5 nm to 3.3 nm in diameter.

3.2 Computational details

For all DFT calculations the PBE¹²⁶ functional and the D3-dispersion correction¹⁴³ implemented in the VASP^{168–171} program package in version 5.4.1 using the projector-augmented wave (PAW) method with standard PAW-potentials¹⁵³ were used. The PBE-D3 functional was chosen because it reproduces the experimental Pt(111) surface energy (1.03 eV¹⁷²), which is not the case for other functionals¹³⁴. To demonstrate this, Figure 3.1 shows an adoption of Fig. 8 of the paper of Wellendorf et al.¹³⁴.

For all calculations a Γ -centered k-point sampling and Gaussian smearing with a width of 0.1 eV is used. Structures were optimized until atomic forces were below 0.01 eV/Å.

For the bulk lattice parameter and the fit of the dependence of the bulk energy on the lattice parameter, a cut-off of 800 eV was used for the plane wave basis set and a (16,16,16) Monkhorst-Pack grid. The obtained bulk lattice parameter a_0^{bulk} and bulk chemical potential $\mu_{\text{bulk}}^{\text{metal}}$ relative to the gas phase atom are presented in Table 3.1. The values for the lattice parameter dependent chemical potential are in Table 9.2. In Table 3.2 the parameters of the quadratic equations are shown which are used for the stability model.

The gas phase atoms are obtained using an energy cut-off of 800 eV. The atoms are placed in a super cell, where the periodic image is separated by 16 Å. Spin-polarization is used and the number of unpaired electrons given in Table 3.1.

This chapter is based on the following publication: Dietze, E. M.; Plessow, P. N.; Studt, F., Modeling the Size-Dependency of the Stability of Metal Nanoparticles. *J. Phys. Chem. C* 2019, 123, 41, 25464-25469.

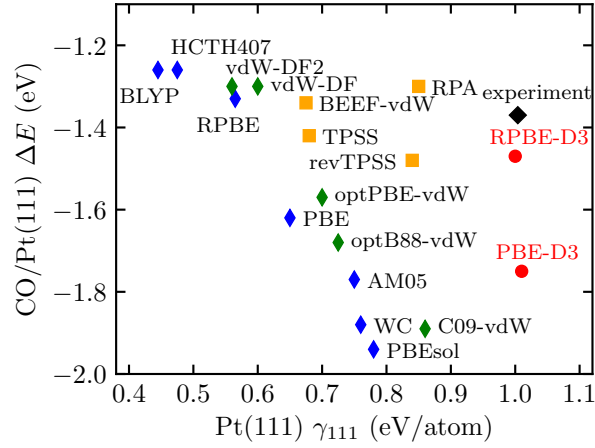


Figure 3.1: Reproduction of Fig. 8 of Wellendorf et al.¹³⁴ PBE-D3 and RPBE-D3 calculations from this work are shown as red symbols. The MGGA and RPA data is taken from Schimka et al.¹⁷³ and the other data points from Wellendorf et al.¹³⁴ The experimental values are taken from liquid-metal data¹⁷² and chemisorption energies of CO/Pt(111) from Abild-Pedersen and Andersson¹⁷⁴ and the references therein.

Table 3.1: Bulk chemical potential $\mu_{\text{bulk}}^{\text{metal}}$ [eV/atom] relative to the gas phase atom, fcc(111) surface energy γ_{111} [meV/Å²] and the corresponding surface area A_{111} [Å²] for all investigated metals. Similar data is shown for the fcc(100) surface: γ_{100} and A_{100} , as well as the lattice constant (a_0^{bulk} [Å]). $E_{\text{bulk}}^{\text{tot}}$ in eV is the total bulk energy, $E_{\text{atom}}^{\text{tot}}$ in eV is the total energy of the gas phase atom and N_{ue} gives the number of unpaired electrons. For Pt, values for PBE-D3 and RPBE-D3 are given. All other values are for PBE-D3.

Metal	$\mu_{\text{bulk}}^{\text{metal}}$	γ_{111}	A_{111}	γ_{100}	A_{100}	a_0^{bulk}	$E_{\text{bulk}}^{\text{tot}}$	$E_{\text{atom}}^{\text{tot}}$	N_{ue}
Ag	-3.01	82.04	7.18	88.29	8.30	4.07	-3.21	-0.199	1
Au	-3.70	92.15	7.28	98.29	8.40	4.10	-3.88	-0.185	1
Co	-5.47	174.45	5.24	201.76	6.05	3.48	-7.36	-1.895	3
Cu	-3.99	137.94	5.52	148.87	6.37	3.57	-4.24	-0.243	1
Ir	-8.02	206.69	6.38	246.75	7.37	3.84	-9.55	-1.524	3
Ni	-5.19	144.32	5.23	162.34	6.04	3.47	-5.87	-0.677	2
Os	-8.76	227.14	6.35	282.80	7.33	3.83	-11.69	-2.930	4
Pd	-4.32	135.92	6.54	135.92	7.55	3.89	-5.80	-1.476	0
Pt (PBE-D3)	-6.26	151.65	6.65	174.29	7.49	3.92	-6.86	-0.608	2
Pt (RPBE-D3)	-5.82	148.17	6.72	170.62	7.76	3.94	-6.48	-0.663	2
Rh	-6.29	182.29	6.21	206.09	7.17	3.79	-7.85	-1.561	3
Ru	-7.22	199.66	6.15	239.09	7.11	3.77	-9.69	-2.473	4
Al	-3.60	68.64	6.95	74.87	8.03	4.01	-3.92	-0.315	1
Mg	-1.69	43.14	8.62	56.21	9.95	4.46	-1.70	-0.001	0

Table 3.2: Parameters of the quadratic equations for $\gamma_{111}(a_0)$ and $\mu^{\text{bulk}}(a_0)$, fitted using the values in Table 9.1 and 9.2.

Metal	a_{111} [eV/Å ²]	b_{111} [eV/Å]	c_{111} [eV]	a_{bulk} [eV/Å ²]	b_{bulk} [eV/Å]	c_{bulk} [eV]
Ag	-1.72	14.03	-28.05	4.13	-33.54	65.17
Au	-2.22	18.58	-38.25	6.21	-50.81	100.22
Co	-2.27	16.26	-28.16	7.19	-50.00	81.41
Cu	-1.46	10.57	-18.41	5.24	-37.31	62.44
Ir	0.74	-4.24	6.56	12.66	-97.11	178.14
Ni	-1.80	12.80	-21.89	6.37	-44.22	71.58
Os	-4.13	33.17	-64.92	13.62	-104.22	190.63
Pd	-2.16	17.07	-32.88	12.12	-66.63	87.24
Pt	-4.16	33.36	-65.88	10.48	-81.95	153.89
Rh	-2.09	16.38	-30.97	17.01	-91.10	115.67
Ru	-4.03	31.50	-60.17	10.80	-81.30	145.83
Al	-1.05	8.48	-16.65	2.81	-22.49	41.42
Mg	-0.12	1.21	-2.55	1.28	-11.45	23.81

For the calculation of the CO adsorption energy, an energy cut-off of 400 eV and a (3,3,1) Monkhorst-Pack grid was used. The periodic images of the surfaces are separated in z -direction by 30 Å. The CO is positioned on top of a Pt atom of a 6 layer 4×4 slab, of which the three bottom layers are frozen. The total energies and adsorption energies are given in Table 3.3 and the adsorption energy E_{ads} is calculated according to:

$$E_{\text{ads}} = E_{\text{CO on top Pt}} - E_{\text{CO}} - E_{\text{Pt slab}}, \quad (3.1)$$

with $E_{\text{CO on top Pt}}$ the energy of the adsorbed CO, E_{CO} the energy of the CO molecule and $E_{\text{Pt slab}}$ the energy of the bare Pt slab.

Table 3.3: Total energies in eV used to calculate the adsorption energy of CO on top Pt (last column) according to eq. (3.1).

Functional	$E_{\text{CO on top Pt}}$	E_{CO}	$E_{\text{Pt slab}}$	E_{ads}
RPBE-D3	-523.52	-14.45	-507.60	-1.47
PBE-D3	-583.01	-14.80	-566.46	-1.75

The fcc(111) and fcc(100) surface energies are calculated from a series of slab calculation with a thickness between 8 and 13 layers. A cut-off energy of 400 eV and a (12,12,1) Monkhorst-Pack grid are employed. The periodic images of the surfaces are separated in z -direction by 16 Å. To fit the dependence of the fcc(111) surface energy on the lattice parameter, various slab calculations were carried out with fixed atom positions but varying lattice parameter (see Table 3.1 for the fcc(111) and fcc(100) surface energy and Table 9.1 for the lattice parameter dependent fcc(111) surface energy). In Table 3.2 the parameters of the quadratic equations are shown which are used for the stability model.

For the nanoparticles, a cut-off energy of 300 eV and a (1,1,1) Monkhorst-Pack grid is used. A vacuum of 14 Å is used in all three dimensions. The calculations were carried out non-spin-polarized, except for Co and Ni. In Table 3.4, the total energy of spin-polarized and non-spin-polarized cuboctahedral clusters of Pt are compared. It

can be seen that spin-polarization has only minor effects, and for cluster with 55 and more atoms no magnetization is observed. For that reason, spin-polarization is not included for metals which are not magnetic in the bulk.

Table 3.4: Comparison of the total energies in eV for spin-polarized and non-spin-polarized calculations for different cuboctahedral Pt cluster. The third column gives the magnetic moment per atom and the last column the difference in the total energy in eV.

N_{atom}	E_{tot} (spin-polarized)	Magnetic moment μ_{B}	E_{tot} (non-spin-polarized)	ΔE_{tot}
13	-57.37	0.42	-56.11	-1.26
55	-295.96	0.00	-295.94	-0.01
147	-854.16	0.00	-854.15	-0.01
309	-1868.90	0.00	-1868.81	-0.09

For the case of Ni and Co in Table 3.5 are compared the magnetic moments of the crystal-phase in fcc structure and of two nanoparticles with the literature. For the Co crystal the calculated magnetic moment ($1.59 \mu_{\text{B}}$) does not agree with Singh and Kroll¹⁷⁵, ($0.16 \mu_{\text{B}}$) but is in agreement with values of H. Ebert et al.¹⁷⁶ ($1.57 \mu_{\text{B}}$) and Marcus and Moruzzi¹⁷⁷ ($1.56 \mu_{\text{B}}$) and also compares well with the magnetic moment per atom obtained for the nanoparticles (Co₅₅: $1.83 \mu_{\text{B}}$, Co₁₄₇: $1.78 \mu_{\text{B}}$). This magnetic moments agree with those calculated by Singh and Kroll¹⁷⁵ (Co₅₅: $1.84 \mu_{\text{B}}$, Co₁₄₇: $1.73 \mu_{\text{B}}$) for the nanoparticles. In the case of Ni, the magnetic moments agree with the results of Singh and Kroll¹⁷⁵ for the crystal and the nanoparticles (crystal: $0.65 \mu_{\text{B}}$, Ni₅₅: $0.73 \mu_{\text{B}}$, Ni₁₄₇: $0.68 \mu_{\text{B}}$).

Table 3.5: Comparison of the magnetic moments calculated in this work for Co and Ni in the fcc structure and the results of Singh and Kroll¹⁷⁵, H. Ebert et al.¹⁷⁶ and Marcus and Moruzzi¹⁷⁷. In the case of the clusters, the magnetic moments are given per atom.

System	Magnetic moment μ_{B}			
	Singh and Kroll ¹⁷⁵	H. Ebert et al. ¹⁷⁶	Marcus and Moruzzi ¹⁷⁷	this work
Co fcc	0.16	1.57	1.56	1.59
Co ₅₅	1.84			1.83
Co ₁₄₇	1.73			1.78
Ni fcc	0.65	0.57		0.59
Ni ₅₅	0.73			0.71
Ni ₁₄₇	0.68			0.68

Accuracy of DFT parameters

To show the convergence of the calculated metal properties, the convergence of the lattice constant of Pt for different cut-off energies $E_{\text{cut-off}}$ and densities of the k-point sampling is shown in Fig. 3.2a and 3.2b respectively. Plotted is the relative variation of the lattice constant in % with respect to the used parameters. It can be seen that for a (16,16,16) k-point sampling the lattice constant is converged for $E_{\text{cut-off}} \geq 600$ eV. Using $E_{\text{cut-off}} = 800$ eV for different k-point samplings shows the convergence in the k-point density for (16,16,16) and higher. In Fig. 3.2c the convergence of the total energy for two different cuboctahedral nanoparticles, Pt₅₅ and Pt₁₄₇, with the employed vacuum size in all dimensions is shown. The difference in total energy of the calculations to the total energy calculated with a vacuum of 14 \AA converges for sizes of 12 \AA .

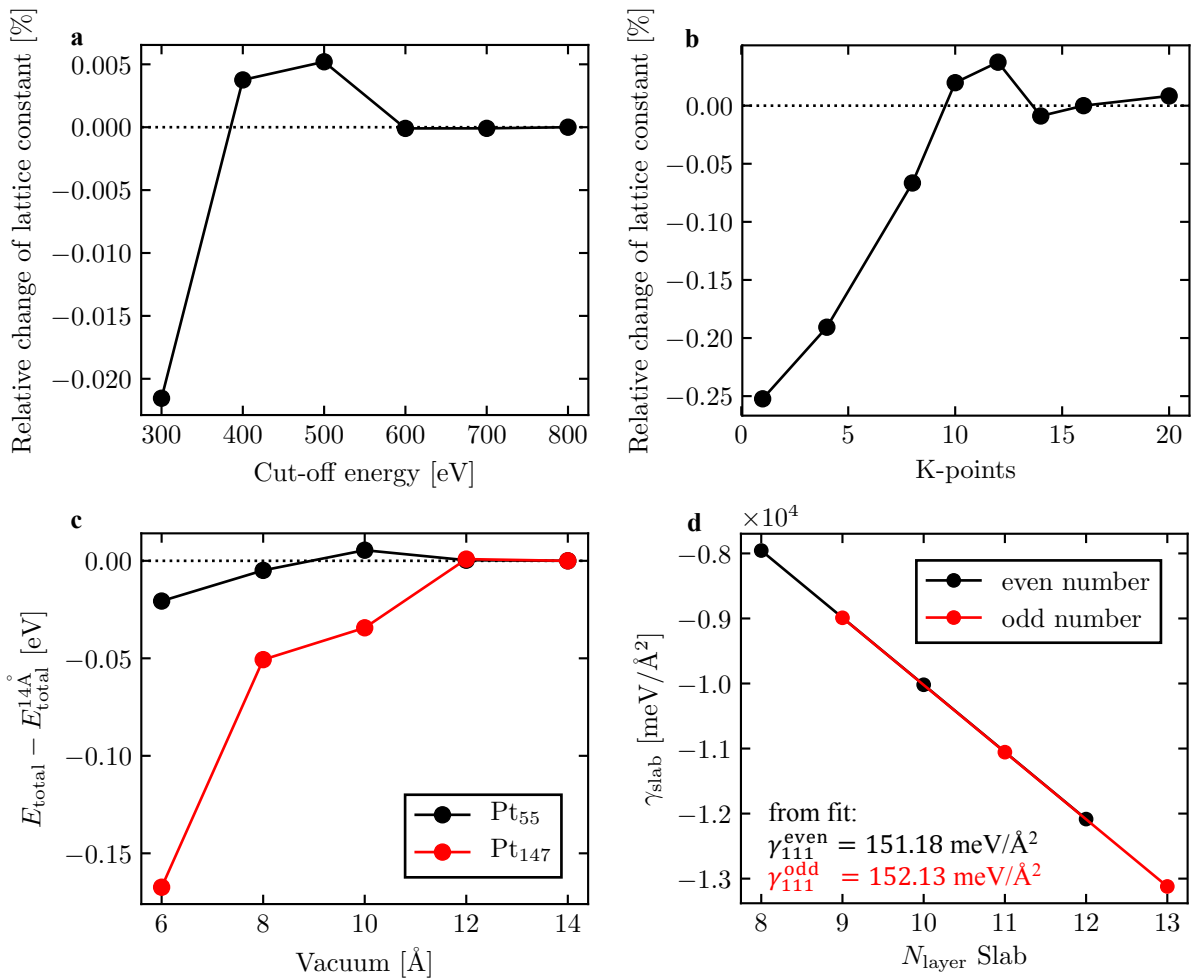


Figure 3.2: Relative change of the Pt lattice constant for (a) different cut-off energies with a (16,16,16) k-point grid and (b) density of k-point sampling with a $E_{\text{cut-off}} = 800$ eV. (c) Convergence of the total energy for Pt₅₅ and Pt₁₄₇ with the vacuum size in all dimensions. (d) Surface energy of various Pt (111) surfaces with different number of layers N_{layer} with surface energy calculated from the linear fit for even and odd numbers of layers.

Nanoparticle construction

The initial nanoparticle structures are constructed using the cluster module of the atomic simulation environment (ASE) package¹⁷⁸ and the PBE-D3 optimized bulk parameter (3.92 \AA in the case of Pt). For the other transition metals, the optimized structures of the Pt clusters were rescaled to the appropriate lattice constant (Table 3.1) and then fully relaxed. The coordination numbers for the different nanoparticle surface atoms are given in Table 9.3. For visualization, the diameter of the various clusters is derived from spherical particles: $d = ((6V_{\text{Pt}} \cdot N_{\text{Pt}})/\pi)^{1/3}$, with $V_{\text{Pt}} = 15.1 \text{ \AA}^3$, the volume¹⁷⁹ per bulk atom.

Calculation of surface energy

As already mentioned, the surface energy of a metal surface is obtained by a series of slab calculations with varying thickness from $N_{\text{layer}} = 8 \dots 13$. The total energies, E_{total} of the DFT calculations are used to plot the surface energy of the slab: $\gamma_{\text{slab}} = E_{\text{total}} \cdot 10^3 / A_{\text{slab}}$, with A_{slab} being the surface area of the slab. Using a linear fit of the either even or odd N_{layer} (see black and red points with line in Fig. 3.2d respectively), the surface energy is obtained as intersection with the y-axis. Because the slabs have two surfaces (bottom and top), the obtained values

have to be divided by two. The surface energies used in this work are the mean of the ones obtained for even and odd N_{layer} separately.

3.3 Shape and size effect for the example of Pt

To investigate the influence of particle size and shape on the thermodynamic stability of Pt, cuboctahedral, octahedral and cubic nanoparticles are chosen. While cubic nanoparticles consists only of (100) faces and octahedral only of (111), cuboctahedral nanoparticles have both, (100) and (111) faces, as shown in Figure 3.3a. The investigated sizes range from 0.72 nm (Pt₁₃) to 2.99 nm (Pt₉₂₃) for the cuboctahedral nanoparticles. Pt₆₃ to Pt₆₆₅ and Pt₁₉ to Pt₆₇₀ were investigated in the cubic and octahedral form ranging from 1.22 nm to 2.68 nm and 0.82 nm to 2.68 nm, respectively.

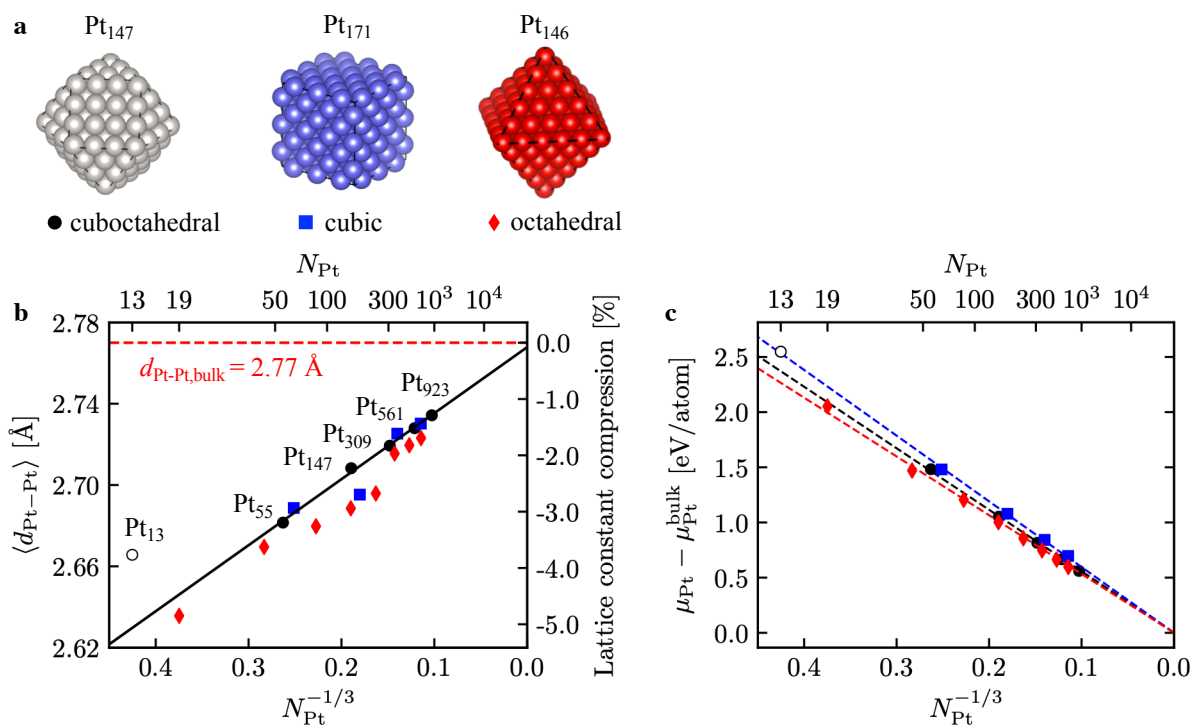


Figure 3.3: (a) Atomic structures of the cuboctahedral Pt₁₄₇, the cubic Pt₁₇₁ and the octahedral Pt₁₄₆ cluster. The colors correspond to the colors used for the symbols in (b) and (c). (b) Mean Pt-Pt distance $\langle d_{\text{Pt-Pt}} \rangle$ in Å of the relaxed nanoparticles, and (c) chemical potential μ_{Pt} relative to the bulk chemical potential of Pt $\mu_{\text{Pt}}^{\text{bulk}}$, both shown as a function of the number of Pt atoms per nanoparticle to the power of $-1/3$, $N_{\text{Pt}}^{-1/3}$ (lower abscissa). The upper abscissa shows the corresponding number of Pt atoms N_{Pt} . The hollow symbol represents Pt₁₃, which is excluded from the fit for cuboctahedral clusters. The black symbols in (b) of the cuboctahedral cluster are labeled with their corresponding number of atoms.

All investigated structures were fully relaxed and the obtained structures are thus local minima. This resulted in a contraction of the average nearest neighbor Pt-Pt distance for smaller clusters. Figure 3.3b shows the mean Pt-Pt distance $\langle d_{\text{Pt-Pt}} \rangle$ as a function of particle size compared to the bulk distance (2.77 Å). As shown previously for Pt¹⁸⁰ and other transition metals^{181–189}, it is found that $\langle d_{\text{Pt-Pt}} \rangle$ scales linearly when plotted against the number of Pt atoms to the power of $-1/3$, $N_{\text{Pt}}^{-1/3}$. The scaling is best for particles exhibiting the cuboctahedral shape (black dots) with the exception of the smallest Pt₁₃ cluster, which is attributed to quantum size effects. The chemical potential, which is approximated as the average energy per atom, $\mu_{\text{Pt}} = E_{\text{total}}/N_{\text{Pt}}$, is shown as a function of $N_{\text{Pt}}^{-1/3}$

in Figure 3.3c and a linear trend is observed for all three particle shapes investigated here. The slight differences in slope for the different shapes are due to the corresponding surface energies, with the fcc(111) surface having a smaller surface energy than the fcc(100) facet (compare Table 3.1).

Importantly, using the linear trend shown in Figure 3.3c the stability of a nanoparticle normalized to its number of atoms can be predicted using:

$$\mu_{\text{Pt}} - \mu_{\text{Pt}}^{\text{bulk}} = s_{\text{surface}} \cdot N_{\text{Pt}}^{-1/3} \quad (3.2)$$

For the cuboctahedral nanoparticles, a slope of: $s_{\text{surface}}^{\text{cuboctahedral}} = 5.57 \text{ eV}$ is found (cubic: $s_{\text{surface}}^{\text{cubic}} = 5.96 \text{ eV}$ and octahedral: $s_{\text{surface}}^{\text{octahedral}} = 5.33 \text{ eV}$). The steepest slope is obtained for cubic nanoparticles, which expose only (100) faces, which are higher in energy than (111) faces. Thus the slope obtained for octahedral nanoparticles is the flattest and the cuboctahedral case in between. Using this fit, the average stability per atom as a function of particle size is predicted as shown in Figure 3.4a (cubic: Figure 3.4c and octahedral: Figure 3.4e). Figure 3.4b shows the energy gained if two equally sized particles merge to form one larger particle. It can be seen that for small nanoparticles the gain in energy and thus the driving force for sintering is much higher than for larger nanoparticles. Similar images for the cubic and octahedral nanoparticles are shown in Figure 3.4d and Figure 3.4f respectively.

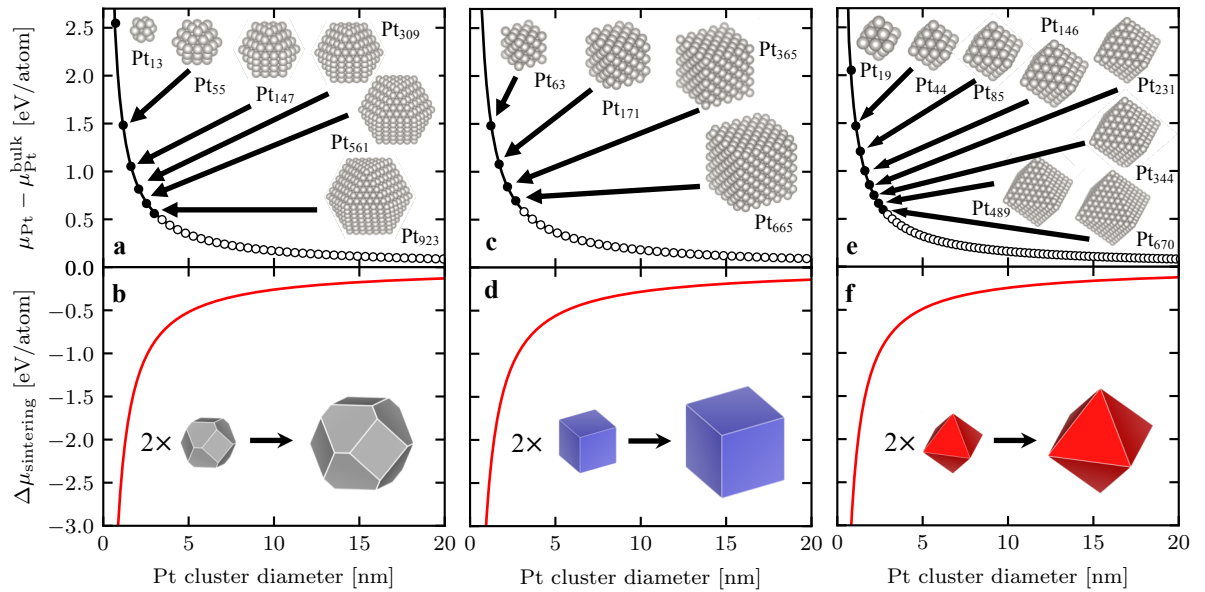


Figure 3.4: (a),(c),(e) Calculated and predicted chemical potential μ_{Pt} relative to the bulk chemical potential $\mu_{\text{Pt}}^{\text{bulk}}$ for (a) cuboctahedral, (c) cubic and (e) octahedral nanoparticles. The filled circles are values calculated using DFT and the hollow ones using the linear fit with $s_{\text{surface}}^{\text{cuboctahedral}} = 5.57 \text{ eV}$, $s_{\text{surface}}^{\text{cubic}} = 5.96 \text{ eV}$ and $s_{\text{surface}}^{\text{octahedral}} = 5.33 \text{ eV}$ according to eq. (3.2). All structures of the calculated nanoclusters are shown as inset. (b),(d),(f) Gain in chemical potential due to sintering under the assumption that two equally sized nanoclusters merge to form one larger particle for (b) cuboctahedral, (d) cubic and (f) octahedral nanoparticles.

Generally it is desirable to be able to predict the stability and shape of nanoparticles as shown in Figure 3.3c with simple models instead of performing explicit DFT calculations. The most widespread model for the prediction of nanoparticle shapes is the Wulff construction¹⁵, which will be presented in the next section 3.4.

3.4 Wulff construction

The surface energies of the different faces can be used to predict the relative stability of the nanoclusters:¹⁵

$$\gamma_{\text{NP}} = \sum_i \gamma_i A_i, \quad (3.3)$$

with γ_{NP} , the total surface energy of a nanoparticle, γ_i the surface energy of a crystal face in eV per surface atom and A_i the surface area of the crystal face.

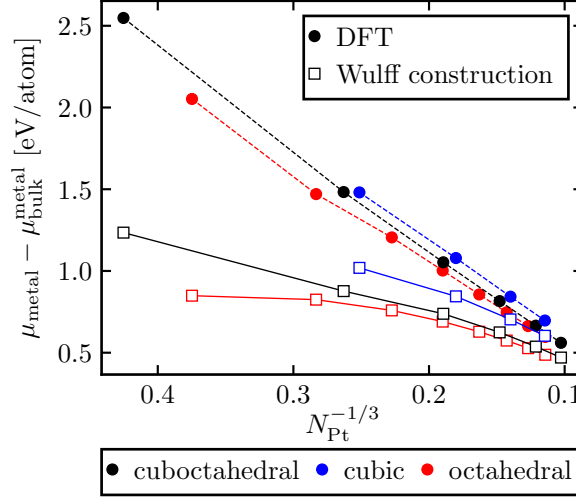


Figure 3.5: Chemical potentials of differently sized and shaped Pt nanoparticles. The filled circles show the chemical potential calculated with DFT and the open squares show the chemical potential according to the WC. The different colors represent different nanoparticle shapes, black: cuboctahedral, blue: cubic and red: octahedral.

The surface area of the (111) face and (100) face are calculated according to:

$$A_{111} = N_{111} \frac{\sqrt{3}a_0^2}{4} \text{ and } A_{100} = N_{100} \frac{a_0^2}{2}, \quad (3.4)$$

with $N_{111,100}$ being the number of atoms per (111) and (100) face respectively. Each cuboctahedral cluster consists of 8 (111) faces and 6 (100) faces, the cubic cluster of 6 (100) faces and the octahedral cluster of 8 (111) faces. The different energy contributions of the faces are listed in Table 9.4. Using eq. (3.3) to plot the chemical potential of different sized and shaped nanoparticles in Fig. 3.5, it can be seen that the Wulff construction overestimates the chemical potential of the nanoclusters, especially for small clusters. The reason is that for small nanoclusters the relative contribution of the edges and corners to the total surface energy is high but not included if only the surface energies are used. Therefore the WC will be extended to account also for the edges and corners by extrapolation from surface energies, as presented in the next section 3.5.

3.5 Pure metal nanoparticle stability model

3.5.1 Formalism

The energy of a nanoparticle is approximated to be additive, so that:

$$\mu^{\text{model}} = \mu^{\text{bulk}} \cdot N_{\text{atom}} + \sum_i^{N_{\text{surf}}} E(CN_i), \quad (3.5)$$

where μ^{model} is the total energy of a nanoparticle, N_{atom} its total number of atoms, N_{surf} its number of surface atoms and μ^{bulk} is the metal chemical potential. $E(CN_i)$ is the energy of a surface atom i with coordination number CN .

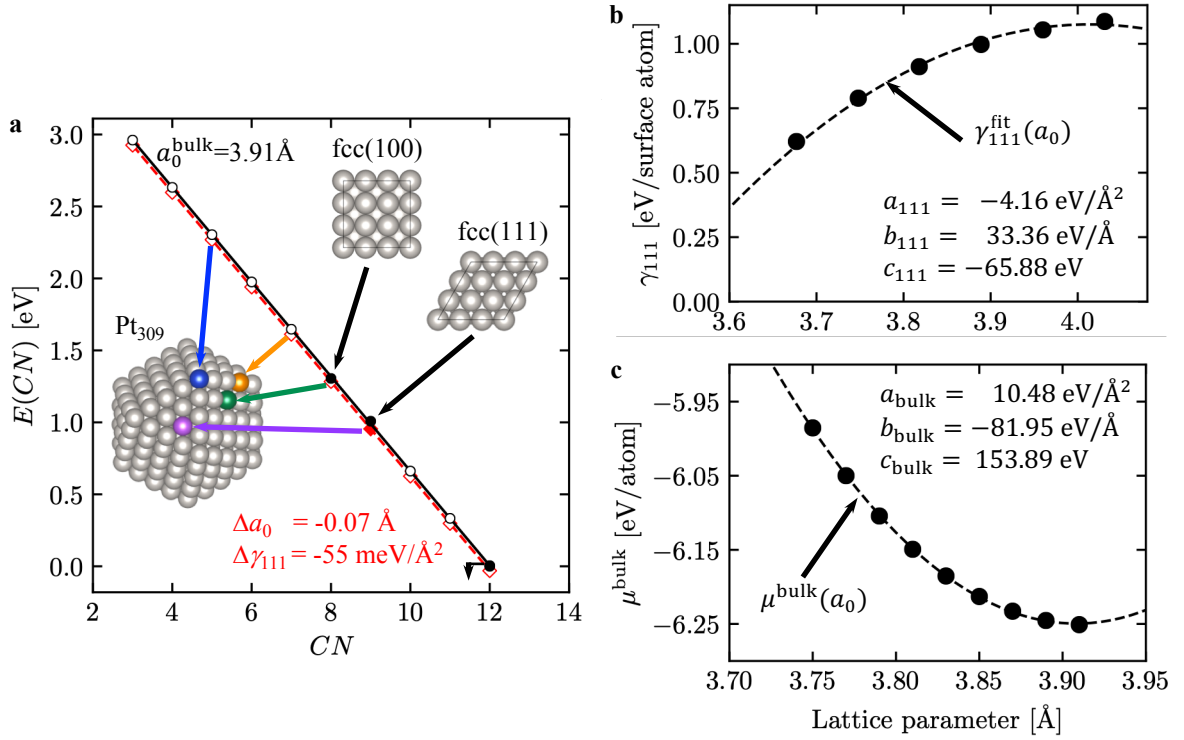


Figure 3.6: (a) Energy for surface atoms as a function of coordination number CN . The filled symbols were obtained with DFT calculations, the hollow ones from extrapolation. The circles represent the energy if the bulk lattice constant $a_0^{\text{bulk}} = 3.91 \text{ \AA}$ is used and the squares if the lattice constant derived from the $\langle d_{\text{Pt-Pt}} \rangle$ of Pt_{309} is used, $a_0^{\text{Pt}_{309}} = 3.77 \text{ \AA}$. The insets show the fcc(111) and fcc(100) surface respectively and the Pt_{309} cluster with its different possible CN numbers highlighted in colors (violet: $CN = 9$, green: $CN = 8$, yellow: $CN = 7$, blue: $CN = 5$). (b) Quadratic fit of the fcc(111) surface energy per atom, $\gamma_{111}^{\text{fit}}(a_0)$ and (c) quadratic fit of $\mu^{\text{bulk}}(a_0)$ for different lattice parameters of platinum.

As shown for the example of Pt in Figure 3.6a, the surface energies at the bulk lattice constant a_0^{bulk} of the fcc(111) and fcc(100) surfaces are used to determine the energy of 9-fold and 8-fold coordinated surface atoms relative to that of a 12-fold coordinated bulk atom. Assuming a linear increase¹⁶⁶ of the energy with the coordination number CN of the atom results in the scaling shown in Figure 3.6a with the solid black line. Within this simple approximation, the chemical potential of a cluster can be predicted based on its number of atoms and their corresponding coordination numbers. However, as shown in Figure 3.3b, the relaxation of the nanoparticles leads to a reduction of the $\langle d_{\text{Pt-Pt}} \rangle$. In order to account for this effect, both, the surface energies and the cohesive energies are determined as a function of the lattice constant a_0 . Within the relevant range (-5%), the surface energy always decreases when a_0 is lowered with respect to the bulk lattice constant (Figure 3.6b). The bulk energy, on the other hand, will increase (Figure 3.6c) whenever a_0 deviates from its bulk value (a_0^{bulk}), thus counteracting the particle contraction induced by the surface energy. This qualitatively explains the trends observed in Figure 3.3b: Smaller particles with a larger fraction of surface atoms contract more since the decrease in surface energy outweighs the increase in the cohesive energy. However, the contraction of the particles can also readily be predicted quantitatively since $\gamma_{111}(a_0)$ and $\mu^{\text{bulk}}(a_0)$ as obtained from DFT calculations, are well described by quadratic functions, as can be seen in Figures 3.6b and c. Explicitly, the lattice dependence of the surface energy is defined as:

$$E(CN) = c(a_0^{\text{bulk}}) \cdot CN + b(a_0), \quad (3.6)$$

with $b(a_0) = \gamma_{111}^{\text{fit}}(a_0) - 9 \cdot c(a_0^{\text{bulk}})$, giving:

$$E(CN) = c(a_0^{\text{bulk}})(CN - 9) + \gamma_{111}^{\text{fit}}(a_0) \quad (3.7)$$

where $\gamma_{111}^{\text{fit}}(a_0)$ is the surface energy of the (111) face per atom in eV depending on a_0 . Using the lattice constant resulting from $\langle d_{\text{Pt-Pt}} \rangle$ of the Pt₃₀₉ nanoparticle, $a_0^{309} = 3.77 \text{ \AA}$, and eq. (3.7) results into the red dotted line in Figure 3.6a. Inserting eq. (3.7) into eq. (3.5) and dividing by the number of atoms gives:

$$\frac{\mu^{\text{model}}(a_0)}{N_{\text{atom}}} = \mu^{\text{bulk}}(a_0) + \frac{N_{\text{surf}} \cdot \gamma_{111}^{\text{fit}}(a_0) + \sum_{CN} N_{CN} \cdot c(a_0^{\text{bulk}})(CN - 9)}{N_{\text{atom}}}. \quad (3.8)$$

For a given cluster with known coordination numbers, this gives a simple, analytical expression for the chemical potential as a function of the lattice constant, which can be minimized.

3.5.2 Results

As already mentioned, the trends described in Fig. 3.3 are not unique to Pt¹⁸⁰, but have also been observed for other transition metals, for example Pd^{181,182}, Ru¹⁸⁴ and Au¹⁸⁵, but also main group metals like Al¹⁸⁵ or alkaline earth metals like Mg^{185,186}. With this in mind transition metals of group 8, 9, 10 and 11 as well as Mg and Al were investigated. Figure 3.7a shows the difference $\mu_{\text{metal}} - \mu_{\text{metal}}^{\text{bulk}}$ vs. $N^{-1/3}$ for cuboctahedral nanoparticles with 55, 147, 309 and 561 atoms. As can be seen in Figure 3.7a, all metals follow the same behavior described in eq. (3.2), but with different slopes. In Figure 3.7b, the slope obtained from Figure 3.7a with eq. (3.2), is plotted against the bulk chemical potential of the corresponding metals as filled circles. The quality of the observed correlation can be attributed to the fact that the surface and cohesive bulk energy are strongly correlated, as shown in Figure 3.7c. The slopes predicted for these metals are compared in Figure 3.7b and Table 3.6 to the ones obtained directly from DFT calculations. With the exception of Ir, all predicted slopes are higher than the results from the DFT calculations with a MAE of 0.54 eV/atom. From the parity plot shown in Figure 3.7d it can be seen that the agreement between DFT calculations and our model improves with increasing cluster size. For the predicted chemical potentials of the different metals the agreement is very good and overall the MAE for the prediction of all clusters investigated in this work is only 0.09 eV/atom with the maximum error being 0.32 eV/atom.

Table 3.6: Fitted slope $s_{\text{surface}}^{\text{DFT}}$ from plotting $\mu_{\text{metal}}^{\text{DFT}} - \mu_{\text{metal}}^{\text{bulk}}$ vs. $N_{\text{atoms}}^{-1/3}$ of the values in column 4 of Table 9.5. $s_{\text{surface}}^{\text{model}}$ is the fitted slope of $\mu_{\text{metal}}^{\text{model}} - \mu_{\text{metal}}^{\text{bulk}}$ vs. $N_{\text{atoms}}^{-1/3}$ for the values in column 5 of Table 9.5. The mean absolute error of the slopes is MAE = 0.54 eV/atom.

Metal	Slope DFT [eV]	Slope Model [eV]
Ag	2.97	3.70
Au	3.42	3.91
Co	4.91	5.43
Cu	3.76	4.46
Ir	7.35	7.28
Ni	4.52	4.81
Os	8.18	8.81
Pd	4.49	5.35
Pt	5.57	5.86
Rh	6.01	6.72
Ru	6.75	7.55
Al	2.58	3.00
Mg	2.32	2.83

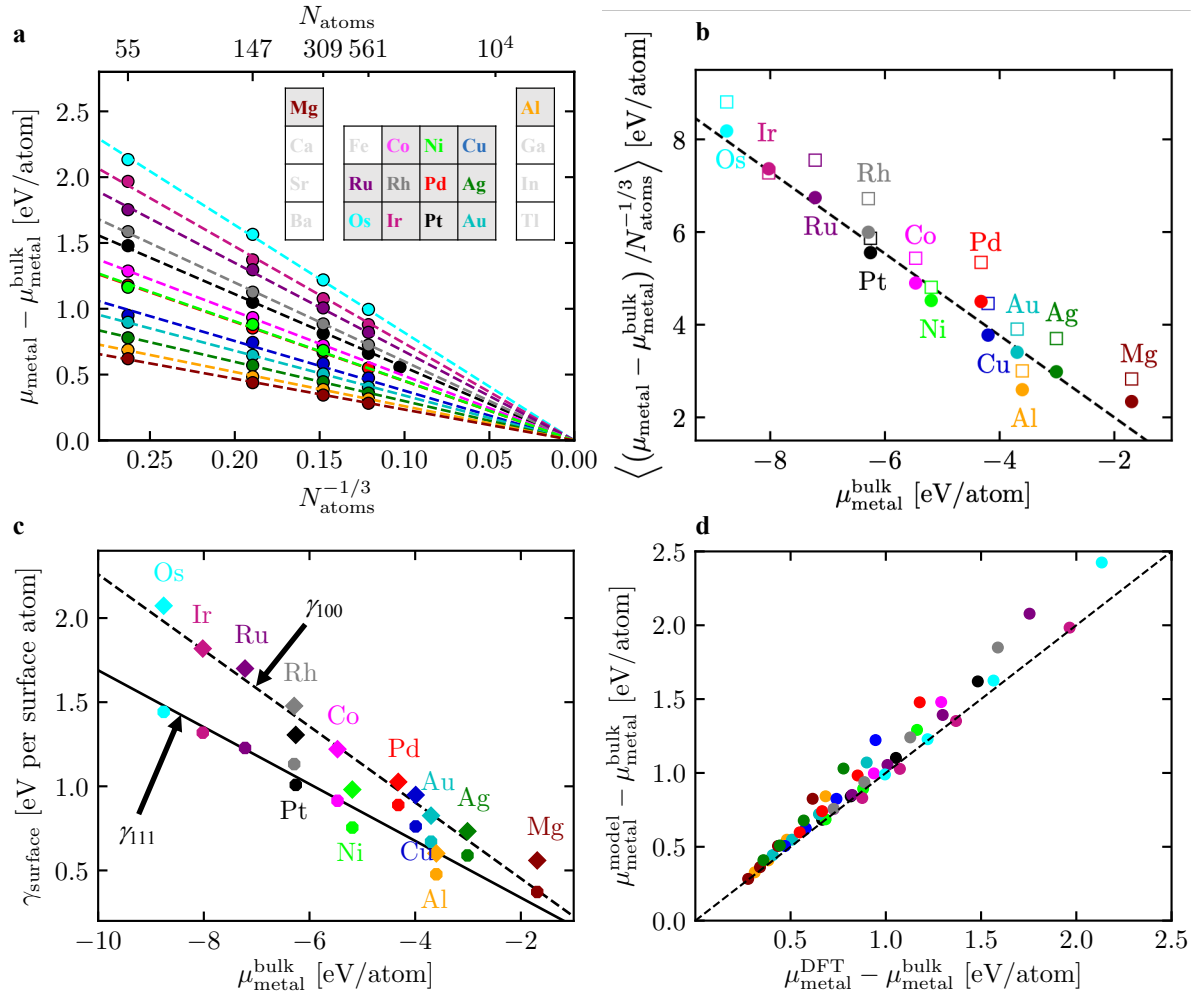


Figure 3.7: (a) $\mu_{\text{metal}} - \mu_{\text{metal}}^{\text{bulk}}$ vs. $N^{-1/3}$ for different metals. (b) Slope, obtained with eq. (3.2), vs. the bulk chemical potential of the corresponding metal. The filled circles are fitted from (a) and the hollow square symbols are the results of fitting the chemical potentials to nanoparticle sizes as shown in (a) calculated with the stability model. The corresponding total energies and chemical potentials are given in Table 9.5 and the slopes in Table 3.6. (c) Correlation of the γ_{111} and γ_{100} surface energies in eV per surface atom with the bulk chemical potential of the investigated metals. (d) Parity plot of the relative stability obtained using the stability model versus the values calculated with DFT. The obtained MAE is 0.09 eV/atom. The color code is the same as shown in the inset of (a).

3.6 Conclusions

In summary, a simple model that is able to predict the stability of nanoparticles as a function of size and shape based on the coordination numbers of the surface atoms and the lattice constant dependent $\gamma_{111}(a_0)$ and $\mu^{\text{bulk}}(a_0)$ was described. The simple stability model is shown to be highly accurate and reproduces the results of DFT calculations with a MAE of only 0.09 eV/atom for the symmetric and well-defined nanoparticles studied in this work. Importantly, this allows to estimate the thermodynamic stability of a whole set of transition metal particles of various sizes towards sintering. However, the thermodynamic stability of gas phase clusters is only one step in the direction to understand the complex behavior of different heterogeneous catalysts. The influence of different supports and adsorbates on the nanoparticle stability is an additional challenge as well as the kinetic sintering processes.

4 Support effects on nanoparticle stability

4.1 Introduction

Studying metal-oxide interfaces is generally difficult, both from the experimental and theoretical side. Experimentally, a lot has been learned from secondary effects, e.g. how the support directly affects properties such as catalytic activity or catalyst deactivation.¹⁴ Detailed information about the atomic structure and the strength of metal-support interactions can be obtained from particle shape analysis and micro calorimetry.^{20,21,190,191} Computational investigations with density functional theory (DFT) either employ finite nanoparticles on extended supports or periodic interfaces between metal- and oxide-surfaces. Both approaches are complimentary in that adhesion between surfaces captures the intrinsic reactivity of these surfaces, whereas the adhesion of nanoparticles additionally includes finite size effects and averages over extended facets and under-coordinated atoms on edges and corners.^{89,192–194} Adhesion energies of Au₂₂-clusters have been found to be 2-3 times larger than those of extended Au-surfaces for three studied oxide surfaces.¹⁹⁵ There are relatively few systematic theoretical investigations of adhesion of metal-support interfaces.^{92,196–199} Campbell and coworkers have recently analyzed experimental data and identified trends, where experimental descriptors such as the heat of formation of bulk oxides have been used to rationalize the observed variations in the adhesion energies.²⁰ In this chapter, the interfaces between fcc(111)- and fcc(100)-surfaces of common transition metals and several oxide supports are investigated using DFT at the PBE-D3 level of theory. The goal is to find trends in adhesion energies and to identify computational descriptors that allow to predict adhesion energies.

4.2 Computational details

4.2.1 Interface models

The main challenge in computing interface energies is that oxide and metal surfaces usually have incommensurate unit cells. Small or medium sized clusters can be expected to adapt to the structure of the support more easily than larger clusters.^{36,200,201} However, the focus is on the situation where the number of layers of both metal and support are large compared to the area of the interface. In this limit, both metal and support will not deviate from their respective bulk lattice constants.^{190,202} In calculations with periodic boundary conditions, either one or both of the surfaces have to be stretched or compressed to be accommodated into the same unit cell. It was generally found that oxides are less sensitive to a change of the lattice constants, while metals may reorganize to structures that deviate significantly from their bulk crystal structure. Thus, all interface models constructed in this work keep the metal surface in its equilibrium lattice constant and adjust the lattice constant of the oxide, with the goal of introducing as little artificial strain on the oxide as possible. The lowest layers of the oxides are kept frozen while all remaining atoms of the interface are fully relaxed. In the case of non-stoichiometric oxides, the dangling bonds of the bottom side are saturated by hydrogen. Initial structures were constructed by placing the metal slab approximately 2 Å above the oxide surface, which had before been scaled to match the lattice constants of the metal. All structures were initially relaxed for the interface with Pt and the other interfaces were then obtained from these structures by adjusting the lattice constants and replacing Pt by the respective metal. Table 4.1 lists the

This chapter is based on the following publication: Dietze, E. M.; Plessow, P. N., Predicting the Strength of Metal–Support Interaction with Computational Descriptors for Adhesion Energies. *J. Phys. Chem. C* 2019, 123, 33, 20443-20450.

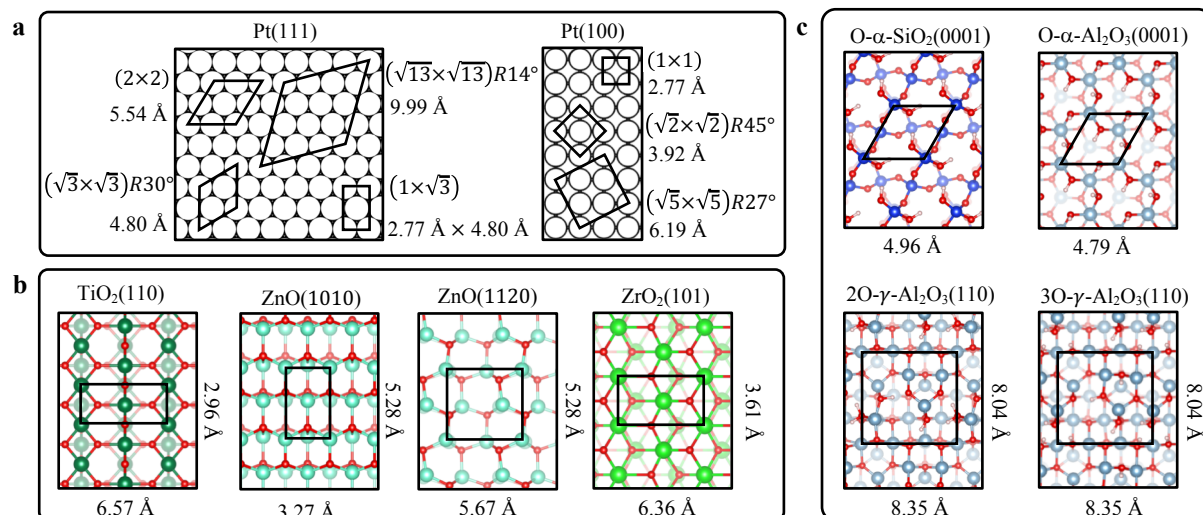


Figure 4.1: Atomic structure of the surfaces used to construct the interfaces studied in this work and the dimension of the corresponding unit cells. (a) Hexagonal Pt(111) unit cells, the rectangular Pt(111) unit cell abbreviated $(1 \times \sqrt{3})$ and quadratic Pt(100) unit cells. (b) Stoichiometric surfaces with the 110-surface of rutile, the $10\bar{1}0$ -surface and $11\bar{2}0$ -surface of ZnO in wurtzite structure and the 101-surface of tetragonal zirconia. (c) Hydroxylated surfaces with the fully hydroxylated 0001-surface of α -quartz, the fully hydroxylated 0001-surface of α -alumina and the partially hydroxylated 110-surface of γ -alumina including two and three adsorbed water molecules per unit cell.

considered super cells and in the last column the strain applied to the oxide to form the interface for the example of Pt. The strain introduced by the interface formation for the other metals is given in Table 9.6 for the case of symmetric strain and Table 9.7 for the unsymmetric case.

The metal surfaces considered are either in the fcc(111) or fcc(100) structure and are all transition metals: Ru, Os, Rh, Ir, Ni, Pd, Pt, Cu, Ag and Au. It is noted that Ru and Os crystallize in hcp structure. The relevant unit cells are shown in Figure 4.1a for the example of Pt.

The oxide surfaces considered in this work are shown in Figure 4.1b,c. Hydroxylated surfaces that can be derived from α -SiO₂(0001)^{32,203}, α -Al₂O₃(0001)^{204–206} and γ -Al₂O₃(110) are studied. γ -Al₂O₃ is commonly used experimentally and the crystalline Digne-model^{207–209} is studied, where two relevant hydroxylation stages are employed with two and three water molecules per unit cell, abbreviated 2O- γ -Al₂O₃(110) and 3O- γ -Al₂O₃(110). Only the oxidized surfaces resulting from full hydroxylation, denoted O- α -SiO₂(0001) and O- α -Al₂O₃(0001), were considered for these materials. The remaining oxide surfaces are all stoichiometric.

To demonstrate that using the oxide lattice constant instead of that of the metal lattice influences the results only little, Figure 4.2 shows the difference in adhesion energy for various metal/oxide interfaces obtained with either the oxide lattice constant or the metal lattice constant for the unit cell. The deviation in adhesion energy increases with increasing strain, but for small strain (up to 5%) it remains below 30 meV/Å². A detailed comparison of the calculated adhesion energies is given in Table 9.12 and the corresponding total energies in Table 9.13.

Table 4.1: Supercells used in the calculation of adhesion energies are listed separately for metal and oxide surfaces. The first index of the oxide supercell refers to the horizontal lattice vector of the unit cells depicted in Figure 4.1. The type of termination (oxidized or stoichiometric) is listed along with the strain applied to the oxide to form the interface for the example of Pt.

Oxide			Metal		Interface with Pt	
Surface and termination		Supercell	Surface	Supercell	Strain ^a [%]	
O- α -SiO ₂ (0001)	ox.	1 × 1	fcc(111)	2 × 2	11.7	11.7
		1 × 1		($\sqrt{3} \times \sqrt{3}$)R30°	-3.3	-3.3
		2 × 2		($\sqrt{13} \times \sqrt{13}$)R14°	0.7	0.7
O- α -Al ₂ O ₃ (0001)	ox.	1 × 1	fcc(111)	($\sqrt{3} \times \sqrt{3}$)R30°	0.3	0.3
		2 × 2		($\sqrt{13} \times \sqrt{13}$)R14°	4.3	4.3
2O- γ -Al ₂ O ₃ (110)	ox. ^b	1 × 1	fcc(100)	3 × 3	-0.5	3.4
3O- γ -Al ₂ O ₃ (110)	ox. ^c	1 × 1	fcc(100)	3 × 3	-0.5	3.4
TiO ₂ (110)	stoich.	2 × 1	fcc(100)	5 × 1	5.4	-6.4
		3 × 1		7 × 1	-1.6	-6.4
		4 × 1		9 × 1	-5.1	-6.4
		1 × 2		($\sqrt{5} \times \sqrt{5}$)R27°	-5.7	4.6
		3 × 5		fcc(111)	7 × 3 $\sqrt{3}$	-1.6
ZnO(10 $\bar{1}$ 0)	stoich.	4 × 1	fcc(100)	5 × 2	5.8	4.9
		5 × 1		6 × 2	1.5	4.9
		1 × 3		fcc(111)	2 × 2 $\sqrt{3}$	4.9
ZnO(11 $\bar{2}$ 0)	stoich.	1 × 1	fcc(100)	2 × 2	-2.3	4.9
		2 × 3		(3 $\sqrt{2} \times 4\sqrt{2}$)R45°	1.5	4.9
ZrO ₂ (101)	stoich.	3 × 3	fcc(100)	7 × 4	1.6	2.4

^a The strain of the oxide with respect to the two lattice vectors of the surface is listed.

^b Derived from the hydroxylated surface with two water per surface unit cell.

^c Same as b but with three water per surface unit cell.

Convergence of adhesion energy with respect to the number of oxide layers

To show the convergence of the results against the number of oxide layers, the Pt/O- α -SiO₂(0001) interface is used as an example with various numbers of layers, ranging from 1 to 5. The first layer in the 1 × 1 O- α -SiO₂(0001) unit cell consists of 4 SiO₂ groups. The following layers each contain 3 SiO₂ groups to have the same hydrogen saturated oxygen atoms at the bottom of the slab. The complete structure is relaxed for the convergences test. It is found that already after the first layer, the adhesion energy varies at most by 1.2 meV/Å². The calculated total energies and adhesion energies are given in Table 4.2.

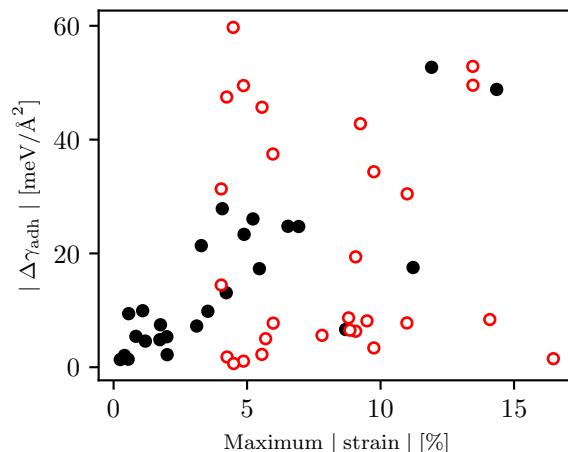


Figure 4.2: Absolute change in the adhesion energy when using either the metal lattice constant or the oxide lattice constant as a function of the absolute maximum strain of the metal/oxide interface. The black circles denote interfaces with symmetric strain (α -SiO₂ and α -Al₂O₃) and the red, hollow circles asymmetric strain on the unit cell. In the case of asymmetric strain the absolute maximum strain is used. The corresponding interfaces and values are shown in Table 9.12.

Table 4.2: Convergence of the adhesion energy γ_{adh} in meV/Å² (last column) with the number of SiO₂ groups per unit cell $N(\text{SiO}_2)$ using the example of the Pt/O- α -SiO₂(0001) interface. The adhesion energy is calculated according to eq. (4.4) with the interface energy $E_{\text{Interface}}$, oxide energy E_{Oxide} , metal energy E_{Metal} in eV and the stability difference between hydroxylated and oxidized surface per supercell $\Delta\gamma_{\text{ox-lat}}^{\text{ox}}$.

$N(\text{SiO}_2)$	$E_{\text{Interface}}$	E_{Oxide}	E_{Metal}	$\Delta\gamma_{\text{ox-lat}}^{\text{ox}}$	γ_{adh}
4	-192.75	-125.17	-76.28	272.03	-181.30
7	-264.77	-197.19	-76.28	272.03	-180.94
10	-336.84	-269.24	-76.28	272.03	-182.15
13	-408.90	-341.32	-76.28	272.03	-181.45
16	-480.96	-413.36	-76.28	272.03	-182.16

4.2.2 DFT parameters

All DFT-calculations were performed with the PBE¹²⁶ functional and the D3-dispersion correction¹⁴³ using the VASP program package in version 5.4.1 and the projector-augmented-wave (PAW) method with standard PAW-potentials.¹⁵³ A cutoff of 400 eV was used for the expansion of the orbitals in plane-waves, along with Gaussian smearing with a width of 0.1 eV and Γ -centered k-point sampling with k-point densities between 10×10 and 16×16 per fcc(111)-(1 \times 1) unit cell, depending on the specific interface. The used k-points for each surface are listed in Table 4.3. Only surfaces involving Ni were computed with spin-polarized calculations. All structures were optimized until atomic forces were below 0.01 eV/Å. The interface calculations are often very time consuming, due to system size and sometimes slow SCF- and geometry convergence. It was therefore not possible to obtain interfaces for all potential combinations of oxides and metal surfaces. Additionally, interfaces were discarded when the strain on the oxide resulted in a visible deformation of the strained clean oxide surface.

Table 4.3: Surface dependent Γ -centered k-point sampling.

Oxide surface	Metal surface	Metal supercell	K-points
O- α -SiO ₂ (0001)	fcc(111)	2×2	(8,8,1)
		$(\sqrt{3} \times \sqrt{3})R30^\circ$	(8,8,1)
		$(\sqrt{13} \times \sqrt{13})R14^\circ$	(3,3,1)
O- α -Al ₂ O ₃ (0001)	fcc(111)	$(\sqrt{3} \times \sqrt{3})R30^\circ$	(8,8,1)
		$(\sqrt{13} \times \sqrt{13})R14^\circ$	(3,3,1)
2O- γ -Al ₂ O ₃ (110)	fcc(100)	3×3	(4,4,1)
3O- γ -Al ₂ O ₃ (110)	fcc(100)	3×3	(4,4,1)
TiO ₂ (110)	fcc(100)	5×1	(2,10,1)
		7×1	(2,10,1)
		9×1	(1,10,1)
		$(\sqrt{5} \times \sqrt{5})R27^\circ$	(5,5,1)
		$7 \times 3\sqrt{3}$	(2,2,1)
ZnO(10 $\bar{1}$ 0)	fcc(111)	$7 \times 3\sqrt{3}$	(2,2,1)
	fcc(100)	5×2	(2,5,1)
ZnO(11 $\bar{2}$ 0)	fcc(100)	6×2	(2,5,1)
		$2\sqrt{3} \times 2$	(3,6,1)
		2×2	(6,6,1)
ZrO ₂ (101)	fcc(100)	$3\sqrt{2} \times 4\sqrt{2}$	(3,2,1)
		7×4	(2,3,1)

The optimized lattice constants for the metals are the same as presented in Table 3.1. The lattice parameters of the oxide surfaces and their corresponding surface area are given in Table 4.4.

Table 4.4: Unit cell surface area in \AA^2 of the oxide surfaces and the surface lattice parameters in \AA .

Oxide surface	Surface area	Lattice parameter	
		a	b
O- α -SiO ₂ (0001)	21.33	4.962	
O- α -Al ₂ O ₃ (0001)	19.85	4.787	
2O- γ -Al ₂ O ₃ (110)	67.11	8.035	8.352
3O- γ -Al ₂ O ₃ (110)	67.11	8.035	8.352
TiO ₂ (110)	19.45	6.569	2.960
ZnO(10 $\bar{1}$ 0)	17.30	3.274	5.283
ZnO(11 $\bar{2}$ 0)	29.96	5.671	5.283
ZrO ₂ (101)	22.95	6.361	3.608

Adsorption energies of oxygen atoms were computed at a coverage of $\theta = 1/9$ on fcc(111) and fcc(100) surfaces. The surfaces consists of 4 layers of which the lower two are frozen to mimic the bulk metal and the upper two relaxed. $(4 \times 4 \times 1)$ Γ -centered k-points are used. The oxygen adsorption energies are summarized in Table 4.5.

Table 4.5: Oxygen adsorption energy in eV on fcc(111) and fcc(100) metal surfaces with 1/9 oxygen coverage. As oxygen reference $0.5 \cdot E_{O_2} = -4.93$ eV is chosen.

Metal	fcc(111)	fcc(100)
Ag	-0.44	-0.90
Au	-0.12	-0.06
Cu	-1.49	-2.06
Ir	-1.77	-2.17
Ni	-2.40	-2.72
Pd	-1.52	-1.34
Pt	-1.13	-1.34
Os	-2.63	-2.74
Rh	-2.14	-2.32
Ru	-2.92	-3.09

4.2.3 Role of van der Waals interactions

The zero-damping D3 approach developed by Grimme is used to compute van-der-Waals (vdW) interactions.¹⁴³ The vdW-part of the adhesion energy can therefore be easily separated and is shown in Figure 4.3a for the metal/oxide interfaces of $TiO_2(110)$, $O-\alpha-Al_2O_3$ and $O-\alpha-SiO_2$ as example. Figure 9.1 shows the D3 correction of the other considered surfaces. The vdW-interactions are relatively similar for all interfaces, typically around -60 to -80 meV/Å². They are notably weaker for $\alpha-SiO_2$, which can be explained by its low bulk density that also leads to significantly reduced vdW-interactions of $\alpha-SiO_2$ with itself in the bulk oxide, compared to the other oxides studied here, see Table 4.6. The vdW-interaction in $\gamma-Al_2O_3$ is also relatively weak, which is attributed to its corrugated surface. Since the vdW-interactions are generally similar for different metals, they do not significantly alter the slope a_{ox} in the scaling relations, but mainly shift the offset b_{ox} . The D3-correction with Becke-Jones-damping leads generally to somewhat weaker adhesion with differences typically around 20 meV/Å² see Figures 4.3b and 9.2.

Table 4.6: VdW-energy with zero damping per volume for bulk oxides and vdW-energy with zero damping per atom of bulk metals.

Oxide	E_{vdW}/V [meV/Å ³]	Metal	E_{vdW} [eV]
$\alpha-SiO_2$	-7.509	Ag	-0.505
$\alpha-Al_2O_3$	-18.115	Au	-0.670
$\gamma-Al_2O_3$	-15.773	Cu	-0.525
TiO_2	-16.581	Ir	-0.719
ZnO	-16.606	Ni	-0.413
ZrO ₂	-16.127	Pd	-0.592
		Pt	-0.783
		Os	-0.595
		Rh	-0.587
		Ru	-0.563

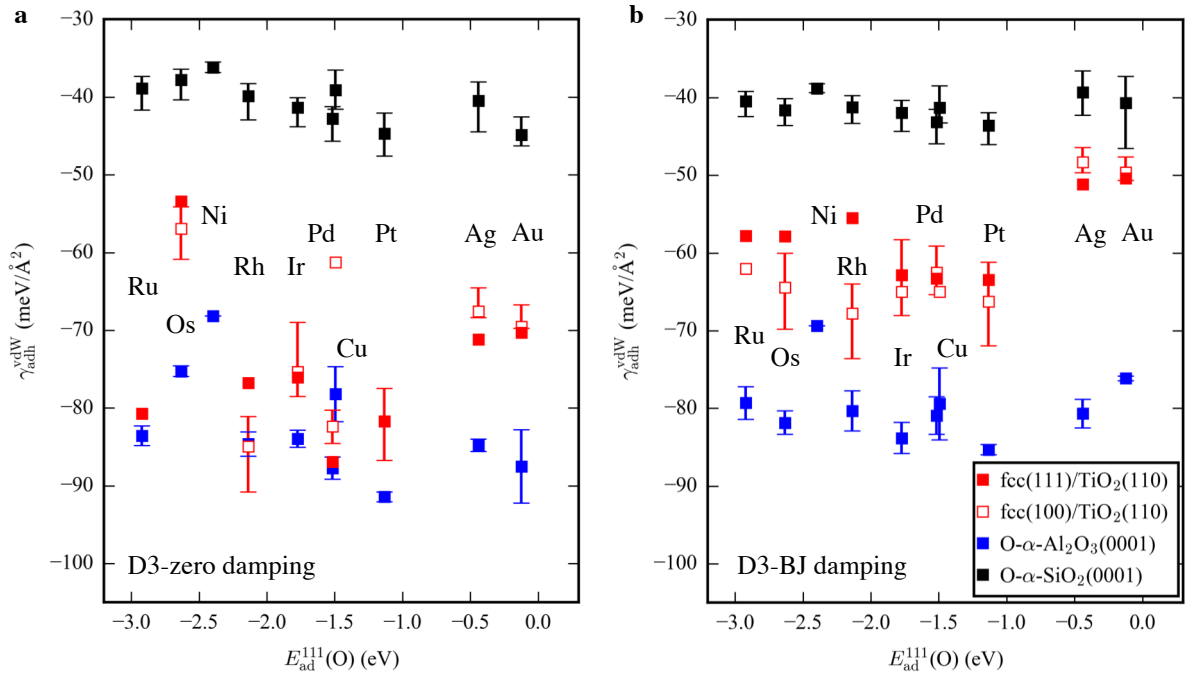


Figure 4.3: Interfaces formed by oxygen-rich oxide surfaces that can be derived from hydroxylated surfaces and stoichiometric oxide surfaces. VdW contributions with (a) D3-zero damping and (b) D3-BJ damping of adhesion energies are shown as a function of oxygen adsorption energies on clean fcc(111) metal surfaces. The vdW contributions of the adhesion energies were averaged over all computed supercells and the largest and smallest deviation within these individual calculations is indicated with error bars.

4.2.4 Calculation of adhesion energies

The adhesion energy of stoichiometric interfaces was calculated as:

$$\gamma_{\text{adh}}^{\text{stoich}} = (E_{\text{M-lat}}^{\text{interf}} - E_{\text{M-lat}}^{\text{M}} - E_{\text{M-lat}}^{\text{ox}}/A_{\text{M-lat}}), \quad (4.1)$$

where E denotes the total energy of a slab and A the area of a slab. The superscript denote interface (interf), metal (M) or oxide (ox). The subscript signifies if the quantity is computed with the structure in the lattice constant of the oxide (ox-lat) or of the metal (M-lat). It is found that using $A_{\text{M-lat}}$ results in somewhat better scaling relations for the stoichiometric surfaces. For a small lattice mismatch, the difference between $A_{\text{ox-lat}}$ and $A_{\text{M-lat}}$ is small. This calculation is illustrated in Figure 4.4a for Pt(111) supported on the (110) surface of rutile. Both surfaces, which are first optimized separately using the same lattice constant, are then brought into contact. The gain in energy (-24.1 eV) per area of the supercell (279 \AA^2) results in an adhesion energy per area of -86 meV/\AA^2 .

For the adhesion energies of the oxidized surfaces, first the hydroxylated surface is used and the adhesion energies calculated under the liberation of $n/2 \text{ H}_2$ -molecules, where n is the number of hydroxyl groups per unit cell.

$$\gamma_{\text{adh}}^{\text{hydrox}} = (E_{\text{M-lat}}^{\text{interf}} - E_{\text{M-lat}}^{\text{M}} + n/2 \cdot E(\text{H}_2) - E_{\text{M-lat}}^{\text{hydrox}})/A_{\text{ox-lat}}, \quad (4.2)$$

Here $A_{\text{ox-lat}}$ is used, since in this way, different supercells have the same, correct concentration of hydroxyl groups as in the ideal interface. Adhesion energies of oxidized interfaces were calculated by accounting for the difference between hydroxylated and oxidized surface, as computed for the unstrained oxide surface:

$$\gamma_{\text{adh}}^{\text{ox}} = \gamma_{\text{adh}}^{\text{hydrox}} - \Delta\gamma_{\text{ox-lat}}^{\text{ox}} \quad (4.3)$$

where the stability difference between hydroxylated and oxidized surfaces is given by:

$$\Delta\gamma_{\text{ox-lat}}^{\text{ox}} = (E_{\text{ox-lat}}^{\text{ox}} - E_{\text{ox-lat}}^{\text{hydrox}} + n/2 \cdot E(\text{H}_2)) / A_{\text{ox-lat}}. \quad (4.4)$$

This procedure was used since the hydroxylated surfaces are thermodynamically most stable under relevant conditions for α -SiO₂(0001), α -Al₂O₃(0001) and γ -Al₂O₃(110). The shifts $\Delta\gamma_{\text{ox-lat}}^{\text{ox}}$ that allows to relate adhesion energies referenced to the oxidized surface ($\gamma_{\text{adh}}^{\text{ox}}$) to hydroxylated surfaces ($\gamma_{\text{adh}}^{\text{hydrox}}$) are listed in Table 4.7. The clean oxidized oxide surfaces derived from the hydroxylated surfaces by removing the surface hydrogen atoms (H) were relaxed only for the unstrained oxide, using spin-polarized calculations. It is noted that the obtained structures are not very stable and partially react under the formation of peroxy structures, e.g. under the formation of O-O bonds. However, the energetic difference between different oxidized structures using different supercells and magnetic states turned out to be relatively small (30 meV/Å²) compared to $\Delta\gamma_{\text{ox-lat}}^{\text{ox}}$. These oxidized surfaces only serve as an artificial reference to be able to directly compare the adhesion energies of oxidized surfaces to those of stoichiometric surfaces, which is otherwise difficult since the formation of oxidized interfaces from hydroxylated surfaces always depends on the chemical potential of hydrogen. Adhesion free energies for any temperature and H₂-pressure can be obtained by computing the free energy of H₂ at those conditions, multiplying by the number of formed hydrogen atoms per unit cell ($n/2$, see Table 4.7) and dividing by the unit cell area (Table 4.4). In this way one can also easily compute the adhesion free energy in the presence of O₂, if H₂O is formed, by adding the reaction free energy for the formation of H₂O. As an example Figure 4.4b, shows the interface formation of the non-stoichiometric interface formed between Pt(111) and α -SiO₂(0001), where, compared to the bulk stoichiometry of α -SiO₂, the interface is oxidized. This interface can be derived from the fully hydroxylated surface of α -SiO₂(0001) from which hydrogen needs to be removed, for example as H₂. In the presence of O₂, hydrogen may also be removed via the formation of H₂O where an adhesion energy $\gamma_{\text{adh}}^{\text{hydrox}} = -42$ meV/Å² at $T = 0$ K is obtained.

Table 4.7: Surface energy difference between hydroxylated and oxidized surface, if H₂ is liberated. $\Delta\gamma_{\text{ox-lat}}^{\text{ox}}$ is listed in meV/Å². Additionally, the number of hydroxyl groups per unit cell is listed, see Table 4.4 for the surface area of these unit cells.

Oxide	$\Delta\gamma_{\text{ox-lat}}^{\text{ox}}$	n/UC
O- α -SiO ₂ (0001)	272.03	2
O- α -Al ₂ O ₃ (0001)	414.39	3
2O- γ -Al ₂ O ₃ (110)	142.76	4
3O- γ -Al ₂ O ₃ (110)	222.33	6

The values of all calculated adhesion energies are presented in detail in Table 9.8 and the corresponding total energies used to calculate them in Table 9.11. The adhesion energies are plotted in Figure 4.6, 4.7 and 9.3 and discussed in section 4.3.

The obtained adhesion energies are compared in detail with previously reported values in Table 4.8. The agreement with a computed value²⁰⁴ for Ag(111) on O- α -Al₂O₃(0001) is very good with deviations of less than 10 meV/Å². Experimental²¹ and computed¹⁹⁵ values for the interface of Au/TiO₂(110) are around -40 meV/Å², while in this work roughly -60 meV/Å² is found. This can be attributed to the approximate calculation of the van der Waals interactions which dominate adhesion in this case, as shown in Figure 4.3.

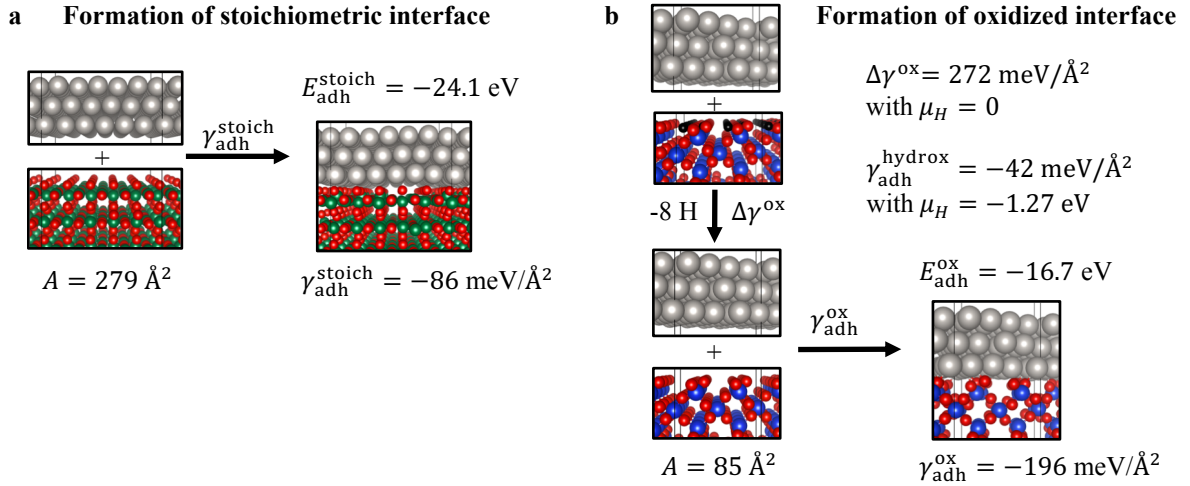


Figure 4.4: Approach to compute adhesion energies. (a) Formation of the interface between Pt(111) and the stoichiometric 110-surface of rutile in a $(7 \times 3\sqrt{3})/(3 \times 5)$ supercell. The adhesion energy is given per supercell (E) and per area (γ). (b) Formation of the oxidized interface between Pt(111) and α -SiO₂(0001) in a $(\sqrt{13} \times \sqrt{13})/(2 \times 2)R14^\circ$ supercell. Eight hydrogen atoms from eight hydroxyl groups are removed per supercell in the formation of the interface. The formation of the oxidized surface is added as an intermediate step. The chemical potential of hydrogen, μ_{H} is given relative to $1/2\text{H}_2$ at $T = 0 \text{ K}$. At 0 K, we consider H_2 as a reference ($\mu_{\text{H}} = 0$) and $\text{O}_2 + \text{H}_2\text{O}$ ($\mu_{\text{H}} = -1.28 \text{ eV}$).

Table 4.8: Comparison of adhesion energies from the literature for systems studied in this work with the values obtained in this work.

Metal	Oxide	γ_{adh} (meV/Å ²)	Reference
Au	TiO ₂ (110)	-34 to -44	ref. 21
		-26 to -35	ref. 195
Au(111)	TiO ₂ (110)	-61 to -62	this work, Table 9.8
Au(100)	TiO ₂ (110)	-68 to -70	this work, Table 9.8
Ag(111)	O- α -Al ₂ O ₃ (0001)	-253	ref. 204
		-252 to -258	this work, Table 9.8

4.3 Effect of adhesion on nanoparticle stability

The effect of adhesion on nanoparticles is illustrated in Figure 4.5 for Pt clusters, employing adhesion energies computed in this work for the interfaces between Pt(111) and the (110)-surface of rutile and the (0001)-surface of α -SiO₂. Figure 4.5a shows how the chemical potential of platinum μ_{Pt} varies as a function of particle size. It can be seen that the stabilization due to adhesion leads to a less steep variation of μ_{Pt} with size, thus reducing the driving force for sintering and stabilizing the particles. To calculate the chemical potential μ_{Pt} the formula derived by Campbell and coworkers²¹:

$$\mu_{\text{Pt}} = \mu_{\text{bulk}} + (3\gamma_{\text{Pt}} - \gamma_{\text{adh}}) \times \frac{V_{\text{m}}}{r}, \quad (4.5)$$

is employed, with $\mu_{\text{bulk}}^{\text{exp}} = -5.82 \text{ eV}$, the experimental Pt bulk chemical potential¹⁷⁹, $\gamma_{\text{Pt}}^{\text{exp}} = 138 \text{ meV}/\text{\AA}^2$, the surface energy of the Pt(111) surface and a volume per atom of $V_{\text{m}} = 15.1 \text{ \AA}^3$ as obtained with PBE-D3^{15,210}, r the nanoparticle radius and γ_{adh} the adhesion energy. Instead of the experimental values for μ_{bulk} and γ_{Pt} also the values obtained with DFT can be employed. Using $\mu_{\text{bulk}}^{\text{DFT}} = -6.26 \text{ eV}$ from Table 3.1 and $\mu_{\text{surface}}^{\text{cuboctahedral}} = 5.57 \text{ eV}$

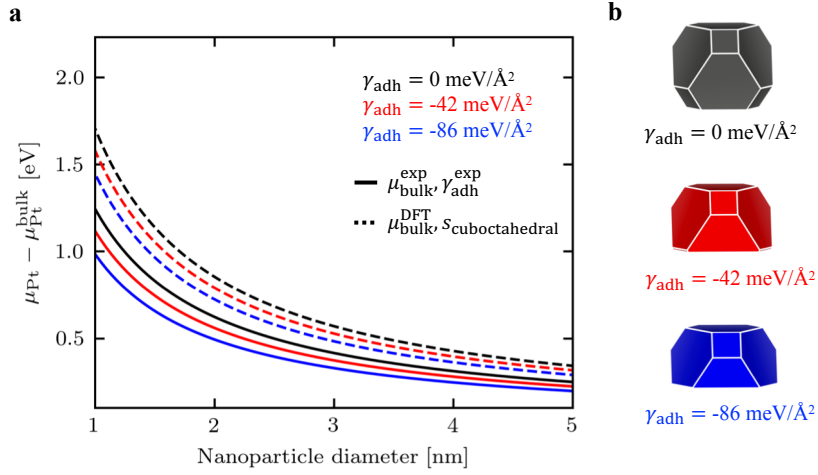


Figure 4.5: Effect of adhesion on the properties of nanoparticles. (a) Size-dependent chemical potential of platinum for different adhesion energies employing the formula derived by Campbell and coworkers²¹ and $\gamma_{\text{Pt}} = 138 \text{ meV}/\text{\AA}^2$ ²¹⁰ for the solid lines and $s_{\text{cuboctahedral}} = 5.57 \text{ eV}$ (section 3.3) for the dashed lines. (b) Wulff constructions of supported Pt clusters with $\gamma_{\text{Pt}}^{111} = 138 \text{ meV}/\text{\AA}^2$, $\gamma_{\text{Pt}}^{111}/\gamma_{\text{Pt}}^{100} = 0.73$ and a volume per atom of 15.1 \AA^3 as obtained with PBE-D3.^{15,179}

from section 3.3 to describe the stability of Pt nanoparticles results in the dashed line of Figure 4.5a. Figure 4.5b shows cluster shapes derived from a Wulff-construction employing the same adhesion energies. Adhesion changes the ratio of facets and edges and also affects the perimeter of the particle that is exposed to the gas-particle-support interface.

Figure 4.6a shows the adhesion energies of interfaces formed between O- α -SiO₂(0001), O- α -Al₂O₃(0001) and TiO₂(110) and the fcc(111)- and fcc(100)-surfaces of various transition metals: Ru, Os, Rh, Ir, Ni, Pd, Pt, Cu, Ag and Au, although it is noted that Ru and Os crystallize in the hcp-structure. Examples of the side-on view of the interfaces between Pt and the mentioned oxides are shown in Fig. 4.6c. Typically, the strain on the oxide is largest for supercells with Ni and Cu, which have the smallest lattice constants. The mean adhesion energies of different supercells are shown, using error bars to indicate the maximum deviation between these supercells, which is relatively small for α -SiO₂(0001), despite the differences in orientation and lattice mismatch. The adhesion energies are plotted against the adsorption energy of oxygen, $E_{\text{ad}}(\text{O})$, on the respective clean fcc(111) metal surfaces. Excellent correlation is observed and $E_{\text{ad}}(\text{O})$ can therefore be used as descriptor:

$$\gamma_{\text{adh}} \approx E_{\text{ad}}(\text{O}) \cdot a_{\text{ox}} + b_{\text{ox}} \quad (4.6)$$

as in scaling relations that have first been established for molecular adsorption on transition metal surfaces and extended to other systems, including metal-supported thin oxide films.^{42,211–214} Here, a_{ox} and b_{ox} are the scaling parameters which depend on the oxide. The parameter a_{ox} thus describes how a change in oxygen adsorption energy, when changing the metal, will affect the adhesion energy.

For α -Al₂O₃(0001) adhesion energies and the slope with respect to $E_{\text{ad}}(\text{O})$ are larger than for α -SiO₂(0001), which is mainly due to the higher concentrations of hydroxyl groups on the hydroxylated surface, that ultimately leads to a higher concentration of metal-oxygen bonds at the interface. For TiO₂(110) the interfaces with both fcc(111) and fcc(100) surfaces are studied. This allows the direct comparison of the adhesion energies of different metal facets. The adhesion per metal atom is typically stronger for fcc(100), however, this is partially compensated by the surface area per metal atom that is 12% higher for fcc(100). As a result, fcc(111) and fcc(100) surfaces are expected to have comparable adhesion energies per area on oxides when they form an incommensurate over layer.

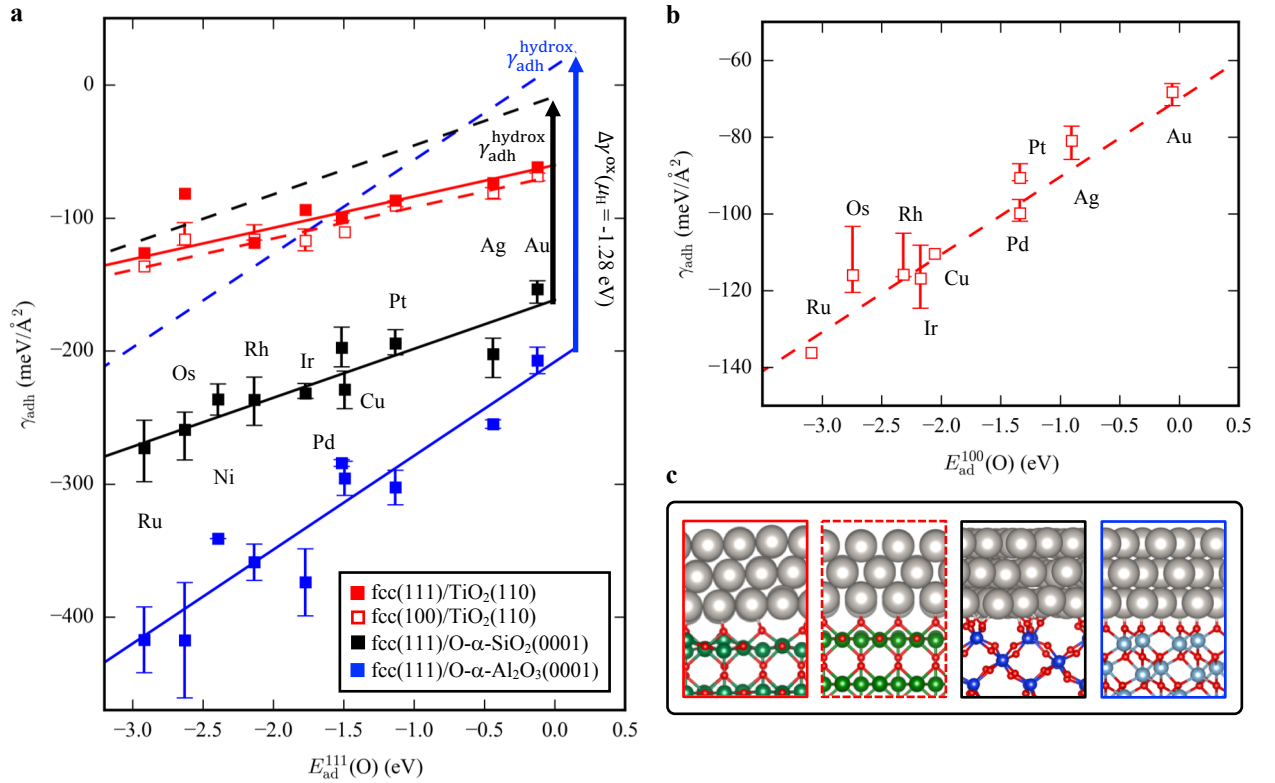


Figure 4.6: Trends in adhesion energies for metal-oxide interfaces. (a) Adhesion energies are shown as a function of oxygen adsorption energies on clean fcc(111) metal surfaces. The adhesion energies were averaged over all computed supercells (see Table 4.1) and the largest and smallest deviation within these individual calculations is indicated with error bars. For O- α -SiO₂(0001) and O- α -Al₂O₃(0001), the adhesion energies are given relative to the oxidized surfaces. In addition, given as dashed lines are the adhesion energies obtained with a hydroxylated oxide surface as the reference. Here, the adhesion free energy depends on the chemical potential of hydrogen and $\mu_H = -1.28$ eV is used as reference. The shift between oxidized and hydroxylated reference is indicated as $\Delta\gamma^{ox}$. (b) Adhesion energies of the fcc(100) metal surfaces with TiO₂(110) as a function of oxygen adsorption energies on clean fcc(100) metal surfaces. (c) Side-on views of the interfaces of Pt with the oxide surfaces listed above. From left to right: Pt(111)/TiO₂(110), Pt(100)/TiO₂(110), Pt(111)/O- α -SiO₂ and Pt(111)/O- α -Al₂O₃(0001).

For the sake of simplicity, $E_{ad}^{111}(O)$ obtained for fcc(111)-surfaces is used as a descriptor also for adhesion energies of the fcc(100) facets, as no fundamentally different results are obtained with $E_{ad}^{100}(O)$, see Figure 4.6b and 9.3. Additionally, interfaces formed with the stoichiometric (10 $\bar{1}0$)- and (11 $\bar{2}0$)-surface of ZnO in wurtzite-structure and the (101)-surface of ZrO₂ in tetragonal structure are studied. The adhesion energies are in the same range (-160 to -70 meV/Å²) as those for TiO₂(110) and are also well described by scaling relations (see Figure 4.7b, c). The interfaces with oxidized γ -Al₂O₃(110) surfaces were also studied and lead to adhesion energies on the order of -200 meV/Å² and are therefore somewhat weaker than those of α -SiO₂(0001), see Figure 4.7a. As expected, the more oxidized surface, 3O- γ -Al₂O₃(110), leads to stronger adhesion than 2O- γ -Al₂O₃(110).

4.4 Model to predict adhesion energies

So far, it was studied how adhesion energies of metal-oxide interfaces vary with the metal for a given support. Finding suitable descriptors for the comparison of the reactivity of different oxide surfaces is more challenging. Surface energies of oxides and oxygen vacancy formation energies have been used to describe the reactivity of

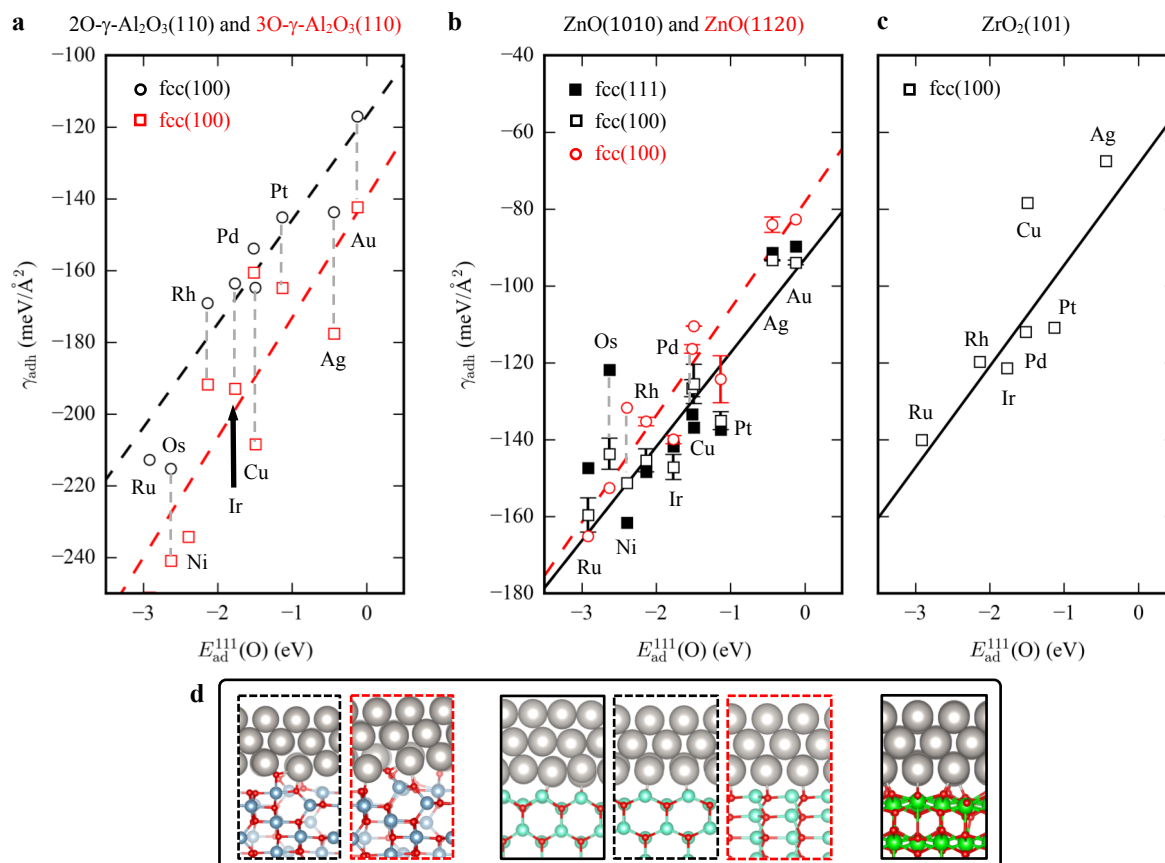


Figure 4.7: Additional adhesion energy calculations. (a) Adhesion energies between fcc(100)-surfaces and the oxidized $\gamma\text{-Al}_2\text{O}_3(110)$ surfaces derived from hydroxylated surfaces with two and three adsorbed water molecules per unit cell. (b) Adhesion energies for the $(10\bar{1}0)$ - and $(11\bar{2}0)$ -surfaces of ZnO in wurtzite structure. Os is excluded from the fit in the case of $\text{ZnO}(10\bar{1}0)$. (c) Adhesion energies for the (101) -surface of tetragonal ZrO_2 . (d) Side-on views of the interfaces of Pt with the oxide surfaces listed above. From left to right: $\text{Pt}(100)/2\text{O}-\gamma\text{-Al}_2\text{O}_3(110)$, $\text{Pt}(100)/3\text{O}-\gamma\text{-Al}_2\text{O}_3(110)$, $\text{Pt}(111)/\text{ZnO}(10\bar{1}0)$, $\text{Pt}(100)/\text{ZnO}(10\bar{1}0)$, $\text{Pt}(100)/\text{ZnO}(11\bar{2}0)$, $\text{Pt}(100)/\text{ZrO}_2(101)$.

oxides before.^{92,199,215} For the cases studied here, the best tested descriptor is the concentration of bonding oxygen atoms at the metal-support interface, c_{O} . No clear-cut definition for metal-oxide bonds at the interface can be derived since the chemical bond itself is a concept rather than a directly measurable quantity. A distance-based criterion is used to determine bonds, since this is based on a well-defined observable. Clearly, all surface oxygens at the interfaces with $\text{O}-\alpha\text{-Al}_2\text{O}_3(0001)$ and $\text{O}-\alpha\text{-SiO}_2(0001)$ engage in chemical bonding. The corresponding bonds-lengths can therefore be used to determine distance-based criteria for c_{O} . Generally, the shortest metal-oxygen distance for a given oxygen is considered. For $\text{O}-\alpha\text{-Al}_2\text{O}_3(0001)$, the metal-oxygen bond lengths vary in between 2.07 \AA and 2.30 \AA for Ag and in between 1.95 \AA and 2.12 \AA for Rh. A tolerance of 0.3 \AA is added to the largest bond lengths to arrive at metal-specific bonding criteria that are around 2.4 to 2.6 \AA . The mentioned bond lengths and criteria are listed in Table 9.9 and the obtained values for the number of interfacial oxygen atoms N_{O} in Table 9.10. The resulting scaling parameters and c_{O} are all listed in Table 4.9. For the interfaces formed from the hydroxylated $\alpha\text{-Al}_2\text{O}_3(0001)$ and $\alpha\text{-SiO}_2(0001)$ surfaces, c_{O} simply equals the concentration of the hydroxyl groups of clean, hydroxylated surfaces. For $\text{TiO}_2(110)$, $\text{ZnO}(11\bar{2}0)$ and $\text{ZnO}(10\bar{1}0)$, c_{O} can be deduced from the number of surface oxygen atoms on the clean oxide surfaces. For the surfaces of $\gamma\text{-Al}_2\text{O}_3(110)$ and $\text{ZrO}_2(101)$, c_{O} cannot easily be predicted from their hydroxylated and clean surfaces. One therefore needs to perform at least a

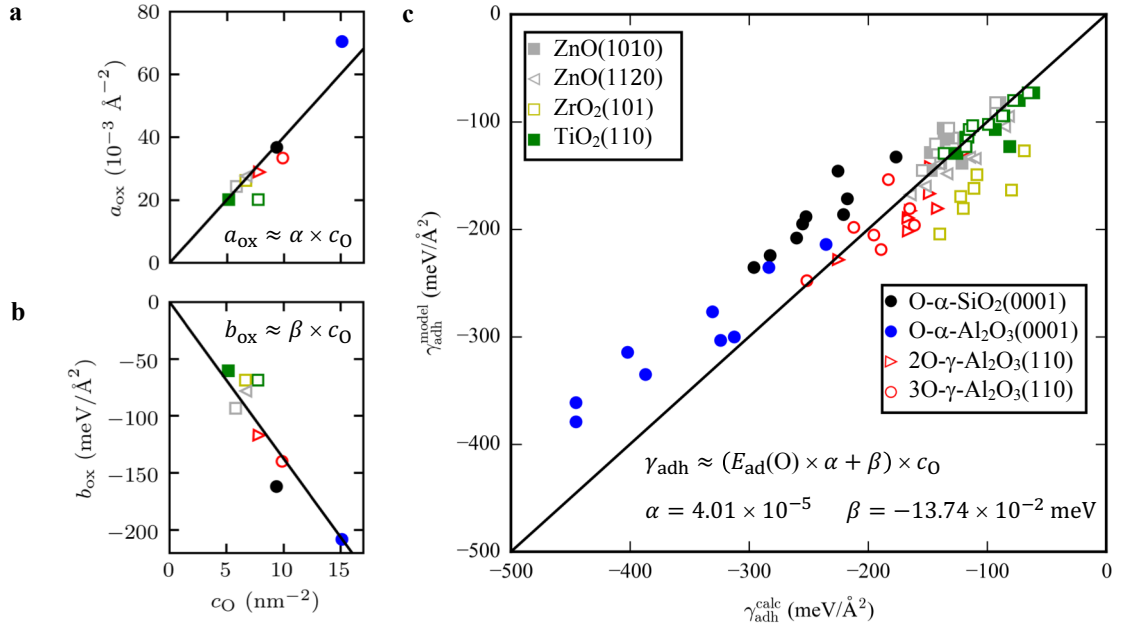


Figure 4.8: Variation of adhesion energies with the type of oxide surface. (a) The slope a_{ox} obtained by fitting adhesion energies for a given oxide as a function of oxygen adsorption energies is shown for different oxides as a function of the number of interfacial oxygen atoms, c_{O} . (b) Same as (a) for the offset b_{ox} . (c) Parity plot where the two fitted parameters α and β are used to predict adhesion energies using eq. (4.7) and are compared to all values computed in this work.

single interface calculation to deduce the number of bonds from the atomic structure based on the distance criteria noted above.

Table 4.9: Obtained scaling parameters a_{ox} and b_{ox} and the mean absolute error (MAE) from Fig. 4.6 and Fig. 4.7 and concentration of interfacial oxygen atoms c_{O} , plotted in Fig. 4.8a, b. If c_{O} cannot be determined from the number of surface oxygens, the mean number of M-O bonds for all calculated metal/oxide interfaces is used. A bond counts as an M-O bound if the M-O distance is smaller than the criterion given in Table 9.9.

Oxide surface	Metal surface	Metal supercell	a_{ox} (10^{-3} \AA^{-2})	b_{ox} ($\text{meV}/\text{\AA}^2$)	MAE ($\text{meV}/\text{\AA}^2$)	c_{O} (nm^{-2})
O- α -SiO ₂ (0001)	fcc(111)	($\sqrt{13} \times \sqrt{13}$)R14°	36.75	-161.72	10.41	9.38
O- α -Al ₂ O ₃ (0001)	fcc(111)	($\sqrt{13} \times \sqrt{13}$)R14°	70.54	-208.26	19.23	15.12
2O- γ -Al ₂ O ₃ (110)	fcc(100)	3 × 3	28.95	-116.94	7.48	7.82
3O- γ -Al ₂ O ₃ (110)	fcc(100)	3 × 3	33.46	-139.65	15.55	9.87
TiO ₂ (110)	fcc(100)	7 × 1	23.54	-68.33	3.91	7.71
	fcc(111)	7 × 3	23.54	-60.30	3.91	5.14
ZnO(10 $\bar{1}$ 0)	fcc(100)	5 × 2	24.45	-92.96	6.27	5.78
	fcc(111)	2 × 2	24.45	-92.93	8.92	5.78
ZnO(11 $\bar{2}$ 0)	fcc(100)	2 × 2	27.76	-78.18	7.03	6.68
ZrO ₂ (101)	fcc(100)	3 × 3	26.30	-68.32	7.52	6.64

Using the concentration of interfacial oxygen atoms, c_{O} , the scaling parameters (slope a_{ox} and offset b_{ox}) obtained for the different oxides can be analyzed. Figure 4.8a and b show slope and offset, respectively, as a function of

c_O . If adhesion is dominated by binding through interfacial oxygen atoms, it is expected that in the absence of interfacial oxygen ($c_O = 0$), both a_{ox} and b_{ox} are zero. In fact, a_{ox} and b_{ox} are approximately proportional to c_O and can thus be relatively well described with two parameters ($a_{ox} = \alpha \times c_O$ and $b_{ox} = \beta \times c_O$). The interface energies of all interfaces can now be approximated using the simple formula:

$$\gamma_{adh} \approx (E_{ad}(O) \cdot \alpha + \beta) \cdot c_O. \quad (4.7)$$

Figure 4.8c shows a parity plot, where the adhesion energies predicted using eq. (4.7) are compared with those computed explicitly with DFT. The correlation is generally good, with some systematic deviations caused by the underestimation of the slope of O- α -Al₂O₃(0001) and the errors in the offset of both α -SiO₂(0001) and ZrO₂(101).

4.5 Conclusions

A variety of metal-oxide interfaces were systematically studied using different supercells to minimize lattice mismatch. Scaling relations can be used to analyze adhesion energies, where the adsorption energy of atomic oxygen on clean metal surfaces $E_{ad}(O)$ serves as a descriptor. Variations between different oxides can be described by the different concentration of interfacial oxygen atoms, c_O . This concentration can in many cases be easily extracted from the atomic structure of the clean oxide surfaces. A simple model is proposed that allows the prediction of adhesion energies for a given metal-oxide based on these two descriptors ($E_{ad}(O)$, c_O). Consequently, properties that depend on the adhesion energy, such as particle shape or metal chemical potential are also accessible through this model.

5 Combined simulation of Ostwald ripening and particle migration

5.1 Introduction

A kinetic Monte Carlo (kMC) based model that can be used to simulate migration of different sized Pt nanoparticles on supports with point defects is used to study the effects of temperature, particle-size, particle-concentration, defect-concentration and defect-binding strength on sintering. Additionally, simulations are performed that combine particle migration and coalescence (PM) with Ostwald ripening (OR), where the latter is simulated through a mean-field model. This allows to assess the relative importance of PM and OR as well as their interaction.

5.2 Particle migration

In principle, there are two ways in which particles can migrate on the support: Concerted movement (translation) and non-concerted movement.²¹⁶ The model described here focuses on the non-concerted movement of particles, which arises from multiple (typically more than 10^6) single-atom movements. Diffusion constants are taken from ref. 49, where they have been determined for Pt particles of different sizes and different temperatures using adhesion energies for Pt(111) on α -Quartz(001). Based on that data⁴⁹, the following parameterization to describe all activation energies required during the simulation is employed:

$$E_a/\text{eV} = c_1 + c_2 \cdot N_{\text{Pt}}^{c_3} \quad (5.1)$$

with N_{Pt} being the number of platinum atoms of the migrating nanoparticle and $c_1 = 9.07$, $c_2 = -9.15$ and $c_3 = -0.05$ being constants. In ref. 49, diffusion constants were determined only for crystalline particles larger than 300 atoms, since it is unlikely that the fcc-parameterization will hold for smaller particles, the formula is expected to be valid only for sufficiently large particles. Therefore, a lower limit to the activation energy $E_{a,\text{min}} = 2 \text{ eV}$ is introduced to prevent unrealistic activation barriers in the region for which the formula has not been parameterized.

The diffusion constant can be expressed in terms of a lattice-hop model:

$$D = l^2 \times \frac{k_{\text{B}}T}{h} \times \exp\left(-\frac{G_a}{k_{\text{B}}T}\right), \quad (5.2)$$

where D is the diffusion constant, $l = 289 \text{ pm}$ is the experimental lattice parameter of Pt(111)¹⁷⁹, T is the temperature, k_{B} is the Boltzmann constant, h is Planck's constant and G_a is the activation free energy. It turns out that the free energy of activation varies very little with temperature, so throughout E_a will be used instead of G_a . What makes the lattice-hop model in eq. (5.2) convenient is the fact that it expresses the strongly temperature-dependent diffusion constant through a single temperature-independent activation energy (eq. (5.1)). The only remaining variable is the nanoparticle size and the interpolated activation energy, which is shown as a function of particle size in Fig. 5.1a. It can be seen that the activation energy for diffusion is increasing the particle size.

This chapter is based on the following publication: Dietze, E. M.; Abild-Pedersen, F.; Plessow, P. N., Comparison of Sintering by Particle Migration and Ripening through First-Principles-Based Simulations. J. Phys. Chem. C 2018, 122, 46, 26563-26569.

PM is simulated with a 2D-lattice Bortz–Kalos–Lebowitz (BKL)-kMC algorithm^{156,217,218} on the hexagonal lattice derived from the Pt(111)-surface employing periodic boundary conditions. Size- and temperature-dependent diffusion constants are computed using eq. (5.2) and activation energies using eq. (5.1), shown in Fig. 5.1a. The particles are represented as hemispheres and coalescence occurs immediately when two particles collide. Fast coalescence is supported by the 3D-lattice kMC simulations described in ref. 216, where coalescence is orders of magnitude faster than diffusion.

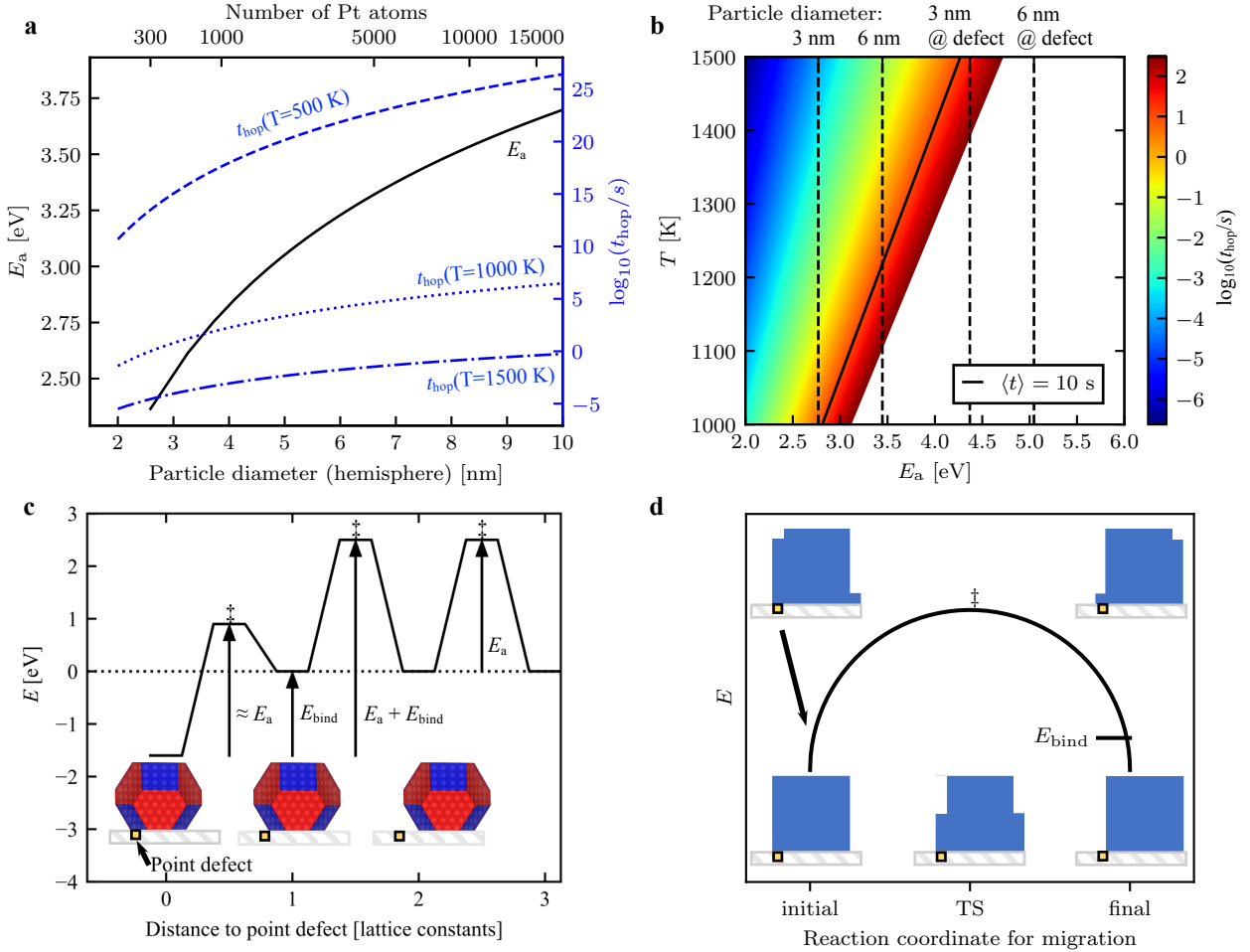


Figure 5.1: (a) Activation energy E_a for migration as a function of particle size (left y-axis) and the corresponding average time for a lattice hop $\log_{10}(t_{\text{hop}}/s)$ (right y-axis). (b) Average time for lattice-hop as a function of activation barrier: $\log_{10}(\langle t = 1/k \rangle/s)$. The color-map extends only to one hour. Activation barriers for particles with a diameter of 3 and 5 nm bound and not bound to a defect with $E_{\text{bind}} = 1.6$ eV are highlighted. (c) Illustration of the energetics for the migration processes in the presence of defects with an activation barrier of $E_a = 2.5$ eV and a binding energy to the defect of $E_{\text{bind}} = 1.6$ eV. (d) Illustration of the pillbox model. A cubic particle moves by one lattice constant by transferring a layer of atoms from left to right. In the transition state the facets on left and right side are equal. The energy is schematically shown. In case of the presence of a defect, the reaction path is expected to deviate near the final state, leading to a less stable particle.

In the absence of defects, a particle with a size-specific activation energy for migration E_a (> 2.0 eV) migrates between degenerate minima on the support. In Fig. 5.1b, the average time for one lattice-hop is shown as a function of the activation energy. A higher E_a leads to an increase in time required for a lattice-hop. This is also demonstrated for 3 different sample temperatures with the blue lines in Fig. 5.1a. In general, the migration of a particle, which is in initial and final state in its minimum shape, requires an entire facet to be transferred from

left to right (e.g. in the direction in which the particle moves), as is schematically shown in Fig. 5.1d. The least stable state, the transition state, occurs when half of the facet is transferred, because the two half-facets have the maximum edge lengths within this process and have therefore the largest number of under-coordinated atoms. This is of course only a qualitative picture, whereas the real particle may also furthermore change its shape to minimize the energetic cost of the transformation. Nevertheless, the simple model by Harris²¹⁹, captures the underlying physics of the process. Importantly, due to the adhesion energy, it is likely that the remaining half-facets are, in the transition state, still in contact with the support. Within the simple pillbox model, these atoms would even be the last to migrate to the other side of the particle.

In the presence of defects, a behavior as illustrated in Fig. 5.1c is expected. When bound to a defect, the particle is stabilized by E_{bind} , which lowers the energy of the corresponding minima. In the picture of the pillbox model, this means that the particle is still in contact with the defect during the transition state and that the last atoms will detach from the defect only after the transition state. Consequently, the binding to the defect is not expected to influence the barrier away from the lattice site significantly. Thus, PM is not influenced by the defect when it is two lattice sites away and the particle can then be considered ‘fully dissociated’. The effective barrier for dissociation from the defect is at least $E_a + E_{\text{bind}}$, which is the height of the second migration step relative to the defect-bound position. The transition state for the initial dissociation is not known explicitly but can be expected to be in between E_a (full interaction of the transition state with the defect as in the minimum) and $E_a + E_{\text{bind}}$ (no interaction of the transition state with the defect).

Therefore, all rate-constants for diffusion that lead to dissociation from a defect are derived from $E_a + E_{\text{bind}}$ instead of the usual E_a . In ref. 27, it has been shown that Pt particles are expected to bind to dangling Si-O groups with a binding energy of $E_{\text{bind}} = 1.6$ eV. Generally E_{bind} is treated as an adjustable parameter to study its effect on sintering. The effect of $E_{\text{bind}} = 1.6$ eV on the lattice-hopping time is shown in Fig. 5.1b.

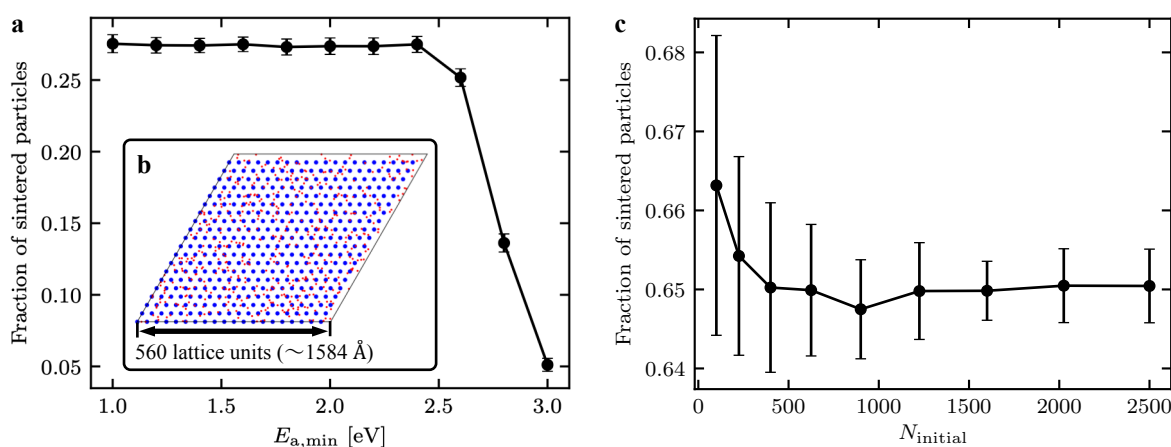


Figure 5.2: (a) Convergence of $E_{a,\text{min}}$ for PM initialized with 10 different normal distributions with $\langle d_{\text{init}} \rangle = 3.5$ nm, $\sigma = 1.0$ nm and $N_{\text{part}} = 2000$ at $T = 1000$ K for $t = 1$ h and (b) as inset. (b) Illustration of an unit cell of 400 3 nm Pt particles with an initial distance of 5 nm. 400 randomly distributed defects are shown as red dots. (c) Convergence of the fraction of sintered particles with the number of particles n_{part} initialized on a regular grid. ($t = 1$ h, initial distance = 20 nm, $T = 1000$ K, $d_{\text{init}} = 3$ nm).

As periodic boundary conditions are employed in all simulations, the size of the supercell is the main parameter that controls the convergence of the simulation results with respect to system size. When the number of particles per unit cell is small (obviously the case if only a single particle is present) the sintering simulations will not be meaningful. The system size (super cell size) is measured, for a given concentration of particles on the support, in terms of the number of particle per unit cell. For pure PM simulations, particle size distribution (PSD)s are used

where all particles have an initial diameter of $d_{\text{initial}} \geq 2$ nm and due to the mechanism the particles can only grow in size, so that variations of the value of the lower limit $E_{a,\text{min}} = 2$ eV have no effect. In the case of simulations that combine PM and OR, initial PSDs also include particles with $d_{\text{initial}} < 2$ nm and small particles are also created through OR. In Fig. 5.2a, the PM simulation is initialized with a normal PSD that includes also particles smaller than 2 nm, as shown in Fig. 5.6a in grey. It can be seen that the simulation result, measured in fraction of sintered particles, is not influenced as long $E_{a,\text{min}} < 2.5$ eV. The convergence of the kMC simulations with respect to the size of the unit cell is shown in Fig. 5.2c. It is found that an ensemble of 400 particles per unit cell is sufficient to reach an accuracy of 5% in terms of sintered particles and 2000 particles per unit cell for an accuracy of less than 1%. For PM all ensembles are initialized on a regular grid, as depicted in Fig. 5.2b. The particle distance refers to the smallest distance between the outer spheres of the nanoparticles.

The results from sintering simulations are compared after an elapsed time of one hour, which is a realistic time-frame also for lab-scale experiments. The extent of sintering is quantified through the fraction of sintered particles given by $1 - \frac{N_t}{N_0}$, where N_0 is the initial number of particles and N_t the number of particles after an elapsed time t . This definition of sintering is very well defined computationally, such that 0 means no sintering and close to 1 means full sintering. Experimentally, the extent of sintering is often measured through the evolution of the PSD, in particular the average diameter. These measures are usually correlated as shown in the Figure 5.6d and one can therefore always transform between these representations thus enabling a direct comparison to experiments.

5.2.1 Particles on defect-free support

First it will be studied how sintering depends on the initial particle distance and the initial particle diameter d_{initial} . Fig. 5.3a shows how the fraction of sintered particles after 1 h decreases roughly linearly with inter-particle distance and that the rate of decrease increases with particle size. This is the result of a complex relation between activation energy vs. size and mean particle displacement from its initial position. At larger inter-particle distances, sintering within 1 h is suppressed for the larger particles and hence the fraction of sintered particles remains constant at essentially zero. Thus at $T = 1000$ K particles larger than $d_{\text{initial}} = 5$ nm are stable to sintering within one hour.

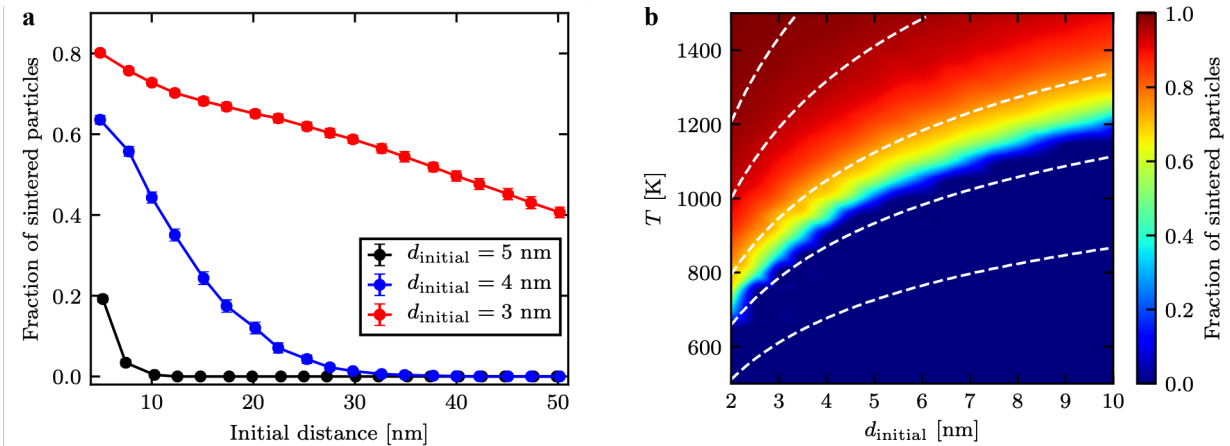


Figure 5.3: (a) Fraction of sintered particles after one hour of sintering as a function of the initial distance with $d_{\text{initial}} = 3, 4$ and 5 nm at $T=1000$ K. (b) Temperature and size dependence of sintering at a fixed inter particle distance of 5 nm. White dashed lines illustrate constant diffusion coefficients at different sizes and temperatures.

Fig. 5.3b shows the extent of sintering as a function of temperature and particle size for an initial distance of 5 nm. As one would expect, for a given particle diameter the fraction of sintered particles increases with increasing temperature and decreases with increasing particle size. The white lines in Fig. 5.3b illustrate a constant diffusion

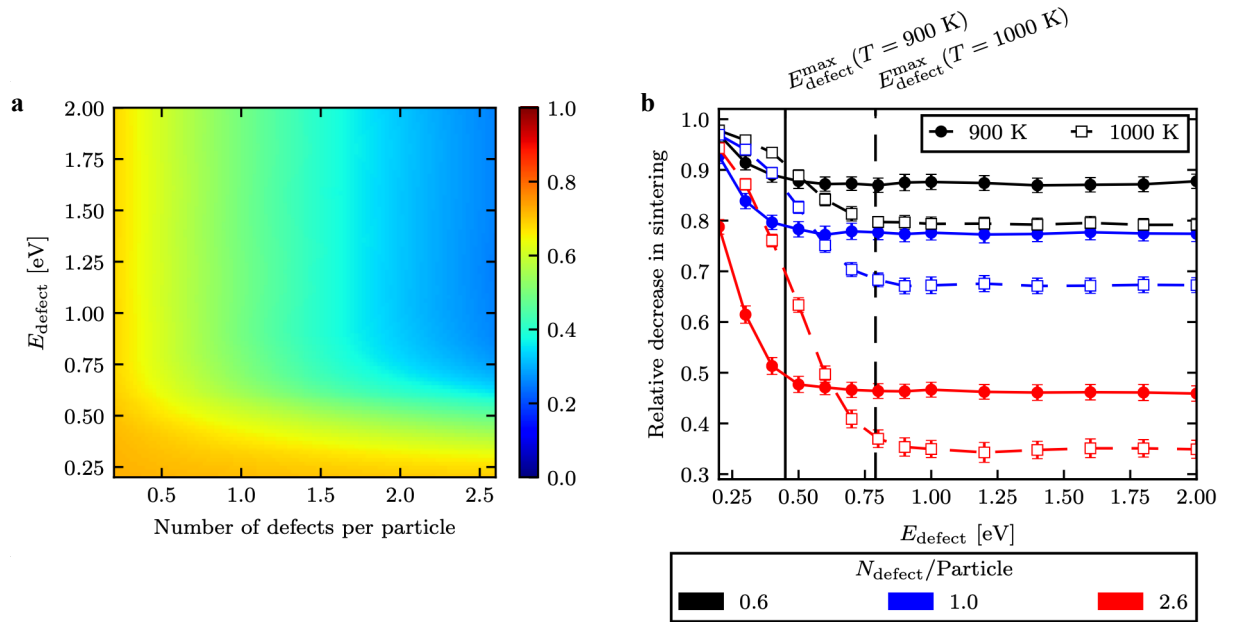


Figure 5.4: (a) Fraction of sintered particles depending on the defect energy and number of defects per particle for $T = 1000$ K, initial particle size $d_{\text{initial}} = 3$ nm and initial distance of 10 nm. (b) Relative decrease in sintering as a function of E_{defect} for different number of defects per particle. The initial particle size is $d_{\text{initial}} = 3$ nm with an initial distance of 10 nm. The relative decrease in sintering is defined as the fraction of sintered particles on the support with defects divided by the fraction of sintering on the defect free surface.

coefficient for different temperatures and particle diameters. It can be seen that constant sintering is well-described by constant diffusion coefficients.

5.2.2 Effect of defects

Defects are initialized in random positions on the kMC-lattice (Fig. 5.2b, red circles) with an adjustable number of defects N_{defect} per particle. The defect binding energy, E_{defect} , is variable to investigate how it affects the fraction of sintered particles. The relative decrease in sintering with increasing number of defects per particle for constant E_{defect} is shown in Fig. 5.4a. Here, a relative decrease in sintering < 1 means that the fraction of sintered particles has decreased by the given amount. In Fig. 5.4b two different temperatures ($T = 900$ and 1000 K) and three different defect concentrations are studied. Generally, sintering decreases rapidly with increasing E_{defect} until it levels off and remains constant after a certain value of E_{defect} . This characteristic value, $E_{\text{defect}}^{\text{max}}$, is found to be independent of defect concentration but depends sensitively on the temperature. As shown in Fig. 5.4b with vertical bars, $E_{\text{defect}}^{\text{max}}$ can be estimated accurately by using the average time to escape t_{esc} from the defect, which is the inverse of the rates constant computed through eq. (5.2):

$$E_{\text{defect}} = -k_{\text{B}}T \ln \left(\frac{\sqrt{2}h}{t_{\text{esc}}k_{\text{B}}T} \right) - E_a. \quad (5.3)$$

Here, the factor $\sqrt{2}$ is due to the use of a hexagonal lattice. As expected, more defects and, up to a certain value $E_{\text{defect}}^{\text{max}}$, stronger binding suppress sintering. The simulations thus show that the defect binding energy $E_{\text{defect}}^{\text{max}}$ required to trap a particle with a given diffusion constant for a given time Δt can be estimated using the rate-constant derived from the lattice-hop model. The defect binding energy $E_{\text{defect}} = 1.6$ eV given in ref. 32 is therefore more than sufficient to trap the particles under the conditions studied here.

5.3 Combined simulation

Gas phase mediated Ostwald ripening is modeled through the mean-field model described in ref. 27, which is based on the Wynblatt-Gjostein model²³ as described in detail in section 1.2.1. In short, PtO₂-emission from the particles is determined based on a sticking coefficient ($S = 1$) and a particle-size dependent chemical potential of Pt that is derived from a Wulff-construction with a surface energy fitted to reproduce experimental kinetics. No diffusion limitations and only redeposition of Pt in between existing particles is assumed. This determines a spatially constant (albeit time-dependent) background pressure of PtO₂.

5.3.1 Extension of the kMC algorithm for particle migration

The combined simulation of PM and OR is best understood as a modification of the kMC simulation that is used to model PM. Within the employed model, migration does not influence the ripening process unless coalescence occurs, which turns two particles into a single, larger particle. Ripening however, within the mean-field model, continuously changes the size of all particles and therefore their diffusion constants. Such a continuous change is of course impractical numerically and OR-steps are performed after certain discrete time-steps, Δt_{\max} , and after coalescence. Δt_{\max} is set to the time after which the first particle has experienced a change in particle size that exceeds two predefined thresholds. These thresholds are defined with respect to a change in the number of atoms (or volume) of the particle: A relative threshold (default 10%) and an absolute threshold (default 100 atoms). Fig. 5.5b shows that the fraction of sintered particles varies within the simulation error bars for an absolute threshold between 50 and 800 atoms, corresponding to a relative threshold of 5% to 80%. The numerical accuracy with which the two models are combined is thus defined by these two thresholds. PM-kMC steps (diffusion steps) are performed until coalescence occurs or Δt_{\max} is exceeded, after which an OR-step is performed. After each OR-step, particle-sizes and diffusion constants are updated. A flow chart of the described simulation steps is shown in Fig. 5.5a.

In principle, nanoparticles consist of an integer number of atoms. This property can be conserved in simulations of pure PM since any initial PSD that consists only of particles with an integer number of atoms will through particle migration and coalescence only result in other PSDs with integer-number particles.

On the contrary, mean-field models for ripening continuously transfer fractional numbers of Pt atoms in between nanoparticles and it is not clear how this can be avoided in a physically meaningful way. Since the interpolated activation energies can be readily used for particles with fractional numbers of Pt atoms, the clusters are treated with a continuous number of Pt atoms, since this allows the combination of OR and PM and conserves the total number of Pt atoms at all times.

For the combined PM and OR simulation, the simulations are initialized with randomly distributed particles with a PSD given by a normal distribution with an initial mean diameter $\langle d_{\text{initial}} \rangle = 3.5$ nm and standard deviation $\sigma = 1.0$ nm^{28,51,58,66}. The calculation contains at least 2000 particles to smoothly represent the normal distribution. Additionally, each simulation for a given first and second moment of the normal distribution is randomly initialized as described in ref. 27 to reduce artificial effects from the discretization of the ideally continuous normal distribution. Since the positions of particles of different sizes on a regular grid is ambitious, the particles are initialized with fully randomized positions, requiring only that they do not overlap. Each simulation was repeated five times and the fraction of sintered particles deviate by $\pm 1\%$, showing only insignificant fluctuations between simulations.

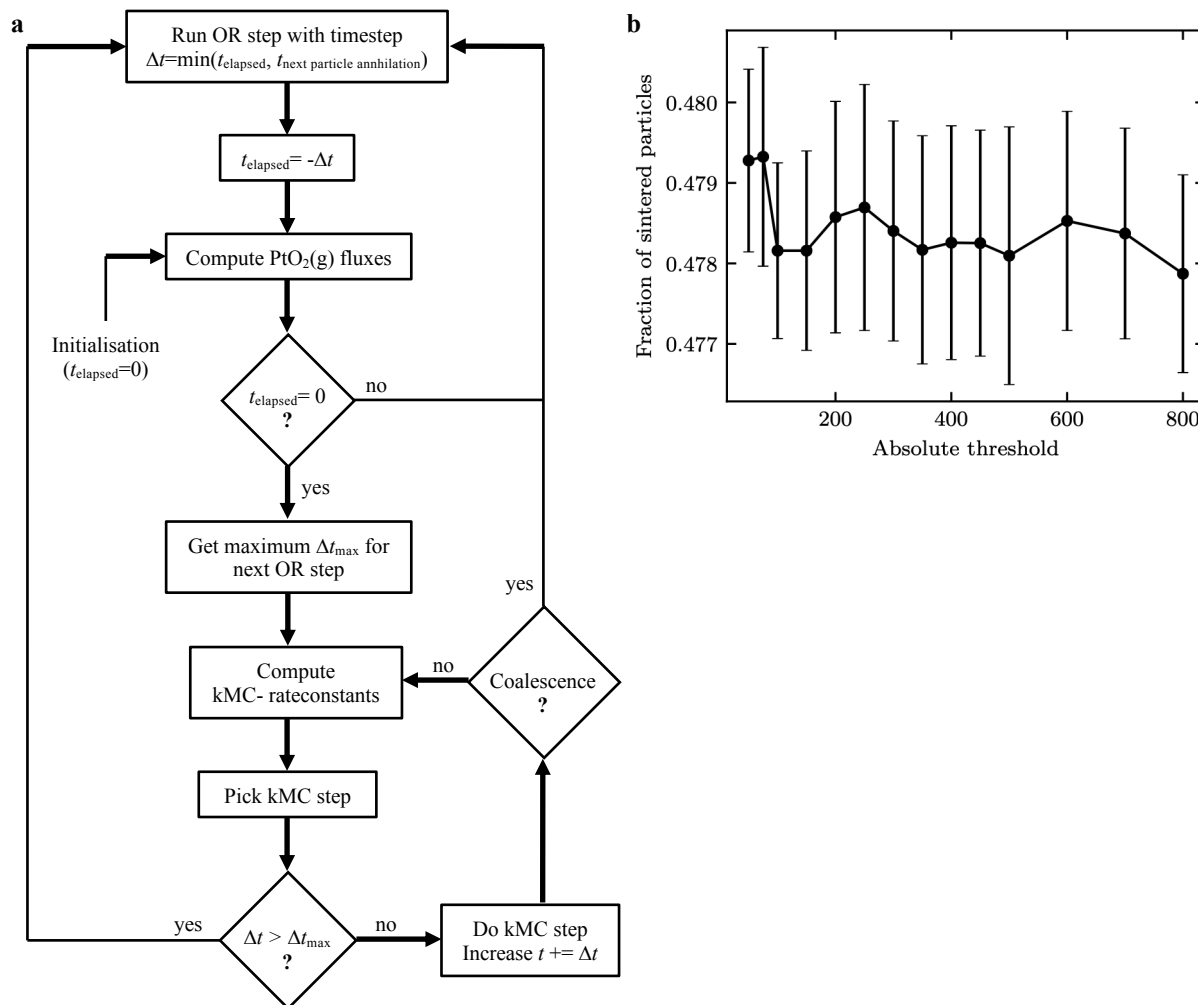


Figure 5.5: (a) Flow chart for the combined kMC-model of PM and the continuum model for OR. (b) Convergence of the fraction of sintered particles with the relative and absolute threshold. ($t = 1$ h, $T = 1100$ K, $p_{\text{O}_2} = 0.2$ mbar, number of employed particles: 2000, $\langle d_{\text{initial}} \rangle = 3.5$ nm and $\sigma = 1.0$ nm, Number of simulations: 96).

5.3.2 Results and Discussion

To study the relative importance of the different sintering mechanisms, simulations on PM and OR are performed separately as well as on PM and OR combined, (PM \circ OR). Fig. 5.6a shows the evolution of the initial PSD after 1 h simulation time at $T = 1200$ K and an oxygen background pressure $p_{\text{O}_2} = 0.1$ mbar for the three different scenarios, PM, OR, and PM \circ OR. All three sintering models visibly shift the PSD towards larger diameters, thus signifying sintering. As expected^{76,219}, the PSD resulting from PM shows no tail towards lower diameters whereas this is clearly the case for both OR and PM \circ OR, which also show broader PSDs. Beside these observations, no characteristic features can be extracted from the PSDs.

Figure 5.6b shows the dependence of the fraction of sintered particles on the width of the used PSD, σ , for different initial mean diameters $\langle d_{\text{init}} \rangle$. With increasing $\langle d_{\text{init}} \rangle$ the fraction of sintered particles reduces, as could be also seen in Fig. 5.3a. Increasing σ has only a minor effect for the pure PM. For OR the fraction of sintered particles increases with increasing σ and for $\langle d_{\text{init}} \rangle = 1.5$ nm it becomes identical with the results of PM \circ OR. The same would be expected for the larger $\langle d_{\text{init}} \rangle$, if σ would be increased further. For PM \circ OR the fraction of sintered particles is not strongly dependent on σ , but for $\sigma < 0.2$ nm and $\langle d_{\text{init}} \rangle = 2.5$ nm the sintering is larger than the

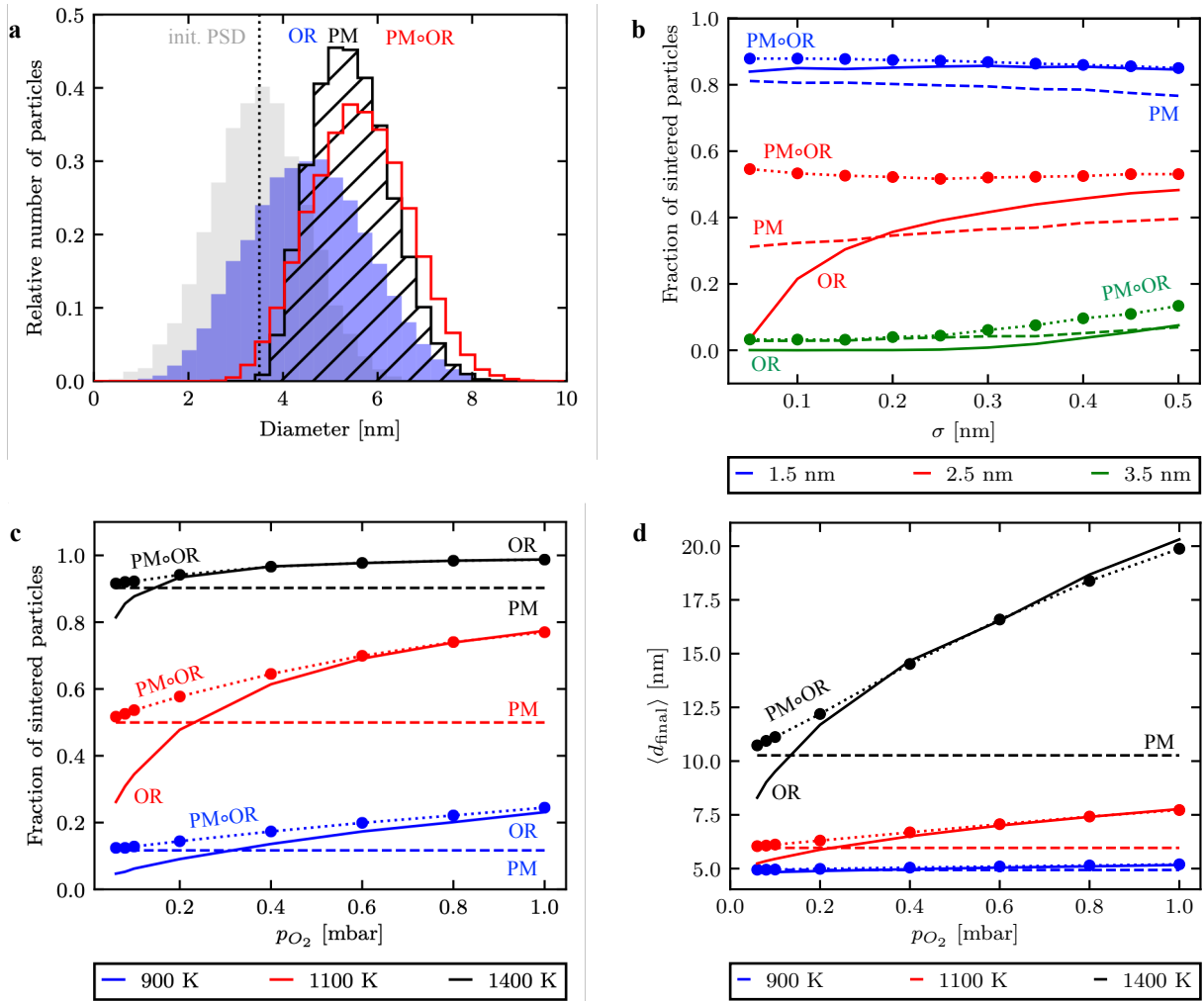


Figure 5.6: (a) Particle size distributions for PM (black), OR (blue) and PM \odot OR (red) at $T = 1200$ K and $p_{O_2} = 0.1$ mbar. The grey PSD shows the initial distribution. (b) Fraction of sintered particles for PM, OR and PM \odot OR for different PSD widths σ and initial mean diameter $\langle d_{init} \rangle$. The simulations employed 2000 particles, $T = 873$ K, $p_{O_2} = 0.3$ mbar and $t = 6$ h. (c) Fraction of sintered particles and (d) final mean diameter $\langle d_{final} \rangle$ for PM, OR and PM \odot OR for different oxygen pressures and temperatures. The simulations employed 2000 particles, $\langle d_{init} \rangle = 3.5$ nm and $\sigma = 1.0$ nm.

sum of PM and OR together. This can be explained as follows: PM of the still relatively mobile nanoparticles leads to an increase in the width of the PSD in the beginning of the simulation, which enhances OR in the combined simulation compared to the pure OR. For the case of $\langle d_{init} \rangle = 1.5$ nm this is not observed, because the fraction of sintered particles is very high anyway and also not for $\langle d_{init} \rangle = 3.5$ nm, because under these conditions the fraction of sintered particles is low, implying that the change in the PSD due to PM is low.

Fig. 5.6c shows the dependence of the fraction of sintered particles on different oxygen pressures p_{O_2} for different temperatures. This behavior with temperature was already seen in Fig. 5.3b, where the fraction of sintered particles increases with increasing temperature. Also observed is that PM is independent of p_{O_2} , which is expected for the model used. With increasing p_{O_2} the fraction of sintered particles increases for OR and PM \odot OR. For PM \odot OR, PM constitutes the lower limit for sintering and is identical at low p_{O_2} . With increasing p_{O_2} , OR becomes more dominant and at even higher O_2 pressures OR is identical to PM \odot OR. Thus PM dominates for $p_{O_2} < 0.1$ mbar, but for experimentally more relevant pressures, such as 40 mbar, OR is the more important sintering process. Interestingly, the crossover between OR and PM occurs at lower p_{O_2} with increasing temperature, indicating that

OR increases somewhat faster with increasing temperature. Fig. 5.6d shows the results of the same simulations as in Fig. 5.6c but the mean final diameter ($\langle d_{\text{final}} \rangle$) is measured instead of the fraction of sintered particles. It can be seen that both properties lead to exactly the same observations demonstrating the possible transferability of the experimentally measured change in mean diameter and simulated fraction of sintered particles.

It is apparent from Fig. 5.6b and 5.6c that the effect of PM and OR is not additive. Generally, the fraction of sintered particles via both PM and OR (PM \circ OR) is less than the sum of the fraction of sintered particles in the individual calculations. Simple additivity of both sintering mechanisms would be expected if they acted independently on different particles. In practice, the smallest particles are removed first, both through PM and OR since they are most mobile and least stable. Therefore, when comparing combined sintering (PM \circ OR) with the separate mechanisms, sintering is often less than the sum of the individual, isolated sintering mechanisms, as any given particle can of course only be removed once.

5.4 Conclusions

Sintering through particle migration and coalescence was investigated with a kMC-model employing diffusion constants obtained from first principles calculations. Generally, the extent of sintering is well-described through the diffusion constant, a function of both temperature and particle size. As expected, the extent of sintering increases with increasing particle concentration. Additionally, the effect of point defects on sintering has been studied explicitly. Generally, more and stronger binding defects lead to less sintering. However, beyond a certain binding strength, stronger binding does not further decrease sintering. The binding strength necessary to completely trap a particle for a certain time can be well estimated through the average escape using a lattice hop model and the diffusion constant of the given particle.

The kMC model for PM was combined with a mean-field model for OR which allows the simultaneous study of both processes. For experimentally relevant conditions ($p_{\text{O}_2} > 1$ mbar), it was found that OR is more important than PM. If both OR and PM are relevant, their combined effect (PM \circ OR) is usually smaller than the sum of the effects of the individual processes. This is likely due to the fact that only the smallest particles are mobile enough for PM. However, these particles are also the ones most readily annihilated through OR.

6 Gas phase diffusion model for Ostwald ripening

6.1 Introduction

First a kinetic Monte Carlo (kMC) model of gas phase diffusion will be described and tested by reproducing ideal gas parameters for ^{40}Ar . As second step, two model systems are investigated to compare the kMC model with analytical solutions of Fick's laws, then the kMC model will be extended to simulate the conditions assumed for the mean-field model of Ostwald ripening (OR) to study the limitations of that method.

6.2 Gas phase diffusion model

Here, a kMC model that describes the collision of an explicitly simulated molecule within a uniform background of ideal gas is developed. Similar models were developed to describe high power impulse magnetron sputtering and direct current sputtering.²²⁰ To calculate the flow of dilute gases often the Direct Simulation Monte Carlo (DSMC) method of G.A. Bird²²¹ is used. The DSMC is a probabilistic approach, where the number of simulated particles is not equal to the number of real particles. In consequence, it is not suitable to model the pathway of a single molecule influenced by a background gas.

In this approach, the background gas is not explicitly simulated but interacts with the molecule through collisions that follow from the temperature, its mass distribution, collision cross section and collective gas-flow.

First the kMC model of gas phase diffusion will be described and tested by reproducing ideal gas parameters for ^{40}Ar . As a second step, two model systems are investigated to compare the gas phase diffusion model with analytical solutions of Fick's laws.

6.2.1 Method

To simulate the diffusion of a particle through an ideal gas, the kMC approach with a Bortz–Kalos–Lebowitz (BKL) algorithm²²² is used, which is described in section 2.4. In an ideal gas, particles interact only through collisions and otherwise move linearly at constant velocity. The simulation approach contains explicitly simulated particles M_p (from now on simply referred to as particles) and a background gas, M_b . The particles do not interact with each other and do not change the properties of the background gas. This is expected to be a good approximation when the particles are present at very low concentration. This will be the case in the applications of interest, where mass transport between solid particles is mediated by species with low vapor pressure, while the gas phase is mainly composed of inert gas, air, or a reactive atmosphere. It is also a valid approach for the simulation of pure gas phase properties, where only a single type of particle is simulated. This will be the validation case for this model, the diffusion of ^{40}Ar in ^{40}Ar .

The only kMC processes are collisions between particles and the background gas, in between collision events the particles move with constant velocity. Initially, particles are supplied with certain velocities and from there on move until collisions change both direction and magnitude of the velocity.

Section 6.2 of this chapter is based on the following publication: Dietze, E. M.; Plessow, P. N., Kinetic Monte Carlo Model for Gas Phase Diffusion in Nanoscopic Systems. *J. Phys. Chem. C* 2018, 122, 21, 11524-11531. The other sections are unpublished.

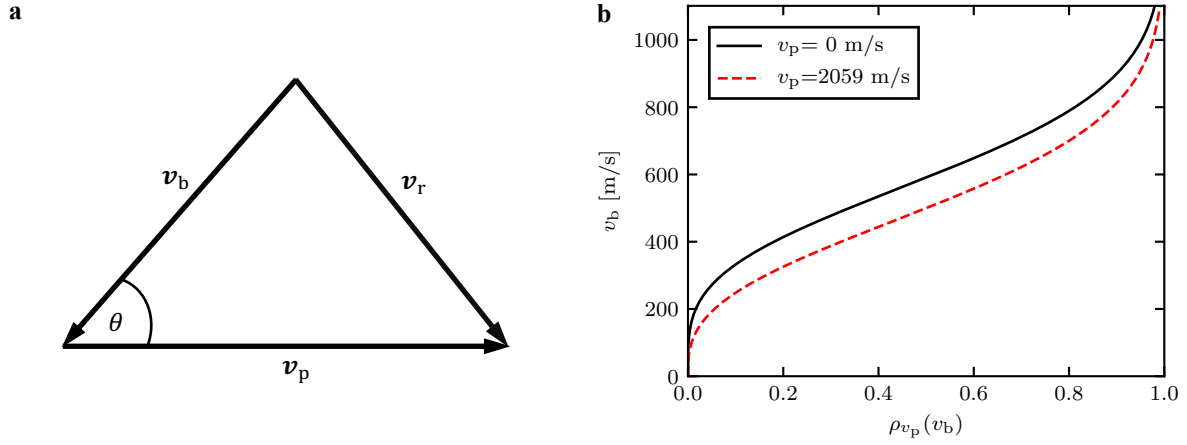


Figure 6.1: (a) Velocities v_1 and v_2 of the molecules M_1 and M_2 with the collision angle θ and their relative velocity v_r . (b) Inverted probability function of $v_b(\rho_{v_b}(v_p))$ for two different example velocities v_p .

In the moment of the collision, the distance between the centers of M_p and one molecule of M_b is $d_{av} = 1/2(d_p + d_b)$ with d_p and d_b being the diameters of M_p and M_b . In consequence, only molecules from the background can collide with M_p , which pass M_p with a distance less than d_{av} . The collision cross section follows as:

$$\sigma = \pi d_{av}^2. \quad (6.1)$$

Generally, the number of scattered molecules is proportional to the number of scattering events, $N_{scatter}$, per time and unit volume:

$$Z_p = N_{scatter} \sigma v. \quad (6.2)$$

In an ideal gas mixture with a molecule M_p with velocity v_p and a different kind of molecule M_b , which has a randomly oriented velocity v_b , the collision probability of M_p will be given by eq. (6.2), where v is replaced by the average relative velocity between M_p and M_b , \bar{v}_r :

$$Z_{pb} = n_b \sigma \bar{v}_r, \quad (6.3)$$

with n_b being the molecular density of M_b .

In consequence, the problem of finding Z_{pb} reduces to the calculation of \bar{v}_r . v_p relative to v_b varies only with the angle θ between the directions of motions (compare Fig. 6.1a). Because of the random orientation of the velocities, a fraction of $1/2 \sin \theta d\theta$ will move in directions with an angle θ with v_p .

The average value \bar{v}_r of v_r is:

$$\bar{v}_r = \frac{1}{2} \int_0^\pi v_r \sin \theta d\theta. \quad (6.4)$$

With $v_r^2 = v_p^2 + v_b^2 - 2v_p v_b \cos \theta$, it follows:

$$\bar{v}_r = \frac{1}{2} \int_0^\pi (v_p^2 + v_b^2 - 2v_p v_b \cos \theta)^{1/2} \sin \theta d\theta, \quad (6.5)$$

which can be solved analytically:

$$\begin{aligned} \bar{v}_r &= \frac{1}{6v_p v_b} \left[(v_p^2 + v_b^2 - 2v_p v_b \cos \theta)^{3/2} \right]_{\theta=0}^{\theta=\pi} \\ &= \frac{1}{6v_p v_b} [(v_p + v_b)^3 - |v_p - v_b|^3]. \end{aligned} \quad (6.6)$$

Depending on the ratio of v_p and v_b , \bar{v}_r is determined according to:

$$\bar{v}_r = v_p + \frac{v_b^2}{3v_p} \text{ if } v_p > v_b, \quad (6.7a)$$

$$\bar{v}_r = v_b + \frac{v_p^2}{3v_b} \text{ if } v_p < v_b. \quad (6.7b)$$

The velocities of the background gas are assumed to follow the Maxwell-Boltzmann distribution:

$$f(v_b) = 4\pi \left(\frac{m_b}{2\pi k_B T} \right)^{3/2} \cdot v_b^2 \cdot e^{-m_b v_b^2 / 2k_B T}, \quad (6.8)$$

with m_b being the mass of the background gas, T the temperature and k_B the Boltzmann constant.

To obtain the total rate of collision between M_p and M_b in the velocity range $v dv$ eqs. (6.3) and (6.6) are used:

$$z(v_p, v_b) dv_b = f(v_b) n_b \sigma \bar{v}_r dv_b. \quad (6.9)$$

Hence the total rate of collision of M_p is:

$$z(v_p) = \int_0^\infty z(v_p, v_b) dv_b. \quad (6.10)$$

The probability function for collision with a molecule with velocity $\leq v_b$ is:

$$\rho_{v_p}(v_b) = \frac{\int_0^{v_b} z(v_p, v') dv'}{z(v_p)} \quad (6.11)$$

This expression already includes all possible orientations of v_p and v_b . The inverted probability function is shown in Fig. 6.1b, where v_b is plotted against $\rho_{v_b}(v_p)$. In contrast to usual kMC algorithms, which have a finite number of processes, here are an infinite number of possible processes. This is due to the continuum nature of the background gas, where at any time all velocities follow the Maxwell-Boltzmann distribution. Fig. 6.2a illustrates $\rho_{v_b}(v_p)$, which is a smooth function (right side), whereas a finite number of rate constants would lead to a step-like curve (left side).

The direction of the velocity v_b , can be described with two angles θ and ϕ , using polar coordinates. As already mentioned, the angle between v_p and v_b is given by θ (see Figure 6.1a), while ϕ describes different orientations of v_b with respect to the direction of v_r . In the absence of an external field, all values of ϕ have an equal probability. Therefore, ϕ is chosen randomly in the range $[0, 2\pi]$.

Due to the proportionality between the probability function of θ and v_r , v_r can be used to calculate θ in the following way:

$$\rho_{v_r}(\theta) = \frac{\int_0^\theta d\theta' v_r(\theta')}{\int_0^\pi d\theta' v_r(\theta')}. \quad (6.12)$$

The denominator of eq. (6.12) is equal to \bar{v}_r and the numerator similar to eq. (6.6):

$$\begin{aligned} v_r(\theta') &= \frac{1}{6v_p v_b} (v_p^2 + v_b^2 - 2v_p v_b \cos \theta')^{3/2} \\ &= \underbrace{\frac{(2v_p v_b)^{3/2}}{6v_p v_b}}_{n_{v_p v_b}} \underbrace{\left(\frac{v_p^2 + v_b^2}{2v_p v_b} - \cos \theta' \right)}_{\tilde{f}(\theta')}. \end{aligned} \quad (6.13)$$

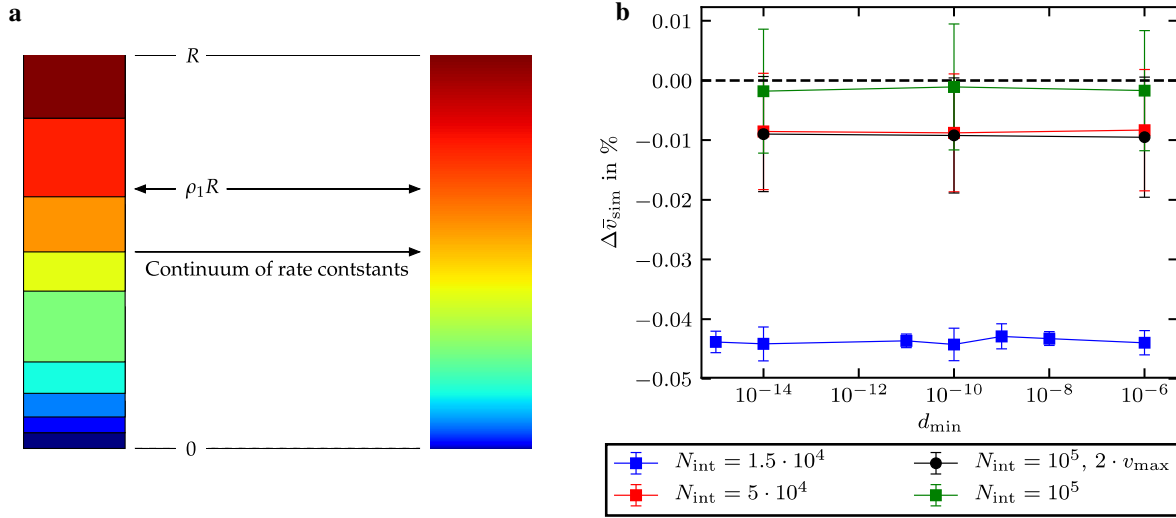


Figure 6.2: (a) Visualization of the transition from a finite number of processes (left side) to a continuum of processes (right side). (b) Dependence of v on d_{min} for different N_{int} over a large distance range. ($N_{v_p} = 2000$, $N_{\text{kMC}} = 3 \cdot 10^3$, $N_{\text{traj}} = 4 \cdot 10^5$, $v_{\text{max}} = 10 \cdot \bar{v}$ (apart from the black marked values), Number of calculations per point: 10)

Because the first term in eq. (6.13), $n_{v_p v_b}$ is independent of θ , eq. (6.12) reduces to:

$$\begin{aligned} \rho_{v_s}(\theta) &= \frac{\int_0^\theta d\theta' \tilde{f}(\theta')}{\int_0^\pi d\theta' \tilde{f}(\theta')} \\ &= \frac{(v_s - \cos \theta)^{3/2} - (v_s - 1)^{3/2}}{(v_s + 1)^{3/2} - (v_s - 1)^{3/2}}, \end{aligned} \quad (6.14)$$

in terms of the dimensionless parameter v_s :

$$v_s = \frac{v_p^2 + v_b^2}{2v_p v_b}. \quad (6.15)$$

The outcome of the scattering process depends on v_b and the angle θ . Due to its complicated functional form, $v_b(\rho_{v_b}(v_p))$ was precomputed before the kMC simulation. The velocity is discretised on an evenly spaced grid from 0 to $v_{\text{max}} = 10 \cdot \bar{v}_b$. \bar{v}_b is calculated according to eq. (6.22), below.

The integral in the numerator of eq. (6.11) is calculated numerically using the trapezoidal rule. The inverse of eq. (6.11), $v_b(\rho_{v_p})$, is interpolated. Since $\rho_{v_p}(v_b)$ varies very slowly for small v , where ρ_{v_p} is essentially 0 and for very large v , where ρ_{v_p} is essentially 1, it is the other way around for $v_b(\rho_{v_p})$. Here, $v_b(\rho_{v_p})$ varies most strongly when ρ_{v_p} is close to 0 or 1. While the points were chosen to be evenly spaced in v , they are generally unevenly spaced in ρ_{v_p} and are very dense in the region, where ρ_{v_p} is close to 0 or 1. This may cause problems in the interpolation of $v_b(\rho_{v_p})$. Therefore, it was chosen to use only a subset of the computed points for interpolation. Thus, a minimum distance d_{min} between the calculated points is introduced, which will generally lead to a more evenly spaced discretisation by removing points from the regions where they are very dense. As shown in Fig. 6.2b, the interpolation procedure is very stable when the parameter d_{min} is varied in the range of 10^{-6} to 10^{-15} . Thus $d_{\text{min}} = 10^{-10}$ is chosen, because it lies in the center of this range. The total number of points used to discretise v , N_{int} , determines how dense points are in the middle region. The convergence of the computed velocity and diffusion constant with N_{v_p} and N_{int} is shown Figure 6.3.

During the kMC calculation, for a given v_p and a random number ρ_{1a} , v_b was obtained by quadratic interpolation of $v_b(\rho_{v_b}(v_p) = \rho_{1a})$ using the three closest v_p -values of the precomputed grid. As shown in eq. (6.14), θ only depends on v_s , and the probability ρ_{v_s} . Eq. (6.14) can therefore be solved for θ :

$$\theta = \arccos \left(\left[-\rho_{v_s}(\theta) \left((v_s + 1)^{3/2} - (v_s - 1)^{3/2} \right) + (v_s - 1)^{3/2} \right]^{2/3} + v_s \right). \quad (6.16)$$

The collision process with a background molecule with a certain velocity and orientation is then chosen according to:

$$v_b = v_b(\rho_{v_p} = \rho_{1a}), \quad (6.17a)$$

$$\theta = \theta(\rho_{v_s} = \rho_{1b}), \quad (6.17b)$$

with $\rho_{1a,1b} \in (0, 1]$ being random numbers. The resulting particle velocity after the collision process is determined according to a hard-sphere elastic collision.

The change in time Δt is calculated according to eq. (2.25) and the position of the particles in space up to the collision process is updated:

$$\Delta \mathbf{x} = \Delta t \cdot \mathbf{v}_p. \quad (6.18)$$

As already mentioned, the precision of a kMC simulation depends on the interpolation procedure. Here, the precision depends on the number of points N_{vp} to precompute the probability distribution of v_b and N_{int} , the number of points to precompute the integral in eq. (6.11). To investigate the precision of the simulations, gas phase properties such as the diffusion coefficient D and the mean velocity $\bar{v} := \langle |\mathbf{v}| \rangle$ were studied.

The kMC simulation, with N_{kMC} steps, is repeated N_{traj} times. The particle is initialized with the velocity which has the highest probability according to the Boltzmann distribution. To allow the system to equilibrate, D_{sample} and \bar{v}_{sample} are calculated as follows for each trajectory after 100 initial steps ($n > 100$):

$$\bar{v}_{sample} = \frac{\sum_n v_n \cdot \Delta t_n}{t_{kMC}}, \quad (6.19)$$

$$D_{sample} = \left\langle \frac{\sum_{i=1}^3 x_{n,i}^2}{3 \cdot 2 \cdot \sum_{k=1}^n \Delta t_k} \right\rangle, \quad (6.20)$$

n being the current step and t_{kMC} the elapsed time excluding the 100 initial steps. v_n , Δt_n and $x_{n,i}$ are the mean velocity, change in time and the i^{th} -component of the particle position of each step n of the simulation. D_{sim} and \bar{v}_{sim} are calculated as the average over all simulated samples.

6.2.2 Parameter convergence for the example of self diffusion of Ar

As a model system, the self diffusion of ^{40}Ar is studied at a temperature of $T = 500$ K and a pressure of $p = 1$ bar.

Calculation of the diffusion coefficient

Following Kennard²²³, the diffusion coefficient is defined for a mixture of two ideal gases. The molecules are modeled as hard spheres.

The diffusion coefficient after the method of Maxwell²²⁴ and Chapman²²⁵ is:

$$D_{12} = \frac{3}{8} \sqrt{\frac{\pi}{2}} \frac{1}{n\sigma} \left[\frac{m_1 + m_2}{m_1 m_2} k_B T \right]^{1/2} \quad (6.21a)$$

and for the self-diffusion:

$$D_{11} = \frac{3\pi}{16\sqrt{2}} \frac{\bar{v}}{n\sigma}, \quad (6.21b)$$

with n the total number of molecules per unit volume, m_1 and m_2 the atomic masses. The mean velocity \bar{v} within the self-diffusion equation is:

$$\bar{v} = \sqrt{\frac{8k_B T}{\pi m}}. \quad (6.22)$$

According to the result of eq. (6.21a) the diffusion in a gas mixture is independent of the proportions of the mixture, because only n occurs in the formula. Regarding the fully theory as worked out by Chapman²²⁵ and by Enskog²²⁶ the variation of D_{12} with the proportions of the gas mixture is small. In general, eq. (6.21a) and eq. (6.21b) can be rewritten as:

$$D_{12} = (1 + \lambda_{12}) \frac{3}{8} \sqrt{\frac{\pi}{2}} \frac{1}{n\sigma} \left[\frac{m_1 + m_2}{m_1 m_2} k_B T \right]^{1/2} \quad (6.23a)$$

$$D_{11} = (1 + \lambda_{11}) \frac{3\pi}{16\sqrt{2}} \frac{\bar{v}}{n\sigma}. \quad (6.23b)$$

The exact theory gives for $\lambda_{11} = 0.017$ in the case of hard elastic spheres. λ_{12} has a maximum at $3^2/9 \cdot \pi - 1 = 0.132$ in the case of hard spheres with significantly different mass. Generally λ_{12} varies with the composition: the diffusion coefficient increases if the amount of the lighter molecules decreases.

In more common textbooks such as Atkins and de Paula¹ the diffusion coefficient for an ideal gas is defined as:

$$D_{11} = \frac{1}{3} \frac{\bar{v}}{\sqrt{2}n\sigma}, \quad (6.24)$$

which is equivalent to the equation derived from Landau and Lifschitz²²⁷ for the diffusion coefficient of a light gas in a heavy gas. Comparing eq. (6.24) and eq. (6.21b) the prefactor changes from $1/3$ to $3\pi/16$. Another example are the equations introduced by Wedler²²⁸:

$$D_{11} = \frac{1}{2} \frac{\bar{v}}{\sqrt{2}n\sigma}, \quad (6.25a)$$

$$D_{12} = \frac{1}{2} \frac{n_1 \lambda_2 \bar{v}_2 + n_2 \lambda_1 \bar{v}_1}{n_1 + n_2}, \quad (6.25b)$$

with $\lambda = \bar{v}/z$ as the mean-free path and z the collision frequency. In this case the prefactor is $1/2$ instead of $3\pi/16$ for D_{11} . Thus approximations in common textbooks deviate by 44% (Atkins and de Paula¹) or by 17% (Wedler²²⁸).

Convergence results

The diffusion coefficient $D_{\text{ref}}(^{40}\text{Ar}) = 3.388 \cdot 10^{-5} \pm 4 \cdot 10^{-8} \text{ m}^2/\text{s}$ was calculated according to eq. (6.23b). $\bar{v}_{\text{ref}}(^{40}\text{Ar}) = 514.69 \text{ m/s}$ follows from the ideal gas law.

Fig. 6.3 shows the decreasing deviation of D_{sim} and \bar{v}_{sim} from the reference values with increasing N_{int} (a) and N_{vp} (b) respectively. Taking the value of the last data point in Fig. 6.3b, the simulated diffusion coefficient is $D_{\text{sim}} = 3.3853 \cdot 10^{-5} \text{ m}^2/\text{s}$ which deviates by 0.09% from D_{ref} and is within the error range mentioned by Kennard. The simulated velocity is $\bar{v}_{\text{sim}} = 514.70 \text{ m/s}$, which deviates by 0.002% from \bar{v}_{ref} . The deviation is expected to be sufficient for sintering calculations and could be further reduced by increasing N_{int} and N_{vp} .

Fig. 6.4a shows the differential scattering cross section of ^{40}Ar for a constant collision energy of 0.062 eV at $T = 500 \text{ K}$ and $p = 1 \text{ bar}$ which qualitatively agrees with Phelps et al.²²⁹. The probability to have either small or high scattering angles is increased whereas the probability to find scattering angles between 20° and 160° is orders of magnitude smaller. Numerical noise is due to poor sampling in the range where collisions are less likely.

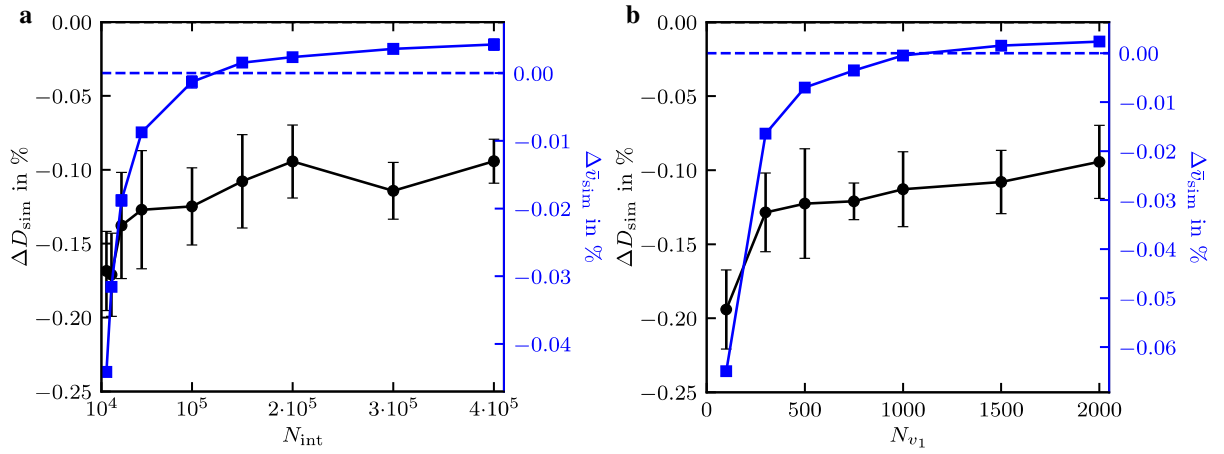


Figure 6.3: (a) Deviation of D_{sim} and \bar{v}_{sim} from D_{ref} and \bar{v}_{ref} with respect to N_{int} and constant $N_{\text{vp}} = 2000$ ($N_{\text{kMC}} = 3 \cdot 10^3$, $N_{\text{traj}} = 4 \cdot 10^6$, Number of calculations per point: 10, the error bars show the standard deviation of the simulated data with respect to the mean value). (b) Deviation of D_{sim} and \bar{v}_{sim} from D_{ref} and \bar{v}_{ref} with respect to N_{vp} and constant $N_{\text{int}} = 2 \cdot 10^5$ ($N_{\text{kMC}} = 3 \cdot 10^3$, $N_{\text{traj}} = 4 \cdot 10^6$, Number of calculations per point: 10, the error bars show the standard deviation of the simulated data with respect to the mean value).

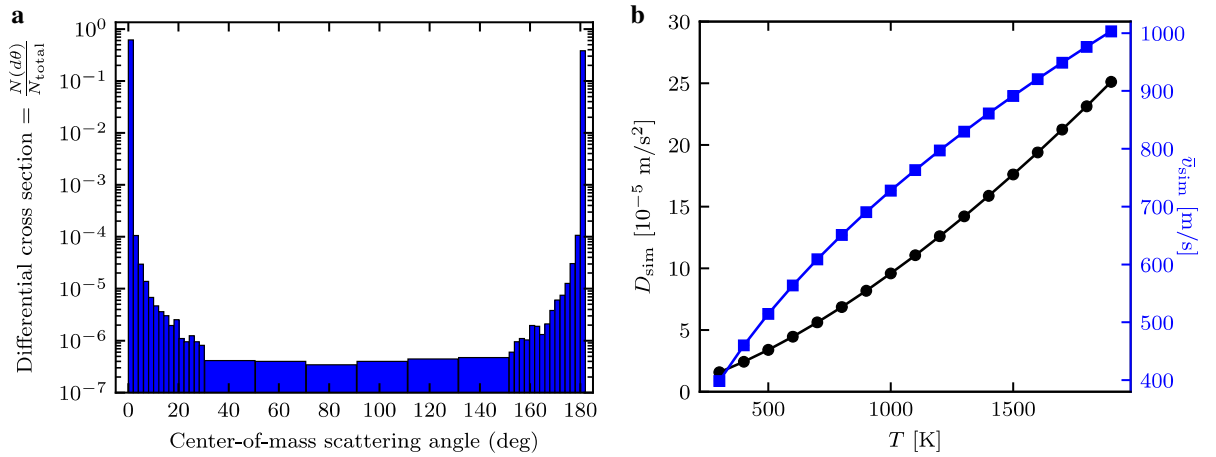


Figure 6.4: (a) Differential scattering cross section for a collision energy of 0.062 eV. ($N_{\text{vp}} = 2000$, $N_{\text{int}} = 2 \cdot 10^5$, $N_{\text{kMC}} = 3 \cdot 10^3$, $N_{\text{traj}} = 10^6$). (b) Comparison of D_{sim} (black circles) and D_{ref} (black line) and \bar{v}_{sim} (blue squares) and \bar{v}_{ref} (blue line) for different temperatures at $p = 1$ bar. ($N_{\text{vp}} = 2000$, $N_{\text{int}} = 2 \cdot 10^5$, $N_{\text{kMC}} = 3 \cdot 10^3$, $N_{\text{traj}} = 10^5$, Number of calculations per point: 20).

Fig. 6.4b shows D_{sim} and D_{ref} and the corresponding \bar{v}_{sim} and \bar{v}_{ref} for different temperatures at a constant pressure $p = 1$ bar. Both graphs are in excellent agreement over the whole temperature range. This shows that ideal gas properties can be simulated accurately using the presented kMC model with the parameters $N_{\text{vp}} = 2000$ and $N_{\text{int}} = 2 \cdot 10^5$, reproducing the mean velocity and the diffusion coefficient over a wide range of temperatures.

6.2.3 Diffusion between parallel walls

The first example is the diffusion of single atoms between two parallel surfaces with a surface area A and a distance Δz along the z -axis. The system is infinitely large in two dimensions and is described with a square unit cell with the surface area A . Ultimately A does not affect the outcome of the simulation (per a given surface area). However, A controls the rate constant for emission and adsorption for a given surface area. Choosing a very small surface area of $A = 10^{-16}$ m² results in a very small gas phase volume in the unit cell. This in turn means that during the simulation generally only one particle is present in the gas phase which greatly simplifies the analysis of the flux, as opposed to a situation with a larger volume and a larger number of particles in the gas phase.

Atoms can be emitted from both surfaces with rate constants $K_{1,2}$ according to their chemical potentials $\mu_{1,2}$. In the case of surface collisions, atoms are adsorbed with a probability that is given by the sticking coefficient S . The diffusion of Pt(g) in between clean Pt-surfaces and in a pure ⁴⁰Ar gas phase will be studied. In this model $S = 1$ is chosen as is appropriate for Pt(g). More complex surface-gas interactions could be incorporated through an angle- and velocity-dependent sticking coefficient. The rate equation for atom emission is defined²⁷ as:

$$K_{1,2} = \frac{A \cdot S}{\sqrt{2\pi \cdot m \cdot k_B T}} p^\circ \exp \frac{\mu_{1,2} - \Delta G^\circ}{k_B T} \quad (6.26)$$

with p° the standard pressure and ΔG° the standard Gibbs free energy in the gas phase.

The atoms are emitted with a velocity distribution for v_z corresponding to that for collision of the ideal gas with a surface with a normal vector in z -direction, so that emission and collision are in equilibrium at the interface. Importantly, this velocity distribution is not the 1D Maxwell-Boltzmann (MB)-distribution, $\rho(v_z)$, but proportional to $v_z \cdot \rho(v_z)$ (Fig. 6.5a)^{230–232}. v_x and v_y are chosen according to the 1D MB-distribution.

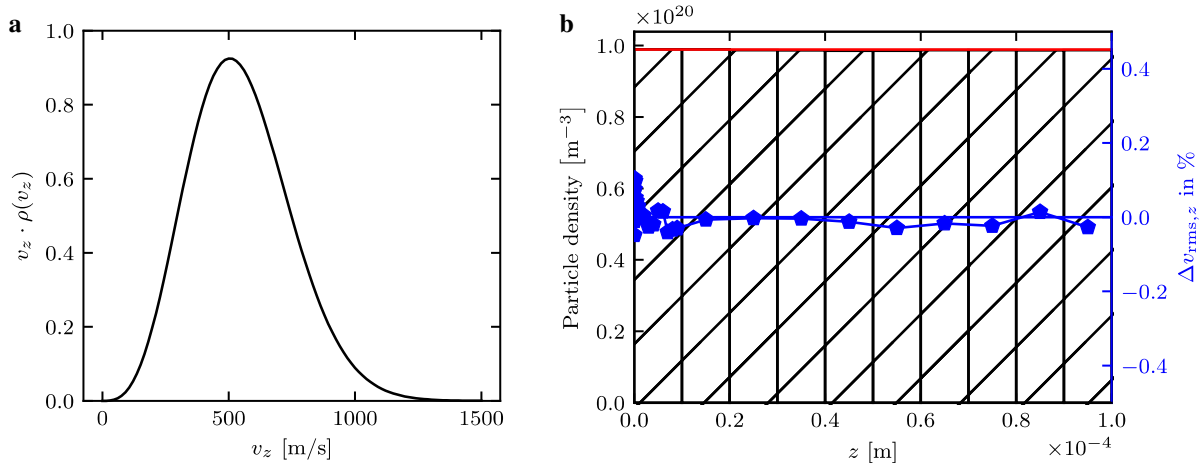


Figure 6.5: (a) Probability distribution $v_z \cdot \rho(v_z)$ at $T = 2000$ K for Pt atoms. (b) Bars: Simulated particle density for $\Delta\mu = 0$. Red line: Particle density in thermodynamic equilibrium. Blue line with symbols: Deviation of the simulated mean squared velocity from $v_{\text{rms},z}^{\text{ref}} = 291.40$ m/s. (kMC parameters: $\Delta z = 10^{-4}$ m, $N_{\text{vp}} = 2000$, $N_{\text{int}} = 10^5$, $N_{\text{kMC}} = 2 \cdot 10^7$, $N_{\text{traj}} = 25$, $T = 2000$ K, $p = 1$ bar).

For a system in equilibrium, the potential difference of the walls is $\Delta\mu = 0$ eV. In consequence all gas properties should be constant throughout the system. In Fig. 6.5b the calculated mean squared velocity $v_{\text{rms},z}$ of the

z -component is plotted and is in good agreement with the theoretical value $v_{\text{rms},z}^{\text{ref}} = 291.40 \text{ m/s}$ at $T = 2000 \text{ K}$. The calculated particle density remains constant over the whole range, in agreement with the one given by thermodynamic equilibrium.

For all calculations, the chemical potential $\mu_1 = -5.82 \text{ eV}^{179}$ of the left surface was kept constant at the value of solid Pt. μ_2 was chosen to be variable with the condition $\mu_2 > \mu_1$, causing a flux from the right surface to the left.

Solution for the particle flux from Fick's laws

With eq. (6.26), the outward flux J_{out} of either surface is:

$$J_{\text{out}} = \frac{S \cdot A}{\underbrace{\sqrt{2\pi \cdot m \cdot k_B T}}_{\tilde{\alpha}}} \underbrace{p^\circ \exp\left(\frac{\mu_{1,2} - \Delta G^\circ}{k_B T}\right)}_{p_{\text{eq}}} \quad (6.27)$$

and the inward flux J_{in} :

$$J_{\text{in}} = \tilde{\alpha} \cdot p_{\text{in}}. \quad (6.28)$$

The total flux follows as:

$$\begin{aligned} J_{\text{tot}} &= J_{\text{out}} - J_{\text{in}} = \tilde{\alpha} \cdot (p_{\text{eq}} - p_{\text{in}}), \\ &= \underbrace{\tilde{\alpha} \cdot k_B T}_{\alpha} \underbrace{(n_{\text{eq}} - n_{\text{in}})}_{\Delta n}, \end{aligned} \quad (6.29)$$

with $p = nk_B T$ from the ideal gas law and n being the number of particles per unit volume.

Fick's laws are used to calculate the change in the number of particles per unit volume Δn for the stationary case:

$$1^{\text{st}} \text{ law: } J_{\text{tot}} = -D \cdot \nabla n, \quad (6.30)$$

$$\Rightarrow \frac{dn}{dz} = -\frac{J_{\text{tot}}}{D}, \quad (6.31)$$

$$2^{\text{nd}} \text{ law: } \frac{d^2 n}{dz^2} D = \frac{dn}{dt} \stackrel{!}{=} 0. \quad (6.32)$$

Because of the one dimensional diffusion along the z -axis, ∇n reduces to dn/dz . In the stationary case (eq. (6.32)) the total flux at the reservoirs has to be preserved:

$$J_1^{r=0} = -J_2^{r=z}, \quad (6.33)$$

$$\alpha(n_{\text{eq}}^0 - n^0) = \alpha(n^z - n_{\text{eq}}^z), \quad (6.34)$$

$$\Rightarrow \Delta n = n_{\text{eq}}^0 - n^0 = n^z - n_{\text{eq}}^z. \quad (6.35)$$

From eq. (6.30) it follows:

$$\begin{aligned} \frac{dn}{dz} &= \frac{n^z - n^0}{\Delta z} = \frac{n_{\text{eq}}^z - n_{\text{eq}}^0 + 2\Delta n}{\Delta z}, \\ \Rightarrow \Delta n &= \frac{-D\Delta n_{\text{eq}}}{\alpha\Delta z + 2D}, \end{aligned} \quad (6.36)$$

with $\Delta n_{\text{eq}} = n_{\text{eq}}^z - n_{\text{eq}}^0$. For large Δz the limit is: $\lim_{\Delta z \rightarrow \infty} J_{\text{tot}} = 0$.

Thus, the total flux $J_{\text{total}} = J_{\text{out}} - J_{\text{in}}$, which generally consists of the out-coming and in-coming particle flux, is:

$$J_{\text{total}} = \Delta n \cdot \alpha = \frac{-D\Delta n_{\text{eq}}}{\alpha\Delta z + 2D} \cdot \alpha, \quad (6.37)$$

with $\alpha = k_B T (2\pi \cdot m k_B T)^{-1/2}$ and $\Delta n_{\text{eq}} = (p_{2,\text{eq}} - p_{1,\text{eq}}) / k_B T$, $p_{i,\text{eq}}$ being the equilibrium pressure at which surface i would be in equilibrium with the gas phase.

Extension of the kMC model

In addition to the gas phase scattering, the emission of an atom and the adsorption/reflection on the surfaces are considered as kMC processes. In the absence of gas phase collisions, the atoms move linearly with constant velocity until they collide with a surface and are either adsorbed or reflected. In the presence of an external potential (not considered in this work), the trajectory could be modified accordingly. The time to collision with a background-gas particle, Δt is computed first according to eq. (2.25) and is used to check if any atom in the gas phase collides with one of the surfaces before gas phase collision. In the case of a collision with the surface within Δt , Δt is changed to the actual collision time Δt_{col} and the atom is adsorbed or reflected, depending on S . The positions of all other atoms in the gas phase are then updated using Δt . Formally, this kMC approach can be considered as a first-reaction method²³³, where possible processes are collision with the surfaces, collision in the gas phase and emission from the surfaces. Here, the wall-collision processes are deterministic. The probability for any other process to occur follows from the BKL-algorithm described in section 2.4, e.g. from the total rate constants of these processes and eq. (2.25).

From the kMC simulations, the total flux of platinum atoms $J_{\text{total}}^{\text{num}}$ is calculated as:

$$J_{\text{total}}^{\text{num}} = \frac{(N_{E1} - N_{C1}) - (N_{E2} - N_{C2})}{2 \cdot A \cdot t_{\text{kMC}}}, \quad (6.38)$$

$N_{E(1,2)}$ and $N_{C(1,2)}$ being the number of emitted and adsorbed particles on the surfaces.

Simulation results

$T = 2000$ K was chosen as a temperature at which the formation of Pt(g) is relevant. The total flux for different pressures and distances at $T = 2000$ K is shown in Fig. 6.6a. The solid lines represent the solution of eq. (6.37) and the lines with point symbols the simulated values. The general behavior of both curves is similar and so is the effect of the background pressure. For distances $\Delta z > 10^{-4}$ m for $p = 10$ bar or increased Δz for smaller pressures, both models give the same result and converge to zero for large distances, due to a negligible concentration gradient. For distances $\Delta z < 10^{-4}$ m, the kMC model shows a higher flux than the continuum model. In this case, the simulated flux is twice the flux given by the continuum model for $\Delta z < 5 \cdot 10^{-9}$ m. On this length scale, there is an increased probability for particles to be emitted and adsorbed on the other wall without scattering processes.

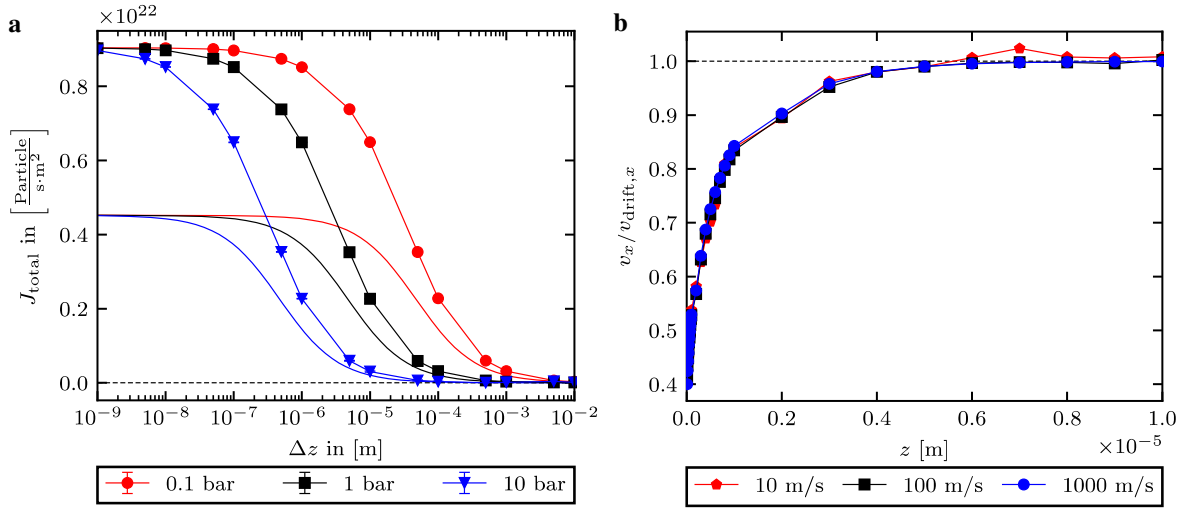


Figure 6.6: (a) Total flux between two parallel surfaces for different pressures and surface distances at $T = 2000$ K and $\Delta\mu = 100$ meV. Solid lines with symbols: Simulated flux. Solid lines: Flux according to eq. (6.37). (kMC parameters: $N_{\text{vp}} = 2000$, $N_{\text{int}} = 10^5$, $N_{\text{kMC}} = 10^9$, $N_{\text{traj}} = 10$). (b) Convergence of the ratio of the calculated velocity v_x to the applied drift velocity $v_{\text{drift},x}$ at $T = 2000$ K, $p = 1$ bar, $\Delta z = 10^{-4}$ m and $\Delta\mu = 0$ eV, $v_{\text{drift},x} = 10$ 100 and 1000 m/s. (kMC parameters: $N_{\text{vp}} = 2000$, $N_{\text{int}} = 10^5$, $N_{\text{kMC}} = 2 \cdot 10^7$, $N_{\text{traj}} = 50$).

Carrillo et al.⁷⁹ investigated experimentally how flowing air reduces the amount of Pt in a Pt/SiO₂ sample, by studying the Pt particle size distribution (PSD). They concluded that the flowing air sweeps volatile PtO₂(g) off the surface. In this kMC model, the flowing air can be simulated by applying a drift velocity v_{drift} to the background gas. Thus simulates how volatile Pt(g) is swept off the surface. In order to achieve significant pressures of Pt(g) again $T = 2000$ K is employed, e.g. higher temperatures than necessary to cause emission of PtO₂(g), and a drift velocity in x -direction $v_{\text{drift},x}$ applied. To find out for which distance range from a surface the Pt particles adapt to the drift velocity, Fig. 6.6b shows the ratio of v_x to $v_{\text{drift},x}$ for $v_{\text{drift},x} = 10$ 100 and 1000 m/s. It can be seen that v_x converges within $5 \cdot 10^{-6}$ m to the applied drift velocity, independent of its magnitude. In Fig. 6.7 the simulated particle density (PD) is shown as bars, in good agreement with the PD according to Fick's law.

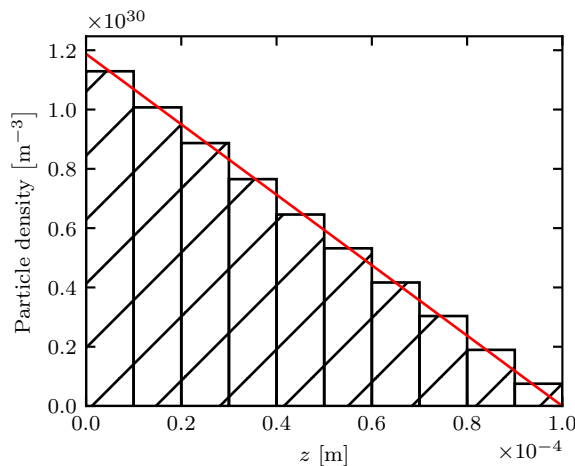


Figure 6.7: Bars: Simulated particle density for different distances from the emitting surface, Red line: Particle density according to Fick's law at $T = 2000$ K, $p = 1$ bar, $\Delta z = 10^{-4}$ m and $\Delta\mu = 4$ eV (kMC parameters: $N_{\text{vp}} = 2000$, $N_{\text{int}} = 10^5$, $N_{\text{kMC}} = 2 \cdot 10^7$, $N_{\text{traj}} = 50$).

6.2.4 Diffusion between two spheres

As a second example, the diffusion of single particles between two concentric spheres is studied. Again, Pt is the surface material and ^{40}Ar constitutes the gas phase. The chemical potential of the outer sphere is kept constant at $\mu_2 = -5.82$ eV and the inner one, $\mu_1 = -1.82$ eV chosen. The high $\Delta\mu$ increases the ratio of the probabilities of emissions from the inner sphere and outer sphere. This reduces the computational cost as the fraction of attempted processes that are relevant for diffusion increases. The radius r_1 of the inner sphere is 1 nm. In general, the Gibbs-Thomson-equation²³⁴ could be used to calculate a radius dependent chemical potential. The emission rate is calculated according to eq. (6.26). As before, the velocity distribution is chosen to be in equilibrium with the gas phase. In contrast to the parallel surfaces, the surface areas of the spheres are not equal but depend on the radius.

Solution for the particle flux from Fick's laws

Diffusion occurs through the gas phase between the inner sphere with radius r_1 and the outer sphere with radius r_2 . The spheres are centered at the same origin. The distance Δz is defined as $\Delta z = r_2 - r_1$ and the surface area $A_{1,2} = 4\pi r_{1,2}^2$. Because of the spherical system, Fick's laws are transformed into spherical coordinates. It follows analogously to eq. (6.30) and (6.32):

$$\text{1st law: } J_{\text{tot}} = -D \cdot \left(\frac{dn}{dr} + \frac{1}{r} \frac{dn}{d\theta} + \frac{1}{r \cdot \sin\theta} \frac{dn}{d\phi} \right), \quad (6.39)$$

$$\text{2nd law: } \frac{1}{r^2} \frac{d}{dr} \left(r^2 \frac{dn}{dr} \right) D = \frac{dn}{dt}, \quad (6.40)$$

$$\Rightarrow \text{steady state: } 0 = \frac{d^2n}{dr^2} + \frac{2}{r} \frac{dn}{dr}. \quad (6.41)$$

Because of the spherical symmetry, the flux from the surface is the same in each direction. The solution of the differential equation eq. (6.41) has the following general form for the steady state:

$$n(r) = c_1/r + c_2, \quad (6.42)$$

with c_1 and c_2 being constants. According to the conditions:

$$J(r_1) = \alpha(n_{\text{eq}}^{r_1} - n^{r_1}), \quad (6.43)$$

$$J(r_1) = -D \frac{dn^{r_1}}{dr_1}, \quad (6.44)$$

$$J(r_2) = \alpha(-n_{\text{eq}}^{r_2} + n^{r_2}), \quad (6.45)$$

$$J(r_2) = D \frac{dn^{r_2}}{dr_2}, \quad (6.46)$$

with $n(r = r_1) = n^{r_1}$, $n(r = r_2) = n^{r_2}$ and $\alpha = k_B T / \sqrt{2\pi \cdot m \cdot k_B T}$. Using eq. (6.42) for n^{r_1} and n^{r_2} , c_1 can be expressed as:

$$n^{r_1} - n^{r_2} = \frac{c_1}{r_1} - \frac{c_1}{r_2} = c_1 \left(\frac{1}{r_1} - \frac{1}{r_2} \right), \quad (6.47)$$

$$c_1 = \frac{n^{r_1} - n^{r_2}}{\frac{1}{r_1} - \frac{1}{r_2}}. \quad (6.48)$$

The first derivative of eq. (6.42) is:

$$\frac{dn(r)}{dr} = -\frac{c_1}{r^2}, \quad (6.49)$$

$$= \frac{n^{r_2} - n^{r_1}}{r^2 \left(\frac{1}{r_1} - \frac{1}{r_2} \right)}, \quad (6.50)$$

$$\left. \frac{dn(r)}{dr} \right|_{r=r_1} = \frac{n^{r_2} - n^{r_1}}{r_1^2 \left(\frac{1}{r_1} - \frac{1}{r_2} \right)}. \quad (6.51)$$

With eq. (6.51) and a similar one for $\left. \frac{dn(r)}{dr} \right|_{r=r_2}$ two equations for n^{r_2} can be found giving n^{r_1} by comparison as shown:

$$\alpha \cdot (n_{\text{eq}}^{r_1} - n^{r_1}) = -D \left. \frac{dn(r)}{dr} \right|_{r=r_1}, \quad (6.52)$$

$$n^{r_2} = n^{r_1} - \frac{\alpha \cdot r_1^2 \cdot (n_{\text{eq}}^{r_1} - n^{r_1}) \left(\frac{1}{r_1} - \frac{1}{r_2} \right)}{D}, \quad (6.53)$$

$$\alpha \cdot (n^{r_2} - n_{\text{eq}}^{r_2}) = -D \left. \frac{dn(r)}{dr} \right|_{r=r_2}, \quad (6.54)$$

$$n^{r_2} = \frac{\alpha \cdot r_2^2 \left(\frac{1}{r_1} - \frac{1}{r_2} \right) n_{\text{eq}}^{r_2} + D \cdot n^{r_1}}{\alpha \cdot r_2^2 \left(\frac{1}{r_1} - \frac{1}{r_2} \right) + D}, \quad (6.55)$$

$$\Rightarrow n^{r_1} = \frac{n_{\text{eq}}^{r_1} \alpha r_1^2 r_2 - n_{\text{eq}}^{r_1} \alpha r_1 r_2^2 - D n_{\text{eq}}^{r_1} r_1^2 - D n_{\text{eq}}^{r_2} r_2^2}{\alpha r_1^2 r_2 - \alpha r_1 r_2^2 - D r_1^2 - D r_2^2}. \quad (6.56)$$

The first and second derivative of eq. (6.43) are:

$$\frac{dJ(\Delta z)}{d\Delta z} = (n_{\text{eq}}^{r_2} - n_{\text{eq}}^{r_1}) (\alpha (r_1 + \Delta z) - 2D), \quad (6.57)$$

$$\frac{d^2J(\Delta z)}{d\Delta z^2} = (n_{\text{eq}}^{r_2} - n_{\text{eq}}^{r_1}) \alpha. \quad (6.58)$$

Thus a maximum can be found for pressures $p \leq 4.7 \cdot 10^8$ Pa at $T = 2000$ K. The extremum is a maximum because $n_{\text{eq}}^{r_2} > n_{\text{eq}}^{r_1}$ for all pressures and thus $\frac{d^2J(\Delta z)}{d\Delta z^2} < 0$. The maximum is small and thus doesn't influence the general comparison between the results of the kMC simulations and of eq. (6.43).

When the volume between the spheres becomes small, the gas phase consists in reality only of a small discrete number of molecules. The implicit background model does not provide an accurate description of this situation. However, since the number of collisions is small in this case anyway, this shouldn't be a significant problem.

Simulation results

In analogy to a system involving real nanoparticles, the flux from the inner sphere $J(r_1)$, eq. (6.43), is studied, mimicking a sintering nanoparticle. Eq. (6.43) shows that $J(r_1)$ not only depends on r_1 and μ_1 but also r_2 and μ_2 . With increasing r_2 , the surface area of the outer sphere increases quadratically. This generally leads to a faster adsorption of particles emitted from the inner sphere. Eventually, at large r_2 the system resembles an open system where the background pressure of Pt(g) is determined by the outer sphere, e.g. it follows from the chemical potential of solid platinum. The limit given by the open system is plotted as a dashed black line in Fig. 6.8.

A competing effect is that, with increasing r_2 , diffusion limitations, which depend on the pressure, become more important. Fig. 6.8 shows the flux from a sphere with $r_1 = 1$ nm at $T = 2000$ K, different pressures and surface distances. The solid lines show the flux according to eq. (6.43). For 1 bar the flux increases with increasing Δz and

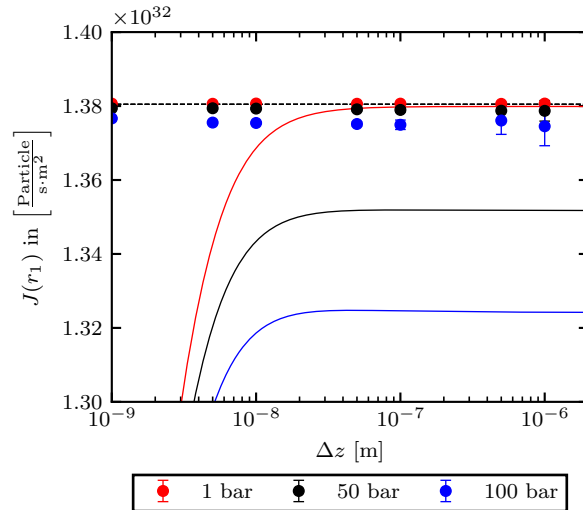


Figure 6.8: Total flux between two centered spheres for different pressures and surface distances at $T = 2000$ K, $r_1 = 1$ nm and $\mu_1 = -1.82$ eV (kMC parameters: $N_{vp} = 2000$, $N_{int} = 10^5$, $N_{kMC} = 4 \cdot 10^8$, $N_{traj} = 20$).

converges to the flux of an open system, which is also the case for smaller pressures. For 50 bar and 100 bar, the flux according to Fick's laws increases and converges to a constant value for $\Delta z > 10^{-7}$ m which is smaller than the flux of the open system. From the kMC simulations, the flux of the inner sphere is calculated as:

$$J^{num}(r_1) = \frac{(N_{E1} - N_{C1})}{A \cdot t_{kMC}}. \quad (6.59)$$

The simulated flux is shown in Fig. 6.8 as point symbols. For 1 bar, the simulated flux is constant with increasing surface distance and agrees with the value of an open system. For 50 bar and 100 bar the flux is smaller than the one given by an open system but larger than the flux according to eq. (6.43). The calculations show only a small dependence on the pressure. Similar to the parallel surfaces, it is expected that the calculated flux will converge to the flux of Fick's laws for high Δz .

6.2.5 Conclusions

It was shown that ideal gas properties, in particular the diffusion constant, can be simulated accurately using the developed kMC model. The model describes the collisions of an explicitly simulated molecule in a background gas. This approach can furthermore be used to simulate mass-transport through the gas phase between surfaces. For model systems, it was found that solutions based on Fick's laws underestimate mass transport if the systems are on the nanometer scale. This can be explained by the long mean free path in the gas phase that leads to a sizable number of trajectories where particles are not scattered by the background gas. Such an effect can not be predicted by standard continuum models and it is expected that this is important in systems where gas phase diffusion occurs on the nanoscale. In the following sections the gas phase transport between nanoparticles will be studied.

6.3 Explicit modeling of Ostwald ripening

Using the gas phase diffusion model, Ostwald ripening can be simulated explicitly in a simulation box with periodic boundary conditions in x - and y -directions. The surface, at $z = 0$, is assumed not to be interacting with the gas phase, thus molecules striking the surface are reflected elastic. The surface supports nanoparticles, which are

characterized by their number of atoms N_{Pt} , from which an effective diameter d_{eff} can be calculated under the assumption that the nanoparticle is represented as half-sphere:

$$d_{\text{eff}} = \left(\frac{3 \cdot V_{\text{Pt}} \cdot N_{\text{Pt}}}{2 \cdot \pi} \right)^{1/3} \quad (6.60)$$

with $V_{\text{Pt}} = 15.1 \text{ \AA}^3$, the volume per bulk atom¹⁷⁹. The simulation box can contain several nanoparticle, which do not overlap. The nanoparticles consist of Pt atoms and emit volatile $\text{PtO}_2(\text{g})$ ²⁶. Depending on the gas phase composition and pressure, the rate for atom emission is similar to eq. (6.26):

$$K_{\text{NP}} = \frac{S \cdot A}{2 \cdot \pi \cdot m_{\text{PtO}_2} \cdot T \cdot k_B} p_{\text{O}_2} \exp \left(\frac{-\Delta G_{\text{form}}(\text{PtO}_2) + \mu_{\text{NP}} - \mu_{\text{Pt}}^{\text{bulk}}}{T \cdot k_B} \right), \quad (6.61)$$

with p_{O_2} , the partial pressure of Oxygen in the gas phase, $\Delta G_{\text{form}}(\text{PtO}_2) = 1.69 \text{ eV}$ ²⁷, the free energy of formation of PtO_2 , which is assumed to be temperature independent, $m_{\text{PtO}_2} = 227.077 \text{ u}$ ²³⁵, the mass of PtO_2 , $\mu_{\text{NP}} = \mu_{\text{Pt}}^{\text{bulk}} + (2 \cdot 6.613)/d_{\text{eff}}$ ²⁷, the chemical potential of a nanoparticle, depending on its diameter and $\mu_{\text{Pt}}^{\text{bulk}} = -5.82 \text{ eV}$ ¹⁷⁹, the experimental bulk chemical potential of Pt. For the adsorption of PtO_2 and the following dissociation on the nanoparticle, it is assumed that the dissociation is fast compared to the redesorption for coverages below $\theta_0^0 = 2/9$ as shown by Plessow and Abild-Pedersen²⁷.

During the calculation units are defined which are similar to those often used in theoretical chemistry, known as atomic units²³⁶: for the length unit: 1 \AA , the mass unit: 1 u , the time unit: 1 ps . The energy E_0 , the temperature T_0 and pressure p_0 are a combination of these:

$$\begin{aligned} E_0 &= m_0 \cdot \left(\frac{x_0}{s_0} \right)^2 \\ T_0 &= E_0/k_B \\ p_0 &= \frac{m_0}{x_0 s_0^2} \\ k_B &= 1 \end{aligned}$$

Similar to the diffusion between two walls, the emission of a molecule and the adsorption/reflection of it are considered as kMC processes, but in this case the molecule adsorbs on the nanoparticle and is reflected from the surface which is not covered by the nanoparticle. The height of the simulation box is defined as $z = z_{\text{box}}$. At z_{box} the molecule is either reflected or absorbed. The first case is discussed in the following section 6.3.1 for Ostwald ripening of a closed system. The second case could be used to resemble an open system. In the closed system the total number of atoms/molecules of the system remains constant over time. In the open system the number would decrease, because those molecules adsorbed at z_{box} are not considered further during the simulation.

Implications of periodic boundary conditions

Periodic boundary conditions applied in the x - and y -directions, are such that molecules in the gas phase which leave the simulation box in $+x$ -direction reenter the simulation box at $-x$. The direction of the velocity of the gas phase molecule is not altered. In Figure 6.9a the situation with periodic boundary conditions in 2D is illustrated to show the determination of the collision between the molecule and the nanoparticles. The parameters used in the following are visualized in Fig. 6.9b in a side-view of one supported nanoparticle with one molecule in the gas phase.

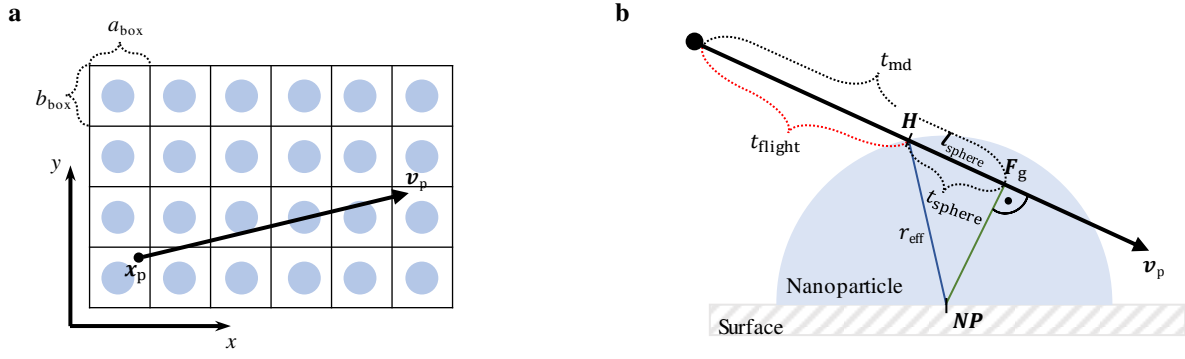


Figure 6.9: (a) 2D projection of the periodically repeated simulation box containing one nanoparticle (light blue circle) and one molecule (black point). The velocity of the particle \mathbf{v}_p is indicated with a black arrow. (b) Side-view of one supported nanoparticle with one molecule in the gas phase. All the parameters described in the text are indicated.

The molecule is characterized by its position $\mathbf{x}_p = (p_x, p_y, p_z)$ and velocity $\mathbf{v}_p = (v_x, v_y, v_z)$. The nanoparticle on the surface is characterized by its radius $r_{\text{eff}} = d_{\text{eff}}/2$ and general position within the periodic boundary conditions:

$$\mathbf{NP} = \begin{bmatrix} x_{\text{NP}} \\ y_{\text{NP}} \\ 0 \end{bmatrix} + n_a \begin{pmatrix} 1 \\ 0 \\ 0 \end{pmatrix} + n_b \begin{pmatrix} 0 \\ 1 \\ 0 \end{pmatrix} \cdot \begin{pmatrix} a_{\text{box}} \\ b_{\text{box}} \\ 0 \end{pmatrix}, \quad (6.62)$$

with $x_{\text{NP}}, y_{\text{NP}}$ the position of the nanoparticle in reduced length units, $a_{\text{box}}, b_{\text{box}}$ the size of the simulation box in x and y direction respectively and n_a (n_b) the number of periodically repeated simulation boxes in x (y).

A possible collision between the molecule and the nanoparticle is determined by calculating the minimal distance between \mathbf{NP} and the trajectory of the molecule $\mathbf{g}_p = \mathbf{x}_p + t_{\text{md}}\mathbf{v}_p$. The general point closest to the position of the nanoparticle is:

$$\mathbf{F}_g = \begin{pmatrix} p_x + t_{\text{md}}v_x \\ p_y + t_{\text{md}}v_y \\ p_z + t_{\text{md}}v_z \end{pmatrix} \quad (6.63)$$

The distance between the nanoparticle and the general point is:

$$\mathbf{F}_g - \mathbf{NP} = \begin{pmatrix} p_x + t_{\text{md}} \cdot v_x - a_{\text{box}} \cdot (x_{\text{NP}} + n_a) \\ p_y + t_{\text{md}} \cdot v_y - b_{\text{box}} \cdot (y_{\text{NP}} + n_b) \\ p_z + t_{\text{md}} \cdot v_z \end{pmatrix} = \mathbf{G}_{\text{NP}} \quad (6.64)$$

The distance is minimal if $\mathbf{G}_{\text{NP}} \cdot \mathbf{v} = 0$:

$$\begin{aligned} 0 &= p_x v_x + t_{\text{md}} v_x^2 - a(x + n_a)v_x + p_y v_y + t_{\text{md}} v_y^2 - b(y + n_b)v_y + p_z v_z + t_{\text{md}} v_z^2 \\ &= \mathbf{v}_p \cdot \mathbf{x}_p + t_{\text{md}} |\mathbf{v}_p|^2 - \mathbf{NP} \cdot \mathbf{v}_p \end{aligned} \quad (6.65)$$

$$t_{\text{md}} = \frac{\mathbf{NP} \cdot \mathbf{v}_p - \mathbf{v}_p \cdot \mathbf{x}_p}{|\mathbf{v}_p|^2}. \quad (6.66)$$

t_{md} is the time of flight to the point minimal in distance with \mathbf{NP} . To calculate the time of flight t_{flight} , of the particle to the border of the nanoparticle, the time in the sphere t_{sphere} is calculated based on the Pythagorean theorem:

$$\begin{aligned} |\mathbf{F}(t_{\text{md}})\mathbf{H}|^2 &= r_{\text{eff}}^2 - |\mathbf{F}(t_{\text{md}})\mathbf{NP}|^2 = |\mathbf{l}_{\text{sphere}}|^2 \\ &= (F_x - l_x)^2 + (F_y - l_y)^2 + (F_z - l_z)^2 \\ &= (F_x - (F_x - t_{\text{sphere}}v_x))^2 + (F_y - (F_y - t_{\text{sphere}}v_y))^2 + (F_z - (F_z - t_{\text{sphere}}v_z))^2 \\ &= t_{\text{sphere}}^2 v_x^2 + t_{\text{sphere}}^2 v_y^2 + t_{\text{sphere}}^2 v_z^2 \end{aligned}$$

$$t_{\text{sphere}} = \sqrt{\frac{|\mathbf{l}_{\text{sphere}}|^2}{|\mathbf{v}_p|^2}} \quad (6.67)$$

with \mathbf{H} the crossing point of the molecule and the sphere of the nanoparticle and $\mathbf{l}_{\text{sphere}}$ the distance traveled in the sphere by the molecule to \mathbf{F}_g . The time for a collision between molecule and nanoparticle is:

$$t_{\text{flight}} = t_{\text{md}} - t_{\text{sphere}}. \quad (6.68)$$

6.3.1 Ostwald ripening in a closed system

To test the kMC model for OR, the case of a closed simulation box is considered. This means that all molecules hitting z_{box} are reflected back into the simulation box. Thus the total number of Pt atoms is constant during the simulation, which is comparable to the assumption of the mean-field model for OR of no mass loss (see section 1.2.1). The difference is that with the kMC model the influence of the distance between the nanoparticles can be studied, as well as the case of very narrow nanoparticle size distributions or equally sized nanoparticles.

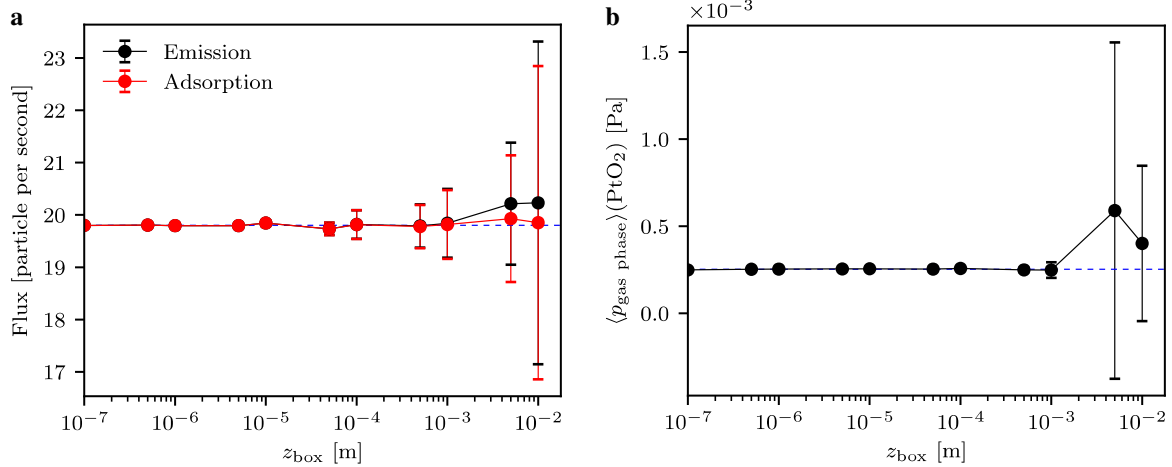


Figure 6.10: (a) Emitted (black) and adsorbed (red) particle flux from and to the nanoparticle with $N_{\text{Pt}} = 468$ ($d_{\text{eff}} = 3$ nm) at $T = 1000$ K and $p_{\text{O}_2} = 500$ Pa. The distance to the next periodic image of the nanoparticle is 10 nm. The blue dotted line is the rate expected from the mean-field OR model. (b) Mean pressure of $\text{PtO}_2(\text{g})$. The blue dotted line is the calculated equilibrium pressure p_{eq} (kMC parameters: $N_{\text{kMC}} = 2 \cdot 10^8$, $N_{\text{traj}} = 10$, $N_{\text{vp}} = 2000$, $N_{\text{int}} = 10^5$).

Figure 6.10a shows the emitted and adsorbed particle flux from and to a nanoparticle centered in the simulation cell, with an effective radius $d_{\text{eff}} = 3$ nm. The blue dotted line shows the flux which would be expected from eq. (6.61). With increasing simulation box size z_{box} , the standard deviation of the simulated fluxes increases, but the mean value is equal to the flux expected from eq. (6.61). In Fig. 6.10b the corresponding mean pressure of

$\text{PtO}_2(\text{g})$, averaged over the simulation time, is shown. In both plots deviations from the expected value can be only seen for $z_{\text{box}} \geq 5 \cdot 10^{-2}$ m, where the standard deviation is largest. Thus it is expected that with an increase in N_{traj} and N_{kMC} the simulation would converge to the expected value. To summarize, the size of the simulation box shows no difference between simulated data and eq. (6.61).

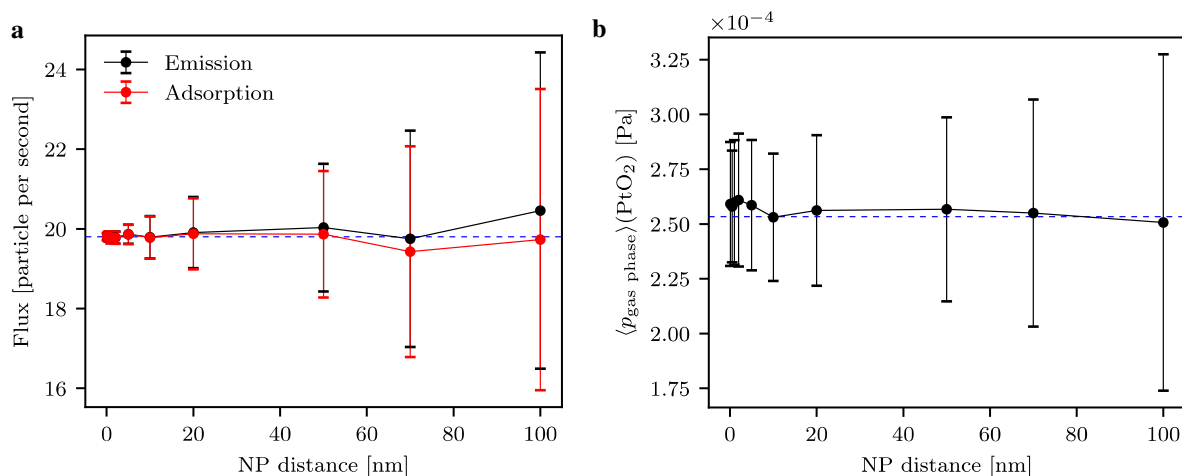


Figure 6.11: (a) Emitted (black) and adsorbed (red) particle flux from and to the nanoparticle with $N_{\text{Pt}} = 468$ ($d_{\text{eff}} = 3$ nm) at $T = 1000$ K, $p_{\text{O}_2} = 500$ Pa and $z_{\text{box}} = 10^{-3}$ m. The blue dotted line is the rate expected from the mean-field OR model. (b) Mean pressure of $\text{PtO}_2(\text{g})$. The blue dotted line is the calculated equilibrium pressure p_{eq} (kMC parameters: $N_{\text{kMC}} = 5 \cdot 10^8$, $N_{\text{traj}} = 50$, $N_{\text{vp}} = 2000$, $N_{\text{int}} = 10^5$).

In Figure 6.11a and 6.11b the effect of the distance of the nanoparticle to its next periodic image is studied at a constant box height, $z_{\text{box}} = 10^{-3}$ m for the emitted/adsorbed particle flux and mean pressure of $\text{PtO}_2(\text{g})$ respectively. With increasing nanoparticle distance the standard deviation increases, but all mean values are close to the results from eq. (6.61). Thus the distance, starting from 1 nm to 100 nm does not influence the measured properties. This is especially remarkable for very small distances < 5 nm, for which a direct transfer of PtO_2 between the nanoparticle and its images without scattering in the gas phase and thus an increase in the particle flux could be expected.

Figure 6.12a shows the time t_{anh} to annihilation of one of two nanoparticles in the simulation cell. t_{anh} is the time in which the first nanoparticle is evaporated. The size of nanoparticle $d_1 = 2$ nm is not varied, but the size of the second to simulate the case of nanoparticles similar in size. From the mean-field model (red line), it is expected that for $\Delta d \rightarrow 0$, $t_{\text{anh}} \rightarrow \infty$. That implies that nanoparticles exactly equal in size would show no change in particle size. The kMC simulation shows that also nanoparticles of equal size have a finite t_{anh} and that for $\Delta d < 0.05$ nm, t_{anh} is constant. Although the probability to emit a molecule into the gas phase is the same for equally sized nanoparticles, in the kMC model one of the nanoparticles is chosen at random. After the first scattering processes of the gas phase molecule, the origin of the molecule is oblivious and it is adsorbed by chance on either of the nanoparticles. In the beginning of the simulation this leads to only small variations in the nanoparticle sizes, but that is sufficient to drive the sintering of the nanoparticles. Even if particles could be experimentally produced being perfectly equal in size, fluctuations²³⁷ would lead to a small variation in particle size and drive sintering.

It can be seen in Fig. 6.12a that with decreasing Δd , the standard deviation increases. To demonstrate the convergence of the standard deviation with the number of trajectories, in Fig. 6.12b, the convergence of the standard deviation is shown with increasing number of trajectories. It can be seen that for equally sized nanoparticles and nanoparticles with $\Delta d = 0.1$ nm, the convergence is reached with 400 trajectories and that an increase in number of trajectories does not lead to a decrease of the standard deviation.

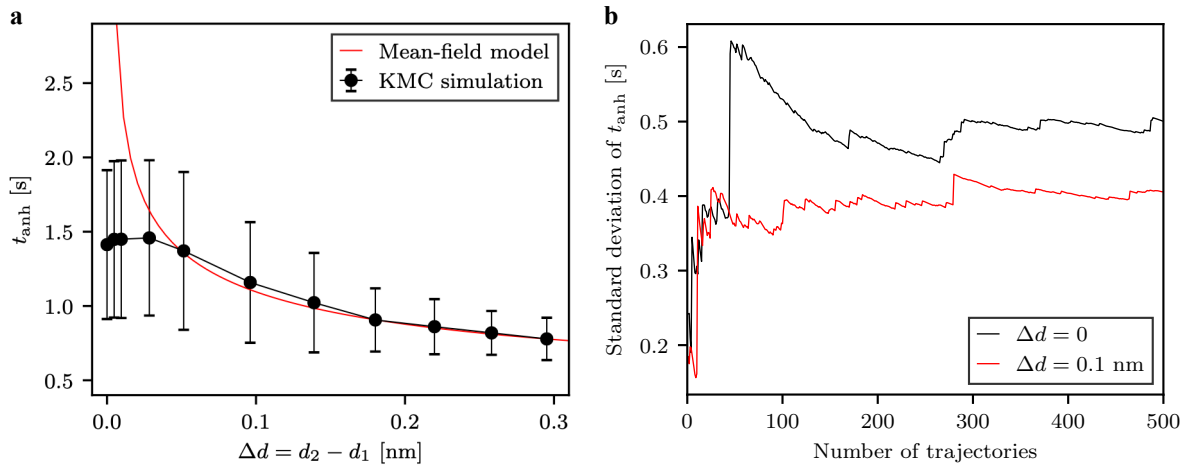


Figure 6.12: (a) Annihilation time t_{anh} to evaporate one of two nanoparticles with difference in diameter Δd , calculated with the kMC model (black line with circles, errorbars: standard deviation) and using the mean-field model²⁷. The size of one nanoparticle is kept constant to $d_1 = 2$ nm, $T = 1000$ K and $p_{\text{O}_2} = 500$ Pa. (b) Convergence of the standard deviation of the calculated t_{anh} with the number of trajectories for the examples of equal particles (black, $\Delta d = 0$) and different sized particles (red), $\Delta d = 0.1$ nm. (kMC parameters: $N_{\text{kMC}} = 2 \cdot 10^8$, $N_{\text{traj}} = 500$, $N_{\text{vp}} = 2000$, $N_{\text{int}} = 10^5$)

6.3.2 Conclusions

The gas phase kMC model was extended to simulate OR using the same assumptions as for the mean-field model. It was demonstrated that the size of the simulation box and the distance between the nanoparticles have no effect on the modeled particle flux and mean background pressure of $\text{PtO}_2(\text{g})$. For the limit of narrow PSDs it was shown that a finite time for sintering exists, which is not covered by the mean-field model. Thus the mean-field model is limited to nanoparticles with a difference in diameter of 0.05 nm. To go beyond the mean-field model, the effect of Platinum loss ought to be studied.

7 Final conclusions and outlook

In this thesis, density functional theory (DFT) was used to investigate the thermodynamic stability of pure nanoparticles and the influence of different supports on their stability. The kinetics of the sintering processes were studied for the example of Pt/quartz which is a model for exhaust-gas after-treatment catalysts.

To study the stability of pure nanoparticles, a simple model was described that is able to predict the stability of nanoparticles as a function of size and shape based on the coordination numbers of their surface atoms and lattice constant dependent $\gamma_{111}(a_0)$ and $\mu_{\text{bulk}}(a_0)$. Importantly, it was found that the energy of a surface termination can be directly calculated based on the corresponding coordination numbers of the surface atoms. The derived stability model was shown to be highly accurate and reproduced the results of DFT calculations with a mean absolute error of only 0.09 eV/atom for the symmetric and well-defined nanoparticles studied in this thesis. Importantly, this allows to estimate the thermodynamic stability of a whole set of transition metal particles of various sizes towards sintering. However, the thermodynamic stability of gas phase clusters is only one step in the direction to understand the complex behavior of different heterogeneous catalysts. The influence of different supports and adsorbates on the nanoparticle stability is an additional challenge.

To investigate the influence of different supports, a variety of metal/oxide interfaces were systematically studied using different supercells to minimize lattice mismatch. Scaling relations could be identified to analyze adhesion energies, where the adsorption energy of atomic oxygen on clean metal surfaces $E_{\text{ad}}(\text{O})$ serves as a descriptor. Variations between different oxides could be described by the different concentrations of interfacial oxygen atoms c_{O} . These concentrations can in many cases be easily extracted from the atomic structure of the clean oxide surfaces. A simple model was proposed that allows the prediction of adhesion energies for a given metal-oxide based on these two descriptors ($E_{\text{ad}}(\text{O})$, c_{O}). Consequently, properties that depend on the adhesion energy, such as particle shape or metal chemical potential are also accessible through this model.

The kinetics of sintering were investigated for the example of platinum on quartz through particle migration and coalescence with a kinetic Monte Carlo (kMC)-model employing diffusion constants obtained from first principles calculations. Generally, the extent of particle migration and coalescence is well-described through the diffusion constant, D , a function of both, temperature and particle size. As expected, the extent of sintering increased with increasing particle concentration. The effect that point defects have on sintering has also been studied extensively. Generally, more and stronger binding defects lead to less sintering. However, beyond a certain binding strength, stronger binding does not further decrease sintering. The binding strength necessary to completely trap a particle for a certain time could be estimated through the average escape time using a lattice hop model and the diffusion constant of the given particle.

The kMC model for particle migration and coalescence was combined with a mean-field model for gas phase Ostwald ripening of Pt via volatile $\text{PtO}_2(\text{g})$ which allowed to study both processes simultaneously. For experimentally relevant conditions ($p_{\text{O}_2} > 1$ mbar), it was found that ripening is more important than particle migration. If both, gas phase Ostwald ripening and particle migration and coalescence are relevant, their combined effect is usually smaller than the sum of the effects of the individual processes. This is likely due to the fact that only the smallest particles are mobile enough for particle migration. However, these particles are also the ones most readily annihilated through ripening.

This chapter is based on the conclusions in refs. 31,101,102,238.

To investigate the accuracy of the employed mean-field model for Ostwald ripening, a gas phase diffusion kMC model was developed. It could be shown that ideal gas properties, in particular the diffusion constant, could be simulated accurately using this developed kMC model. The model describes the collisions of an explicitly simulated molecule in a background gas. This approach could furthermore be used to simulate mass transport through the gas phase between surfaces. For model systems, it was found that solutions based on Fick's laws underestimate mass transport if the systems were on the nanometer scale. This could be explained by the long mean free path in the gas phase that leads to a sizable number of trajectories where particles were not scattered by the background gas. Such an effect can not be predicted by standard continuum models and it is expected that this is important in systems where gas phase diffusion occurs on the nanoscale. Finally, this kMC approach is applied to model gas phase mediated Ostwald ripening of Pt. It could be demonstrated that the mean-field model and the kMC model agree in the case of varying particle sizes but that for the limit of equally sized particles the mean-field model predicts no sintering whereas the kMC model predicts vaporization of the nanoparticles. With the kMC model it could be shown that the effect of nanoparticle distance up to 100 nm is negligible.

The investigated aspects of catalyst stability and deactivation are only small steps in the direction of a full understanding of these processes. A next step to investigate the shape of stable supported nanoparticles could be to use the developed stability model for metal nanoparticles to describe the size dependent stability of nanoparticles more accurately than with the commonly employed Gibbs-Thomson equation. Different supports can be taken into account based on the computed adhesion energies. Thus, the accuracy of models for the sintering kinetics can be improved and the simulations can be adapted to specific applications.

A remaining challenge is the limited accuracy of DFT, which limits the reliability of kinetic models based on DFT calculations. Industrial catalysts are often based on amorphous supports, for example SiO_2 or Al_2O_3 , of which the actual structure is not only unknown but may also contains defects. Additionally, catalysts can be functionalized using dopants, leading to a complex composition and surface structure. These complexities of real catalysts pose additional challenges for simulations that are typically based on idealized structures.

8 Bibliography

- [1] Atkins, P. W.; de Pala, J. *Physikalische Chemie*, 4th ed.; WILEY-VCH Verlag GmbH & Co. KGaA: Weinheim, 2006; p 839.
- [2] Thomas, J. M.; Thomas, W. J. *Principles and Practice of Heterogeneous Catalysis*; Wiley-VCH Verlag GmbH & Co.: Weinheim, 1997.
- [3] Cuenya, B. R. Synthesis and Catalytic Properties of Metal Nanoparticles: Size, Shape, Support, Composition and Oxidation State Effects. *Thin Solid Films* **2010**, *518*, 3127–3150.
- [4] Ryerson, T. B. et al. Observations of Ozone Formation in Power Plant Plumes and Implications for Ozone Control Strategies. *Science* **2001**, *292*, 719.
- [5] Lox, E. S. In *Handbook of Heterogeneous Catalysis*; G. Ertl, F. S., H. Knözinger, Weitkamp, J., Eds.; 2008; pp 2274–2345.
- [6] Deutschmann, O.; Grunwaldt, J.-D. Abgasnachbehandlung in Mobilen Systemen: Stand der Technik, Herausforderungen und Perspektiven. *Chemie Ingenieur Technik* **2013**, *85*, 595–617.
- [7] Bartholomew, C. H. Mechanisms of Catalyst Deactivation. *Appl. Catal., A* **2001**, *212*, 17–60.
- [8] Moulijn, J. A.; van Diepen, A. E.; Kapteijn, F. Catalyst Deactivation: Is It Predictable?: What To Do? *Appl. Catal., A* **2001**, *212*, 3–16.
- [9] Tollefson, J. Worth its Weight in Platinum. *Nature* **2007**, *450*, 334–335.
- [10] Farrauto, R. J. Low-Temperature Oxidation of Methane. *Science* **2012**, *337*, 659.
- [11] Argyle, M. D.; Bartholomew, C. H. Heterogeneous Catalyst Deactivation and Regeneration: A Review. *Catalysts* **2015**, *5*, 145–269.
- [12] European Environment Agency (EEA), *European Union emission inventory report 1990–2017*; 2019.
- [13] Mladenov, N. Ph.D. thesis, Universität Karlsruhe (TH), 2010.
- [14] Goodman, E. D.; Schwalbe, J. A.; Cargnello, M. Mechanistic Understanding and the Rational Design of Sinter-Resistant Heterogeneous Catalysts. *ACS Catal.* **2017**, *7*, 7156–7173.
- [15] Wulff, G. Z. Zur Frage der Geschwindigkeit des Wachstums und der Auflösung der Krystallflächen. *Krystallogr. Minera.* **1901**, *34*, 449–530.
- [16] Wagner, C. Theorie der Alterung von Niederschlägen durch Umlösen (Ostwald-Reifung). *Zeitschrift für Elektrochemie, Berichte der Bunsengesellschaft für physikalische Chemie* **1961**, *65*, 581–591.
- [17] Campbell, C. T.; Parker, S. C.; Starr, D. E. The Effect of Size-Dependent Nanoparticle Energetics on Catalyst Sintering. *Science* **2002**, *298*, 811–4.
- [18] Jak, M. J. J.; Konstapel, C.; van Kreuningen, A.; Verhoeven, J.; Frenken, J. W. M. Scanning Tunnelling Microscopy Study of the Growth of Small Palladium Particles on TiO₂(110). *Surf. Sci.* **2000**, *457*, 295–310.

- [19] Parker, S. C.; Campbell, C. T. Kinetic Model for Sintering of Supported Metal Particles with Improved Size-Dependent Energetics and Applications to Au on TiO₂(110). *Phys. Rev. B* **2007**, *75*, 035430.
- [20] Campbell, C. T.; Mao, Z. Chemical Potential of Metal Atoms in Supported Nanoparticles: Dependence upon Particle Size and Support. *ACS Catal.* **2017**, *7*, 8460–8466.
- [21] Hemmingson, S. L.; Campbell, C. T. Trends in Adhesion Energies of Metal Nanoparticles on Oxide Surfaces: Understanding Support Effects in Catalysis and Nanotechnology. *ACS Nano* **2017**, *11*, 1196–1203.
- [22] Lifshitz, I. M.; Slyozov, V. V. The Kinetics of Precipitation from Supersaturated Solid Solutions. *J. Phys. Chem. Solids* **1961**, *19*, 35–50.
- [23] Wynblatt, P.; Gjostein, N. Particle Growth in Model Supported Metal Catalysts? I. Theory. *Acta Metall.* **1976**, *24*, 1165–1174.
- [24] Wynblatt, P. Particle Growth in Model Supported Metal Catalysts? II. Comparison of Experiment with Theory. *Acta Metall.* **1976**, *24*, 1175–1182.
- [25] Rubel, M.; Pszonicka, M.; Ebel, M. F.; Jabłoński, A.; Palczewska, W. Oxygen Generated Platinum, Rhodium and Palladium Volatile Losses From Pure Metals and Their Alloys. *J. Less Common Met.* **1986**, *125*, 7–24.
- [26] Alcock, C. B.; Hooper, G. W.; Nyholm Ronald, S. Thermodynamics of the Gaseous Oxides of the Platinum-Group Metals. *P. Roy. Soc. Lond. A*
- [27] Plessow, P. N.; Abild-Pedersen, F. Sintering of Pt Nanoparticles via Volatile PtO₂: Simulation and Comparison with Experiments. *ACS Catal.* **2016**, *6*, 7098–7108.
- [28] Tabib Zadeh Adibi, P.; Zhdanov, V. P.; Langhammer, C.; Grönbeck, H. Transient Bimodal Particle Size Distributions during Pt Sintering on Alumina and Silica. *J. Phys. Chem. C* **2015**, *119*, 989–996.
- [29] Benavidez, A. D.; Kovarik, L.; Genc, A.; Agrawal, N.; Larsson, E. M.; Hansen, T. W.; Karim, A. M.; Datye, A. K. Environmental Transmission Electron Microscopy Study of the Origins of Anomalous Particle Size Distributions in Supported Metal Catalysts. *ACS Catal.* **2012**, *2*, 2349–2356.
- [30] Yang, W. C.; Zeman, M.; Ade, H.; Nemanich, R. J. Attractive Migration and Coalescence: A Significant Process in the Coarsening of TiSi₂ Islands on the Si(111) Surface. *Phys. Rev. Lett.* **2003**, *90*, 136102.
- [31] Dietze, E. M.; Plessow, P. N. Predicting the Strength of Metal–Support Interaction with Computational Descriptors for Adhesion Energies. *J. Phys. Chem. C* **2019**, *123*, 20443–20450.
- [32] Plessow, P. N.; Sánchez-Carrera, R. S.; Li, L.; Rieger, M.; Sauer, S.; Schaefer, A.; Abild-Pedersen, F. Modeling the Interface of Platinum and α -Quartz(001): Implications for Sintering. *J. Phys. Chem. C* **2016**, *120*, 10340–10350.
- [33] Zhdanov, V. P. Kinetics of Migration and Coalescence of Supported nm-Sized Metal Particles. *Surf. Rev. Lett.* **2008**, *15*, 217–220.
- [34] Challa, S. R.; Song, Y. J.; Shelnut, J. A.; Miller, J. E.; van Swol, F. Evolution of Dendritic Nanosheets Into Durable Holey Sheets: A Lattice Gas Simulation Study. *J. Porphyrins Phthalocyanines* **2011**, *15*, 449–458.
- [35] Jak, M. J. J.; Konstapel, C.; van Kreuningen, A.; Chrost, J.; Verhoeven, J.; Frenken, J. W. M. The Influence of Substrate Defects on the Growth Rate of Palladium Nanoparticles on a TiO₂(110) Surface. *Surf. Sci.* **2001**, *474*, 28–36.

- [36] Hu, C. H.; Chizallet, C.; Mager-Maury, C.; Corral-Valero, M.; Sautet, P.; Toulhoat, H.; Raybaud, P. Modulation of Catalyst Particle Structure upon Support Hydroxylation: Ab Initio Insights into Pd₁₃ and Pt₁₃/γ-A₂O₃. *J. Catal.* **2010**, *274*, 99–110.
- [37] Martin, A.; Biplab, S.; Olle, E.; Natalia, V. S. Small Gold Clusters on Graphene, Their Mobility and Clustering: A DFT Study. *J. Phys.: Condens. Matter* **2011**, *23*, 205301.
- [38] Rasmussen, D.; Janssens, T. V. W.; Temel, B.; Bligaard, T.; Hinnemann, B.; Helveg, S.; Sehested, J. The Energies of Formation and Mobilities of Cu Surface Species on Cu and ZnO in Methanol and Water Gas Shift Atmospheres Studied by DFT. *J. Catal.* **2012**, *293*, 205–214.
- [39] Wang, B.; Yoon, B.; König, M.; Fukamori, Y.; Esch, F.; Heiz, U.; Landman, U. Size-Selected Monodisperse Nanoclusters on Supported Graphene: Bonding, Isomerism and Mobility. *Nano Lett.* **2012**, *12*, 5907–5912.
- [40] Xu, L.; Henkelman, G.; Campbell, C. T.; Jónsson, H. Small Pd Clusters, up to the Tetramer At Least, Are Highly Mobile on the MgO(100) Surface. *Phys. Rev. Lett.* **2005**, *95*, 146103.
- [41] Xu, L.; Henkelman, G.; Campbell, C. T.; Jónsson, H. Pd diffusion on MgO(100): The Role of Defects and Small Cluster Mobility. *Surf. Sci.* **2006**, *600*, 1351–1362.
- [42] Abild-Pedersen, F.; Greeley, J.; Studt, F.; Rossmeisl, J.; Munter, T. R.; Moses, P. G.; Skulason, E.; Bligaard, T.; Nørskov, J. K. Scaling Properties of Adsorption Energies for Hydrogen-Containing Molecules on Transition-Metal Surfaces. *Phys. Rev. Lett.* **2007**, *99*, 016105.
- [43] Sutherland, W. LXXV. A Dynamical Theory of Diffusion for Non-Electrolytes and the Molecular Mass of Albumin. *Lond. Edinb. Dubl. Phil. Mag.* **1905**, *9*, 781–785.
- [44] von Smoluchowski, M. Zur kinetischen Theorie der Brownschen Molekularbewegung und der Suspensionen. *Annalen der Physik* **1906**, *326*, 756–780.
- [45] Morgenstern, K.; Rosenfeld, G.; Poelsema, B.; Comsa, G. Brownian Motion of Vacancy Islands on Ag(111). *Phys. Rev. Lett.* **1995**, *74*, 2058–2061.
- [46] Khare, S. V.; Bartelt, N. C.; Einstein, T. L. Diffusion of Monolayer Adatom and Vacancy Clusters: Langevin Analysis and Monte Carlo Simulations of their Brownian Motion. *Phys. Rev. Lett.* **1995**, *75*, 2148–2151.
- [47] Kashchiev, D. Kinetics of Thin Film Coalescence Due to Crystallite Surface Migration. *Surf. Sci.* **1976**, *55*, 477–493.
- [48] Kandel, D. Selection of the Scaling Solution in a Cluster Coalescence Model. *Phys. Rev. Lett.* **1997**, *79*, 4238–4241.
- [49] Li, L.; Plessow, P. N.; Rieger, M.; Sauer, S.; Sanchez-Carrera, R. S.; Schaefer, A.; Abild-Pedersen, F. Modeling the Migration of Platinum Nanoparticles on Surfaces Using a Kinetic Monte Carlo Approach. *J. Phys. Chem. C* **2017**, *121*, 4261–4269.
- [50] Lai, K. C.; Evans, J. W. Complex Oscillatory Decrease with Size in Diffusivity of 100-Epitaxially Supported 3D Fcc Metal Nanoclusters. *Nanoscale* **2019**, *11*, 17506–17516.
- [51] Simonsen, S. B.; Chorkendorff, I.; Dahl, S.; Skoglundh, M.; Sehested, J.; Helveg, S. Direct Observations of Oxygen-Induced Platinum Nanoparticle Ripening Studied by In Situ TEM. *J. Am. Chem. Soc.* **2010**, *132*, 7968–7975.

- [52] Challa, S. R.; Delariva, A. T.; Hansen, T. W.; Helveg, S.; Sehested, J.; Hansen, P. L.; Garzon, F.; Datye, A. K. Relating Rates of Catalyst Sintering to the Disappearance of Individual Nanoparticles During Ostwald Ripening. *J. Am. Chem. Soc.* **2011**, *133*, 20672–5.
- [53] Hansen, T. W.; DeLaRiva, A. T.; Challa, S. R.; Datye, A. K. Sintering of Catalytic Nanoparticles: Particle Migration or Ostwald Ripening? *Acc. Chem. Res.* **2013**, *46*, 1720–1730.
- [54] Chu, Y.; Ruckenstein, E. On the Sintering of Platinum on Alumina Model Catalyst. *J. Catal.* **1978**, *55*, 281–298.
- [55] Sushumna, I.; Ruckenstein, E. Events observed and evidence for crystallite migration in Pt/Al₂O₃ catalysts. *J. Catal.* **1988**, *109*, 433–462.
- [56] Ouyang, R.; Liu, J. X.; Li, W. X. Atomistic Theory of Ostwald Ripening and Disintegration of Supported Metal Particles Under Reaction Conditions. *J. Am. Chem. Soc.* **2013**, *135*, 1760–71.
- [57] Wettergren, K.; Schweinberger, F. F.; Deiana, D.; Ridge, C. J.; Crampton, A. S.; Rotzer, M. D.; Hansen, T. W.; Zhdanov, V. P.; Heiz, U.; Langhammer, C. High Sintering Resistance of Size-Selected Platinum Cluster Catalysts by Suppressed Ostwald Ripening. *Nano Lett.* **2014**, *14*, 5803–9.
- [58] Simonsen, S. B.; Chorkendorff, I.; Dahl, S.; Skoglundh, M.; Sehested, J.; Helveg, S. Ostwald Ripening in a Pt/SiO₂ Model Catalyst Studied by in Situ TEM. *J. Catal.* **2011**, *281*, 147–155.
- [59] Rickard, J. M.; Genovese, L.; Moata, A.; Nitsche, S. Redispersion of Platinum on Pt/Al₂O₃ Model Catalyst in Oxygen Studied by Transmission Electron Microscopy. *J. Catal.* **1990**, *121*, 141–152.
- [60] Baker, R. T. K.; Thomas, C.; Thomas, R. B. Continuous Observation of the Particle Size Behavior of Platinum on Alumina. *J. Catal.* **1975**, *38*, 510–513.
- [61] Smith, D. J.; White, D.; Baird, T.; Fryer, J. R. The Characterisation of a Model Platinum/Alumina Catalyst by High-Resolution Electron Microscopy. *J. Catal.* **1983**, *81*, 107–118.
- [62] Hofmann, G.; Rochet, A.; Ogel, E.; Casapu, M.; Ritter, S.; Ogurreck, M.; Grunwaldt, J.-D. Aging of a Pt/Al₂O₃ Exhaust Gas Catalyst Monitored by Quasi in Situ X-Ray Micro Computed Tomography. *RSC Adv.* **2015**, *5*, 6893–6905.
- [63] Harris, P. J. F.; Boyes, E. D.; Cairns, J. A. The Sintering of an Alumina-Supported Platinum Catalyst Studied by Transmission Electron-Microscopy. *J. Catal.* **1983**, *82*, 127–146.
- [64] Garetto, T. F.; Borgna, A.; Monzon, A. Modelling of Sintering Kinetics of Naphtha-Reforming Pt/Al₂O₃-Cl Catalysts. *J. Chem. Soc., Faraday Trans.* **1996**, *92*, 2637–2640.
- [65] Porsgaard, S.; Merte, L. R.; Ono, L. K.; Behafarid, F.; Matos, J.; Helveg, S.; Salmeron, M.; Roldan Cuenya, B.; Besenbacher, F. Stability of Platinum Nanoparticles Supported on SiO₂/Si(111): A High-Pressure X-Ray Photoelectron Spectroscopy Study. *ACS Nano* **2012**, *6*, 10743–9.
- [66] Tabib Zadeh Adibi, P.; Mazzotta, F.; Antosiewicz, T. J.; Skoglundh, M.; Grönbeck, H.; Langhammer, C. In Situ Plasmonic Sensing of Platinum Model Catalyst Sintering on Different Oxide Supports and in O₂ and NO₂ Atmospheres with Different Concentrations. *ACS Catal.* **2015**, *5*, 426–432.
- [67] Larsson, E. M.; Millet, J.; Gustafsson, S.; Skoglundh, M.; Zhdanov, V. P.; Langhammer, C. Real Time Indirect Nanoplasmonic in Situ Spectroscopy of Catalyst Nanoparticle Sintering. *ACS Catal.* **2012**, *2*, 238–245.

- [68] Behafarid, F.; Cuenya, B. R. Towards the Understanding of Sintering Phenomena at the Nanoscale: Geometric and Environmental Effects. *Top. Catal.* **2013**, *56*, 1542–1559.
- [69] Goodman, E. D.; Johnston-Peck, A. C.; Dietze, E. M.; Wrasman, C. J.; Hoffman, A. S.; Abild-Pedersen, F.; Bare, S. R.; Plessow, P. N.; Carnello, M. Catalyst Deactivation via Decomposition Into Single Atoms and the Role of Metal Loading. *Nat. Catal.* **2019**, *2*, 748–755.
- [70] Xiong, H. F.; Peterson, E.; Qi, G. S.; Datye, A. K. Trapping Mobile Pt Species by PdO in Diesel Oxidation Catalysts: Smaller is Better. *Catal. Today* **2016**, *272*, 80–86.
- [71] Tait, S. L.; Ngo, L. T.; Yu, Q.; Fain, J., S. C.; Campbell, C. T. Growth and Sintering of Pd Clusters on α -Al₂O₃(0001). *J. Chem. Phys.* **2005**, *122*, 064712.
- [72] Penner, S.; Bera, P.; Pedersen, S.; Ngo, L. T.; Harris, J. J.; Campbell, C. T. Interactions of O₂ with Pd Nanoparticles on α -Al₂O₃(0001) at Low and High O₂ Pressures. *J. Phys. Chem. B* **2006**, *110*, 24577–84.
- [73] Xu, Q.; Kharas, K. C.; Croley, B. J.; Datye, A. K. The Sintering of Supported Pd Automotive Catalysts. *ChemCatChem* **2011**, *3*, 1004–1014.
- [74] Zhdanov, V. P.; Schweinberger, F. F.; Heiz, U.; Langhammer, C. Ostwald Ripening of Supported Pt Nanoclusters with Initial Size-Selected Distributions. *Chem. Phys. Lett.* **2015**, *631*, 21–25.
- [75] Zhdanov, V. P.; Kasemo, B. Nontraditional Models of Ostwald Ripening on Solid Surfaces: From Physics to Biology. *Surf. Sci.* **1999**, *437*, 307–316.
- [76] Datye, A. K.; Xu, Q.; Kharas, K. C.; McCarty, J. M. Particle Size Distributions in Heterogeneous Catalysts: What Do They Tell us About the Sintering Mechanism? *Catal. Today* **2006**, *111*, 59–67.
- [77] Cao, A.; Vesper, G. Exceptional High-Temperature Stability Through Distillation-Like Self-Stabilization in Bimetallic Nanoparticles. *Nat. Mater.* **2010**, *9*, 75–81.
- [78] Ha, M.-A.; Dadras, J.; Alexandrova, A. Rutile-Deposited Pt–Pd clusters: A Hypothesis Regarding the Stability at 50/50 Ratio. *ACS Catal.* **2014**, *4*, 3570–3580.
- [79] Carrillo, C. et al. Regenerative Trapping: How Pd Improves the Durability of Pt Diesel Oxidation Catalysts. *Appl. Catal., B* **2017**, *218*, 581–590.
- [80] Goodman, E. D. et al. Uniform Pt/Pd Bimetallic Nanocrystals Demonstrate Platinum Effect on Palladium Methane Combustion Activity and Stability. *ACS Catal.* **2017**, *7*, 4372–4380.
- [81] Linares, N.; Serrano, E.; Rico, M.; Mariana Balu, A.; Losada, E.; Luque, R.; García-Martínez, J. Incorporation of Chemical Functionalities in the Framework of Mesoporous Silica. *Chem. Commun.* **2011**, *47*, 9024–9035.
- [82] van den Berg, R.; Parmentier, T. E.; Elkjær, C. F.; Gommès, C. J.; Sehested, J.; Helveg, S.; de Jongh, P. E.; de Jong, K. P. Support Functionalization To Retard Ostwald Ripening in Copper Methanol Synthesis Catalysts. *ACS Catal.* **2015**, *5*, 4439–4448.
- [83] Kou, R. et al. Enhanced Activity and Stability of Pt Catalysts on Functionalized Graphene Sheets For Electrocatalytic Oxygen Reduction. *Electrochem. Commun.* **2009**, *11*, 954–957.
- [84] Bruix, A.; Rodriguez, J. A.; Ramirez, P. J.; Senanayake, S. D.; Evans, J.; Park, J. B.; Stacchiola, D.; Liu, P.; Hrbek, J.; Illas, F. A New Type of Strong Metal-Support Interaction and the Production of H₂ through the Transformation of Water on Pt/CeO₂(111) and Pt/CeO_(x)/TiO₂(110) Catalysts. *J. Am. Chem. Soc.* **2012**, *134*, 8968–74.

- [85] Campbell, C. T. Catalyst-Support Interactions: Electronic Perturbations. *Nat. Chem.* **2012**, *4*, 597–8.
- [86] Laursen, S.; Linic, S. Oxidation Catalysis by Oxide-Supported Au Nanostructures: the Role of Supports and the Effect of External Conditions. *Phys. Rev. Lett.* **2006**, *97*, 026101.
- [87] Green, I. X.; Tang, W.; Neurock, M.; Yates, J., J. T. Spectroscopic Observation of Dual Catalytic Sites During Oxidation of CO on a Au/TiO₂ Catalyst. *Science* **2011**, *333*, 736–9.
- [88] Jones, J. et al. Thermally Stable Single-Atom Platinum-on-Ceria Catalysts via Atom Trapping. *Science* **2016**, *353*, 150–4.
- [89] Rodriguez, J. A.; Liu, P.; Hrbek, J.; Evans, J.; Pérez, M. Water Gas Shift Reaction on Cu and Au Nanoparticles Supported on CeO₂(111) and ZnO(0001): Intrinsic Activity and Importance of Support Interactions. *Angew. Chem. Int. Ed.* **2007**, *46*, 1329–1332.
- [90] Nelson, R. C.; Baek, B.; Ruiz, P.; Goundie, B.; Brooks, A.; Wheeler, M. C.; Frederick, B. G.; Grabow, L. C.; Austin, R. N. Experimental and Theoretical Insights into the Hydrogen-Efficient Direct Hydrodeoxygenation Mechanism of Phenol over Ru/TiO₂. *ACS Catal.* **2015**, *5*, 6509–6523.
- [91] Kudernatsch, W.; Peng, G.; Zeuthen, H.; Bai, Y.; Merte, L. R.; Lammich, L.; Besenbacher, F.; Mavrikakis, M.; Wendt, S. Direct Visualization of Catalytically Active Sites at the FeO-Pt(111) Interface. *ACS Nano* **2015**, *9*, 7804–14.
- [92] Siegel, D. J.; Hector, L. G.; Adams, J. B. Ab Initio Study of Al-Ceramic Interfacial Adhesion. *Phys. Rev. B* **2003**, *67*.
- [93] Cheng, L. et al. Reaction Mechanism for Direct Propylene Epoxidation by Alumina-Supported Silver Aggregates: The Role of the Particle/Support Interface. *ACS Catal.* **2013**, *4*, 32–39.
- [94] Saavedra, J.; Doan, H. A.; Pursell, C. J.; Grabow, L. C.; Chandler, B. D. The Critical Role of Water at the Gold-Titania Interface in Catalytic CO Oxidation. *Science* **2014**, *345*, 1599–602.
- [95] Tauster, S. J.; Fung, S. C.; Baker, R. T.; Horsley, J. A. Strong Interactions in Supported-Metal Catalysts. *Science* **1981**, *211*, 1121–5.
- [96] Tauster, S. J. Strong Metal-Support Interactions. *Acc. Chem. Res.* **1987**, *20*, 389–394.
- [97] Tauster, S. J.; Fung, S. C.; Garten, R. L. Strong Metal-Support Interactions. Group 8 Noble Metals Supported on Titanium Dioxide. *J. Am. Chem. Soc.* **1978**, *100*, 170–175.
- [98] Lee, J. et al. Stabilizing Cobalt Catalysts for Aqueous-Phase Reactions by Strong Metal-Support Interaction. *J. Catal.* **2015**, *330*, 19–27.
- [99] Farmer, J. A.; Campbell, C. T. Ceria Maintains Smaller Metal Catalyst Particles by Strong Metal-Support Bonding. *Science* **2010**, *329*, 933–6.
- [100] Campbell, C. T. The Energetics of Supported Metal Nanoparticles: Relationships to Sintering Rates and Catalytic Activity. *Acc. Chem. Res.* **2013**, *46*, 1712–9.
- [101] Dietze, E. M.; Plessow, P. N. Kinetic Monte Carlo Model for Gas Phase Diffusion in Nanoscopic Systems. *J. Phys. Chem. C* **2018**, *122*, 11524–11531.
- [102] Dietze, E. M.; Abild-Pedersen, F.; Plessow, P. N. Comparison of Sintering by Particle Migration and Ripening through First-Principles-Based Simulations. *J. Phys. Chem. C* **2018**, *122*, 26563–26569.

- [103] Hinnemann, B.; Carter, E. A. Adsorption of Al, O, Hf, Y, Pt, and S Atoms on α -Al₂O₃(0001). *J. Phys. Chem. C* **2007**, *111*, 7105–7126.
- [104] Milas, I.; Hinnemann, B.; Carter, E. A. Diffusion of Al, O, Pt, Hf, and Y Atoms on α -Al₂O₃(0001): Implications for the Role of Alloying Elements in Thermal Barrier Coatings. *J. Mater. Chem.* **2011**, *21*, 1447–1456.
- [105] Iddir, H.; Ögüt, S.; Browning, N. D.; Disko, M. M. Adsorption and Diffusion of Pt and Au on the Stoichiometric and Reduced TiO₂ Rutile (110) Surfaces. *Phys. Rev. B* **2005**, *72*.
- [106] Aaron Deskins, N.; Mei, D.; Dupuis, M. Adsorption and Diffusion of a Single Pt Atom on γ -Al₂O₃ Surfaces. *Surf. Sci.* **2009**, *603*, 2793–2807.
- [107] Prieto, G.; Zežević, J.; Friedrich, H.; de Jong, K. P.; de Jongh, P. E. Towards Stable Catalysts by Controlling Collective Properties of Supported Metal Nanoparticles. *Nat. Mater.* **2012**, *12*, 34.
- [108] Liu, J.; Ji, Q.; Imai, T.; Ariga, K.; Abe, H. Sintering-Resistant Nanoparticles in Wide-Mouthed Compartments for Sustained Catalytic Performance. *Sci. Rep.* **2017**, *7*, 41773.
- [109] De Rogatis, L.; Cargnello, M.; Gombac, V.; Lorenzut, B.; Montini, T.; Fornasiero, P. Embedded Phases: A Way to Active and Stable Catalysts. *ChemSusChem* **2010**, *3*, 24–42.
- [110] Lu, J.; Fu, B.; Kung, M. C.; Xiao, G.; Elam, J. W.; Kung, H. H.; Stair, P. C. Coking- and Sintering-Resistant Palladium Catalysts Achieved Through Atomic Layer Deposition. *Science* **2012**, *335*, 1205.
- [111] Biener, M. M.; Biener, J.; Wichmann, A.; Wittstock, A.; Baumann, T. F.; Bäumer, M.; Hamza, A. V. ALD Functionalized Nanoporous Gold: Thermal Stability, Mechanical Properties, and Catalytic Activity. *Nano Lett.* **2011**, *11*, 3085–3090.
- [112] Feng, H.; Lu, J.; Stair, P. C.; Elam, J. W. Alumina Over-Coating on Pd Nanoparticle Catalysts by Atomic Layer Deposition: Enhanced Stability and Reactivity. *Catal. Lett.* **2011**, *141*, 512–517.
- [113] Henkelman, G.; Uberuaga, B. P.; Jónsson, H. A Climbing Image Nudged Elastic Band Method for Finding Saddle Points and Minimum Energy Paths. *J. Chem. Phys.* **2000**, *113*, 9901–9904.
- [114] Henkelman, G.; Jónsson, H. A Dimer Method for Finding Saddle Points on High Dimensional Potential Surfaces Using Only First Derivatives. *J. Chem. Phys.* **1999**, *111*, 7010–7022.
- [115] Heyden, A.; Bell, A. T.; Keil, F. J. Efficient Methods for Finding Transition States in Chemical Reactions: Comparison of Improved Dimer Method and Partitioned Rational Function Optimization Method. *J. Chem. Phys.* **2005**, *123*, 224101.
- [116] Born, M.; Oppenheimer, R. Zur Quantentheorie der Molekeln. *Annalen der Physik* **1927**, *389*, 457–484.
- [117] Hohenberg, P.; Kohn, W. Inhomogeneous Electron Gas. *Phys. Rev.* **1964**, *136*, B864–B871.
- [118] Kohn, W.; Sham, L. J. Self-Consistent Equations Including Exchange and Correlation Effects. *Phys. Rev.* **1965**, *140*, A1133–A1138.
- [119] Carr, W. J. Energy, Specific Heat, and Magnetic Properties of the Low-Density Electron Gas. *Phys. Rev.* **1961**, *122*, 1437–1446.
- [120] Carr, W. J.; Maradudin, A. A. Ground-State Energy of a High-Density Electron Gas. *Phys. Rev.* **1964**, *133*, A371–A374.

- [121] Barth, U. v.; Hedin, L. A Local Exchange-Correlation Potential for the Spin Polarized Case. *J. Phys. C: Solid State Phys.* **1972**, *5*, 1629–1642.
- [122] Perdew, J. P.; Zunger, A. Self-Interaction Correction to Density-Functional Approximations for Many-Electron Systems. *Phys. Rev. B* **1981**, *23*, 5048–5079.
- [123] Vosko, S. H.; Wilk, L.; Nusair, M. Accurate Spin-Dependent Electron Liquid Correlation Energies for Local Spin Density Calculations: A Critical Analysis. *Can. J. Phys.* **1980**, *58*, 1200–1211.
- [124] Becke, A. D. Density-Functional Exchange-Energy Approximation with Correct Asymptotic Behavior. *Phys. Rev. A* **1988**, *38*, 3098–3100.
- [125] Lee, C.; Yang, W.; Parr, R. G. Development of the Colle-Salvetti Correlation-Energy Formula Into a Functional of the Electron Density. *Phys. Rev. B* **1988**, *37*, 785–789.
- [126] Perdew, J. P.; Burke, K.; Ernzerhof, M. Generalized Gradient Approximation Made Simple. *Phys. Rev. Lett.* **1997**, *78*, 1396–1396.
- [127] Perdew, J. P.; Ruzsinszky, A.; Csonka, G. b. I.; Vydrov, O. A.; Scuseria, G. E.; Constantin, L. A.; Zhou, X.; Burke, K. Restoring the Density-Gradient Expansion for Exchange in Solids and Surfaces. *Phys. Rev. Lett.* **2008**, *100*, 136406.
- [128] Perdew, J. P.; Ruzsinszky, A.; Csonka, G. I.; Vydrov, O. A.; Scuseria, G. E.; Constantin, L. A.; Zhou, X.; Burke, K. Erratum: Restoring the Density-Gradient Expansion for Exchange in Solids and Surfaces [Phys. Rev. Lett.100, 136406 (2008)]. *Phys. Rev. Lett.* **2009**, *102*, 039902.
- [129] Tao, J.; Perdew, J. P.; Staroverov, V. N.; Scuseria, G. E. Climbing the Density Functional Ladder: Nonempirical Meta-Generalized Gradient Approximation Designed for Molecules and Solids. *Phys. Rev. Lett.* **2003**, *91*, 146401.
- [130] Becke, A. D. A New Mixing of Hartree-Fock and Local Density Functional Theories. *J. Chem. Phys.* **1993**, *98*, 1372–1377.
- [131] Stephens, P. J.; Devlin, F. J.; Chabalowski, C. F.; Frisch, M. J. Ab Initio Calculation of Vibrational Absorption and Circular Dichroism Spectra Using Density Functional Force Fields. *J. Phys. Chem.* **1994**, *98*, 11623–11627.
- [132] Hertwig, R. H.; Koch, W. On the Parameterization of the Local Correlation Functional. What is Becke-3-LYP? *Chem. Phys. Lett.* **1997**, *268*, 345–351.
- [133] Ernzerhof, M.; Scuseria, G. E. Assessment of the Perdew-Burke-Ernzerhof Exchange-Correlation Functional. *J. Chem. Phys.* **1999**, *110*, 5029–5036.
- [134] Wellendorff, J.; Lundgaard, K. T.; Mogelhoff, A.; Petzold, V.; Landis, D. D.; Nørskov, J. K.; Bligaard, T.; Jacobsen, K. W. Density Functionals for Surface Science: Exchange-Correlation Model Development with Bayesian Error Estimation. *Phys. Rev. B* **2012**, *85*, 235149.
- [135] Israelachvili, J. N. *Intermolecular and surface forces*; Academic press, 2015.
- [136] Tsuneda, T. *Density Functional Theory in Quantum Chemistry*; Springer Japan: Tokyo, 2014.
- [137] Jensen, F. *Introduction to computational chemistry*, 2nd ed.; John Wiley & Sons Ltd: Chichester, England, 2007.

- [138] Williams, H. L.; Chabalowski, C. F. Using Kohn-Sham Orbitals in Symmetry-Adapted Perturbation Theory to Investigate Intermolecular Interactions. *J. Phys. Chem. A* **2001**, *105*, 646–659.
- [139] Andersson, Y.; Langreth, D. C.; Lundqvist, B. I. Van der Waals Interactions in Density-Functional Theory. *Phys. Rev. Lett.* **1996**, *76*, 102–105.
- [140] Vydrov, O. A.; Van Voorhis, T. Nonlocal Van der Waals Density Functional Made Simple. *Phys. Rev. Lett.* **2009**, *103*, 063004.
- [141] Grimme, S. Accurate Description of Van Der Waals Complexes by Density Functional Theory Including Empirical Corrections. *J. Comput. Chem.* **2004**, *25*, 1463–1473.
- [142] Grimme, S. Semiempirical GGA-Type Density Functional Constructed with a Long-Range Dispersion Correction. *J. Comput. Chem.* **2006**, *27*, 1787–1799.
- [143] Grimme, S.; Antony, J.; Ehrlich, S.; Krieg, H. A Consistent and Accurate Ab Initio Parametrization of Density Functional Dispersion Correction (DFT-D) for the 94 Elements H-Pu. *J. Chem. Phys.* **2010**, *132*, 154104.
- [144] Runge, E.; Gross, E. K. U. Density-Functional Theory for Time-Dependent Systems. *Phys. Rev. Lett.* **1984**, *52*, 997–1000.
- [145] Chai, J.-D.; Head-Gordon, M. Long-Range Corrected Hybrid Density Functionals with Damped Atom–Atom Dispersion Corrections. *Phys. Chem. Chem. Phys.* **2008**, *10*, 6615–6620.
- [146] Becke, A. D.; Johnson, E. R. A Density-Functional Model of the Dispersion Interaction. *J. Chem. Phys.* **2005**, *123*, 154101.
- [147] Becke, A. D.; Johnson, E. R. Exchange-Hole Dipole Moment and the Dispersion Interaction: High-Order Dispersion Coefficients. *J. Chem. Phys.* **2006**, *124*, 014104.
- [148] Grimme, S.; Ehrlich, S.; Goerigk, L. Effect of the Damping Function in Dispersion Corrected Density Functional Theory. *J. Comput. Chem.* **2011**, *32*, 1456–1465.
- [149] Slater, J. C. Atomic Shielding Constants. *Phys. Rev.* **1930**, *36*, 57–64.
- [150] Boys, S. Integrals Over Primitive Gaussians. *Proc. R. Soc. London. Ser. A* **1950**, *200*, 532–540.
- [151] Bloch, F. Über die Quantenmechanik der Elektronen in Kristallgittern. *Zeitschrift für Physik* **1929**, *52*, 555–600.
- [152] Blöchl, P. E. Projector Augmented-Wave Method. *Phys. Rev. B* **1994**, *50*, 17953–17979.
- [153] Kresse, G.; Joubert, D. From Ultrasoft Pseudopotentials to the Projector Augmented-Wave Method. *Phys. Rev. B* **1999**, *59*, 1758–1775.
- [154] Van Kampen, N. G. *Stochastic Processes in Physics and Chemistry*; Elsevier, 1992; Vol. 1.
- [155] Schwabl, F. *Statistische Mechanik*; Springer, 2006; pp 417–444.
- [156] Reuter, K. In *First-Principles Kinetic Monte Carlo Simulations for Heterogeneous Catalysis: Concepts, Status, and Frontiers. In Modeling and Simulation of Heterogeneous Catalytic Reactions*; Deutschmann, O., Ed.; 2011.
- [157] Mitrani, I.; Mitrani, I. *Simulation Techniques for Discrete Event Systems*; CUP Archive, 1982; Vol. 14.

- [158] Jansen, A. P. J. *An Introduction to Kinetic Monte Carlo Simulations of Surface Reactions*; Springer Berlin Heidelberg: Berlin, Heidelberg, 2012; pp 37–71.
- [159] Gandhi, H. S.; Graham, G. W.; McCabe, R. W. Automotive Exhaust Catalysis. *J. Catal.* **2003**, *216*, 433–442.
- [160] Bartholomew, C.; Farrauto, R. *Fundamentals of Industrial Catalytic Processes*, 2nd ed.; Wiley: Hoboken, NJ, USA, 2006.
- [161] Verga, L. G.; Aarons, J.; Sarwar, M.; Thompsett, D.; Russell, A. E.; Skylaris, C. K. DFT Calculation of Oxygen Adsorption on Platinum Nanoparticles: Coverage and Size Effects. *Faraday Discuss.* **2018**, *208*, 497–522.
- [162] Simonsen, S. B.; Chorkendorff, I.; Dahl, S.; Skoglundh, M.; Meinander, K.; Jensen, T. N.; Lauritsen, J. V.; Helveg, S. Effect of Particle Morphology on the Ripening of Supported Pt Nanoparticles. *J. Phys. Chem. C* **2012**, *116*, 5646–5653.
- [163] Mostafa, S.; Behafarid, F.; Croy, J. R.; Ono, L. K.; Li, L.; Yang, J. C.; Frenkel, A. I.; Cuenya, B. R. Shape-Dependent Catalytic Properties of Pt Nanoparticles. *J. Am. Chem. Soc.* **2010**, *132*, 15714–9.
- [164] Barnard, A. S.; Zapol, P. A Model for the Phase Stability of Arbitrary Nanoparticles as a Function of Size and Shape. *J. Chem. Phys.* **2004**, *121*, 4276–4283.
- [165] Barnard, A. S. A Thermodynamic Model for the Shape and Stability of Twinned Nanostructures. *J. Phys. Chem. B* **2006**, *110*, 24498–24504.
- [166] Roling, L. T.; Li, L.; Abild-Pedersen, F. Configurational Energies of Nanoparticles Based on Metal-Metal Coordination. *J. Phys. Chem. C* **2017**, *121*, 23002–23010.
- [167] Roling, L. T.; Choksi, T. S.; Abild-Pedersen, F. A Coordination-Based Model for Transition Metal Alloy Nanoparticles. *Nanoscale* **2019**, *11*, 4438–4452.
- [168] Kresse, G.; Furthmüller, J. Efficient Iterative Schemes for Ab Initio Total-Energy Calculations using a Plane-Wave Basis Set. *Phys. Rev. B* **1996**, *54*, 11169–11186.
- [169] Kresse, G.; Furthmüller, J. Efficiency of Ab-Initio Total Energy Calculations for Metals and Semiconductors Using a Plane-Wave Basis Set. *Comput. Mater. Sci.* **1996**, *6*, 15–50.
- [170] Kresse, G.; Hafner, J. Ab Initio Molecular Dynamics for Liquid Metals. *Phys. Rev. B* **1993**, *47*, 558–561.
- [171] Kresse, G.; Hafner, J. Ab Initio Molecular-Dynamics Simulation of the Liquid-Metal-Amorphous-Semiconductor Transition in Germanium. *Phys. Rev. B* **1994**, *49*, 14251–14269.
- [172] Tyson, W. R.; Miller, W. A. Surface Free Energies of Solid Metals: Estimation from Liquid Surface Tension Measurements. *Surf. Sci.* **1977**, *62*, 267–276.
- [173] Schimka, L.; Harl, J.; Stroppa, A.; Grüneis, A.; Marsman, M.; Mittendorfer, F.; Kresse, G. Accurate Surface and Adsorption Energies From Many-Body Perturbation Theory. *Nat. Mater.* **2010**, *9*, 741–4.
- [174] Abild-Pedersen, F.; Andersson, M. P. CO Adsorption Energies on Metals with Correction for High Coordination Adsorption Sites - A Density Functional Study. *Surf. Sci.* **2007**, *601*, 1747–1753.
- [175] Singh, R.; Kroll, P. Structural, Electronic, and Magnetic Properties of 13-, 55-, and 147-Atom Clusters of Fe, Co, and Ni: A Spin-Polarized Density Functional Study. *Phys. Rev. B* **2008**, *78*, 245404.

- [176] Ebert, H.; Battochetti, M.; Gross, E. K. U. Current Density Functional Theory of Spontaneously Magnetised Solids. *Europhys. Lett.* **1997**, *40*, 545–550.
- [177] Marcus, P. M.; Moruzzi, V. L. Equilibrium Properties of the Cubic Phases of Cobalt. *Solid State Commun.* **1985**, *55*, 971–975.
- [178] Hjorth Larsen, A. et al. The Atomic Simulation Environment—a Python Library for Working with Atoms. *J. Phys. Condens. Matter.* **2017**, *29*, 273002.
- [179] Kittel, C. *Introduction to Solid State Physics*, 7th ed.; Wiley: Hoboken, NJ, USA, 1996.
- [180] Jørgensen, M.; Grönbeck, H. Scaling Relations and Kinetic Monte Carlo Simulations To Bridge the Materials Gap in Heterogeneous Catalysis. *ACS Catal.* **2017**, *7*, 5054–5061.
- [181] Nava, P.; Sierka, M.; Ahlrichs, R. Density Functional Study of Palladium Clusters. *Phys. Chem. Chem. Phys.* **2003**, *5*, 3372–3381.
- [182] Viñes, F.; Illas, F.; Neyman, K. M. Density Functional Calculations of Pd Nanoparticles Using a Plane-Wave Method. *J. Phys. Chem. A* **2008**, *112*, 8911–8915.
- [183] Koitz, R.; Soini, T. M.; Genest, A.; Trickey, S. B.; Rösch, N. Scalable Properties of Metal Clusters: A Comparative Study of Modern Exchange–Correlation Functionals. *J. Chem. Phys.* **2012**, *137*, 034102.
- [184] Soini, T. M.; Ma, X.; Üzengi Aktürk, O.; Suthirakun, S.; Genest, A.; Rösch, N. Extending the Cluster Scaling Technique to Ruthenium Clusters with hcp Structures. *Surf. Sci.* **2016**, *643*, 156–163.
- [185] Häberlen, O. D.; Chung, S.-C.; Stener, M.; Rösch, N. From Clusters to Bulk: A Relativistic Density Functional Investigation on a Series of Gold Clusters Au_n, n=6,...,147. *J. Chem. Phys.* **1997**, *106*.
- [186] Köhn, A.; Weigend, F.; Ahlrichs, R. Theoretical Study on Clusters of Magnesium. *Phys. Chem. Chem. Phys.* **2001**, *3*, 711–719.
- [187] Weigend, F.; Ahlrichs, R. Quantum Chemical Treatments of Metal Clusters. *Phil. Trans. R. Soc. A* **2010**, *368*, 1245–1263.
- [188] Tsuneda, T. Theoretical Investigations on Geometrical and Electronic Structures of Silver Clusters. *J. Comput. Chem.* **2019**, *40*, 206–211.
- [189] Nanba, Y.; Ishimoto, T.; Koyama, M. Structural Stability of Ruthenium Nanoparticles: A Density Functional Theory Study. *J. Phys. Chem. C* **2017**, *121*, 27445–27452.
- [190] Nolte, P.; Stierle, A.; Jin-Phillipp, N. Y.; Kasper, N.; Schulli, T. U.; Dosch, H. Shape Changes of Supported Rh Nanoparticles During Oxidation and Reduction Cycles. *Science* **2008**, *321*, 1654–8.
- [191] Hansen, K. H.; Worren, T.; Stempel, S.; Lægsgaard, E.; Bäumer, M.; Freund, H. J.; Besenbacher, F.; Stensgaard, I. Palladium Nanocrystals on Al₂O₃: Structure and Adhesion Energy. *Phys. Rev. Lett.* **1999**, *83*, 4120–4123.
- [192] Gong, X.-Q.; Selloni, A.; Dulub, O.; Jacobson, P.; Diebold, U. Small Au and Pt Clusters at the Anatase TiO₂(101) Surface: Behavior at Terraces, Steps, and Surface Oxygen Vacancies. *J. Am. Chem. Soc.* **2008**, *130*, 370–381.
- [193] Croy, J. R.; Mostafa, S.; Liu, J.; Sohn, Y.; Heinrich, H.; Cuenya, B. R. Support Dependence of MeOH Decomposition Over Size-Selected Pt Nanoparticles. *Catal. Lett.* **2007**, *119*, 209–216.

- [194] Verga, L. G.; Aarons, J.; Sarwar, M.; Thompsett, D.; Russell, A. E.; Skylaris, C.-K. Effect of Graphene Support on Large Pt Nanoparticles. *Phys. Chem. Chem. Phys.* **2016**, *18*, 32713–32722.
- [195] Tosoni, S.; Pacchioni, G. Trends in Adhesion Energies of Gold on MgO(100), Rutile TiO₂(110), and CeO₂(111) Surfaces: A Comparative DFT Study. *J. Phys. Chem. C* **2017**, *121*, 28328–28338.
- [196] Liu, Z.-P.; Gong, X.-Q.; Kohanoff, J.; Sanchez, C.; Hu, P. Catalytic Role of Metal Oxides in Gold-Based Catalysts: A First Principles Study of CO Oxidation on TiO₂ Supported Au. *Phys. Rev. Lett.* **2003**, *91*, 266102.
- [197] Giordano, L.; Baistrocchi, M.; Pacchioni, G. Bonding of Pd, Ag, and Au Atoms on MgO(100) Surfaces and MgO/Mo(100) Ultra-Thin Films: A Comparative DFT Study. *Phys. Rev. B* **2005**, *72*, 115403.
- [198] Mattsson, A. E.; Jennison, D. R. Computing Accurate Surface Energies and the Importance of Electron Self-Energy in Metal/Metal-Oxide Adhesion. *Surf. Sci.* **2002**, *520*, L611–L618.
- [199] Beltrán, J. I.; Muñoz, M. C. Ab Initio Study of Decohesion Properties in Oxide/Metal Systems. *Phys. Rev. B* **2008**, *78*.
- [200] Graoui, H.; Giorgio, S.; Enry, C. R. Effect of the Interface Structure on the High-Temperature Morphology of Supported Metal Clusters. *Philos. Mag. B* **2009**, *81*, 1649–1658.
- [201] Mager-Maury, C.; Bonnard, G.; Chizallet, C.; Sautet, P.; Raybaud, P. H₂-Induced Reconstruction of Supported Pt Clusters: Metal-Support Interaction Versus Surface Hydride. *ChemCatChem* **2011**, *3*, 200–207.
- [202] Goniakowski, J.; Jelea, A.; Mottet, C.; Barcaro, G.; Fortunelli, A.; Kuntová, Z.; Nita, F.; Levi, A. C.; Rossi, G.; Ferrando, R. Structures of Metal Nanoparticles Adsorbed on MgO(001). II. Pt and Pd. *J. Chem. Phys.* **2009**, *130*, 174703.
- [203] Rignanese, G. M.; De Vita, A.; Charlier, J. C.; Gonze, X.; Car, R. First-Principles Molecular-Dynamics Study of the (0001) α -Quartz Surface. *Phys. Rev. B* **2000**, *61*.
- [204] García-Mota, M.; Rieger, M.; Reuter, K. Ab Initio Prediction of the Equilibrium Shape of Supported Ag Nanoparticles on α -Al₂O₃(0001). *J. Catal.* **2015**, *321*, 1–6.
- [205] Wang, X. G.; Chaka, A.; Scheffler, M. Effect of the Environment on α -Al₂O₃ (0001) Surface Structures. *Phys. Rev. Lett.* **2000**, *84*, 3650–3.
- [206] Jensen, M. C. R.; Venkataramani, K.; Helveg, S.; Clausen, B. S.; Reichling, M.; Besenbacher, F.; Lauritsen, J. V. Morphology, Dispersion, and Stability of Cu Nanoclusters on Clean and Hydroxylated α -Al₂O₃(0001) Substrates. *J. Phys. Chem. C* **2008**, *112*, 16953–16960.
- [207] Digne, M.; Sautet, P.; Raybaud, P.; Euzen, P.; Toulhoat, H. Hydroxyl Groups on γ -Alumina Surfaces: A DFT Study. *J. Catal.* **2002**, *211*, 1–5.
- [208] Raybaud, P.; Chizallet, C.; Mager-Maury, C.; Digne, M.; Toulhoat, H.; Sautet, P. From γ -Alumina to Supported Platinum Nanoclusters in Reforming Conditions: 10 Years of DFT Modeling and Beyond. *J. Catal.* **2013**, *308*, 328–340.
- [209] Digne, M.; Sautet, P.; Raybaud, P.; Euzen, P.; Toulhoat, H. Use of DFT to Achieve a Rational Understanding of Acid-Basic Properties of γ -Alumina Surfaces. *J. Catal.* **2004**, *226*, 54–68.
- [210] Vitos, L.; Ruban, A. V.; Skriver, H. L.; Kollár, J. The Surface Energy of Metals. *Surf. Sci.* **1998**, *411*, 186–202.

- [211] Wang, S. et al. Universal Transition State Scaling Relations for (de)Hydrogenation over Transition Metals. *Phys. Chem. Chem. Phys.* **2011**, *13*, 20760–5.
- [212] Loffreda, D.; Delbecq, F.; Vigne, F.; Sautet, P. Fast Prediction of Selectivity in Heterogeneous Catalysis from Extended Bronsted-Evans-Polanyi Relations: a Theoretical Insight. *Angew. Chem. Int. Ed. Engl.* **2009**, *48*, 8978–80.
- [213] Fernández, E. M. et al. Scaling Relationships for Adsorption Energies on Transition Metal Oxide, Sulfide, and Nitride Surfaces. *Angew. Chem. Int. Ed. Engl.* **2008**, *47*, 4683–6.
- [214] Plessow, P. N.; Bajdich, M.; Greene, J.; Vojvodic, A.; Abild-Pedersen, F. Trends in the Thermodynamic Stability of Ultrathin Supported Oxide Films. *J. Phys. Chem. C* **2016**, *120*, 10351–10360.
- [215] O'Connor, N. J.; Jonayat, A. S. M.; Janik, M. J.; Senftle, T. P. Interaction Trends Between Single Metal Atoms and Oxide Supports Identified with Density Functional Theory and Statistical Learning. *Nat. Catal.* **2018**, *1*, 531–539.
- [216] Fampiou, I.; Ramasubramaniam, A. Binding of Pt Nanoclusters to Point Defects in Graphene: Adsorption, Morphology, and Electronic Structure. *J. Phys. Chem. C* **2012**, *116*, 6543–6555.
- [217] Binder, K. *Introduction: Theory and Technical Aspects of Monte Carlo Simulations*; Monte Carlo Methods in Statistical Physics. Topics in Current Physics; Springer: Berlin, Heidelberg, 1986; Vol. 7.
- [218] Voter, A. In *Radiation Effects in Solids*; Sickafus, K. E., Kotomin, E. A., Uberuaga, B. P., Eds.; Springer: Netherlands, 2007; pp 1–23.
- [219] Harris, P. J. F. Growth and Structure of Supported Metal Catalyst Particles. *Int. Mater. Rev.* **1995**, *40*, 97–115.
- [220] Geiser, J.; Blankenburg, S. Monte Carlo Simulations of Elastic Scattering with Applications to DC and High Power Pulsed Magnetron Sputtering For Ti_3SiC_2 . *Commun. Comput. Phys.* **2015**, *11*, 1618–1642.
- [221] Bird, G. *Molecular Gas Dynamics and the Direct Simulation of Gas Flows*; Oxford Science Publications: New York, 1994.
- [222] Bortz, A. B.; Kalos, M. H.; Lebowitz, J. L. New Algorithm for Monte-Carlo Simulation of Ising Spin Systems. *J. Comput. Phys.* **1975**, *17*, 10–18.
- [223] Kennard, H. *Kinetic Theory of Gases*; McGraw-Hill Book Company, Inc., 1938.
- [224] Maxwell, J. XV. On the Dynamical Theory of Gases. *The London, Edinburgh, and Dublin Philosophical Magazine and Journal of Science* **1868**, *35*, 49–88.
- [225] Chapman, S. On the Kinetic Theory of a Gas. *Phil. Trans.* **1918**, *217A*, 115–197.
- [226] Enskog, D. Kinetische Theorie der Vorgänge in mässig verdünnten Gasen. Ph.D. thesis, Upsala, 1917.
- [227] Landau, L. D.; Lifschitz, E. *Lehrbuch der theoretischen Physik, Band X, Physikalische Kinetik*, 1st ed.; Akademie-Verlag Berlin: Berlin, 1986.
- [228] Wedler, G. *Lehrbuch der physikalischen Chemie*, 5th ed.; WILEY-VCH Verlag GmbH & Co. KGaA: Weinheim, 2007; pp 812–817.
- [229] Phelps, A. V.; Greene, C. H.; Burke, J. P. Collision Cross Sections for Argon Atoms With Argon Atoms For Energies From 0.01 eV to 10 keV. *J. Phys. B: At., Mol. Opt. Phys.* **2000**, *33*, 2965–2981.

- [230] Somasundaram, T.; Lynden-Bell, R. M. The Velocity Distribution of Desorbing Molecules: A Simulation Study. *Mol. Phys.* **1999**, *97*, 1029–1034.
- [231] Knox, C. J. H.; Phillips, L. F. Maxwell versus Non-Maxwell Velocity Distributions for Molecules Emitted from a Liquid Surface. *J. Phys. Chem. B* **1998**, *102*, 10515–10520.
- [232] Harvie, D. J. E.; Fletcher, D. F. A Hydrodynamic and Thermodynamic Simulation of Droplet Impacts on Hot Surfaces, Part I: Theoretical Model. *Int. J. Heat Mass Transfer* **2001**, *44*, 2633–2642.
- [233] Gillespie, D. T. Exact Stochastic Simulation of Couple Chemical Reactions. *J. Phys. Chem.* **1977**, *81*, 2340–2361.
- [234] Johnson, C. A. Generalization of the Gibbs-Thomson Equation. *Surf. Sci.* **1965**, *3*, 429–444.
- [235] Meija, J. et al. Atomic Weights of the Elements 2013 (IUPAC Technical Report). *Pure Appl. Chem.* **2016**, *88*, 265.
- [236] Minkin, V. I. Glossary of Terms Used in Theoretical Organic Chemistry. *Pure Appl. Chem.* **1999**, *71*, 1919–1981.
- [237] Landau, L.; Lifschitz, E. *Statistical Physics*, 3rd ed.; Butterworth-Heinemann: Oxford, 1980; pp 1–33.
- [238] Dietze, E. M.; Plessow, P. N.; Studt, F. Modeling the Size Dependency of the Stability of Metal Nanoparticles. *The Journal of Physical Chemistry C* **2019**, *123*, 25464–25469.

9 Appendix

9.1 Extended data of thermodynamic stability of nanoparticles

Table 9.1: Lattice parameter a_0 in Å and surface energy $\gamma_{111}(a_0)$ in eV per surface atom used to parameterize the quadratic equation for $\gamma_{111}(a_0)$.

Ag		Au		Co		Cu		Ir		Ni		Os	
a_0	γ_{111}												
3.98	0.60	4.02	0.62	3.34	0.81	3.47	0.73	3.74	1.08	3.40	0.85	3.74	1.32
4.00	0.61	4.04	0.64	3.37	0.84	3.49	0.74	3.76	1.13	3.42	0.86	3.76	1.36
4.02	0.61	4.06	0.65	3.40	0.86	3.51	0.75	3.78	1.17	3.44	0.87	3.78	1.40
4.04	0.61	4.08	0.66	3.43	0.88	3.53	0.75	3.80	1.21	3.46	0.88	3.80	1.43
4.06	0.62	4.10	0.67	3.46	0.90	3.55	0.76	3.82	1.00	3.48	0.89	3.82	1.47
4.08	0.62	4.12	0.68	3.49	0.92	3.57	0.76	3.84	1.30	3.50	0.89	3.84	1.50

Pd		Pt		Rh		Ru		Al		Mg	
a_0	γ_{111}										
3.82	0.86	3.68	0.62	3.69	1.05	3.66	1.11	3.90	0.46	4.39	0.37
3.84	0.87	3.75	0.79	3.71	1.07	3.68	1.15	3.92	0.47	4.41	0.37
3.86	0.88	3.82	0.91	3.73	1.09	3.70	1.18	3.94	0.47	4.43	0.37
3.88	0.89	3.89	1.00	3.75	1.10	3.72	1.21	3.96	0.48	4.45	0.37
3.90	0.90	3.96	1.05	3.79	1.13	3.74	1.24	3.98	0.48	4.47	0.37
3.92	0.90	4.03	1.09	3.81	1.14	3.76	1.27	4.00	0.48	4.49	0.38

Table 9.2: Lattice parameter a_0 in Å and bulk chemical potential $\mu_{\text{bulk}}(a_0)$ in eV/atom used to parameterize the quadratic equation for $\mu_{\text{bulk}}(a_0)$. $\mu_{\text{bulk}}(a_0)$ is given relative to the gas phase atom.

Ag		Au		Co		Cu		Ir		Ni		Os	
a_0	μ_{bulk}												
3.98	-2.979	4.02	-3.661	3.34	-5.341	3.47	-3.950	3.74	-7.912	3.40	-5.162	3.74	-8.669
4.00	-2.991	4.04	-3.675	3.37	-5.394	3.49	-3.966	3.76	-7.954	3.42	-5.177	3.76	-8.710
4.02	-3.000	4.06	-3.684	3.40	-5.433	3.51	-3.979	3.78	-7.986	3.44	-5.187	3.78	-8.739
4.04	-3.005	4.08	-3.690	3.43	-5.458	3.53	-3.987	3.80	-8.008	3.46	-5.192	3.80	-8.759
4.06	-3.008	4.10	-3.691	3.46	-5.470	3.55	-3.992	3.82	-8.020	3.48	-5.193	3.82	-8.768
4.08	-3.009	4.12	-3.689	3.49	-5.472	3.57	-3.994	3.84	-8.024	3.50	-5.190	3.84	-8.768

Pd		Pt		Rh		Ru		Al		Mg	
a_0	μ_{bulk}										
3.82	-4.293	3.81	-6.149	3.71	-6.244	3.67	-7.122	3.90	-3.572	4.39	-1.688
3.84	-4.306	3.83	-6.185	3.73	-6.266	3.69	-7.158	3.92	-3.582	4.41	-1.691
3.86	-4.314	3.85	-6.213	3.75	-6.281	3.71	-7.185	3.94	-3.590	4.43	-1.693
3.88	-4.318	3.87	-6.233	3.77	-6.289	3.73	-7.204	3.96	-3.596	4.45	-1.694
3.90	-4.317	3.89	-6.245	3.79	-6.291	3.75	-7.215	3.98	-3.600	4.47	-1.694
3.92	-4.312	3.91	-6.251	3.81	-6.287	3.77	-7.219	4.00	-3.602	4.49	-1.693

Table 9.3: Coordination numbers of the surface atoms of the different nanoparticles. The first 6 rows correspond to cuboctahedral, the following 4 to cubic and the last 8 rows to octahedral clusters.

N_{atom}	$CN = 3$	$CN = 4$	$CN = 5$	$CN = 7$	$CN = 8$	$CN = 9$
13	0	0	12	0	0	0
55	0	0	12	24	6	0
147	0	0	12	48	24	8
309	0	0	12	72	54	24
561	0	0	12	96	96	48
923	0	0	12	120	150	80
63	8	0	12	0	30	0
171	0	0	36	0	72	0
365	8	0	36	0	150	0
665	0	0	60	0	240	0
19	0	6	0	12	0	0
44	0	6	0	24	0	8
85	0	6	0	36	0	24
146	0	6	0	48	0	48
231	0	6	0	60	0	80
344	0	6	0	72	0	120
489	0	6	0	84	0	168
670	0	6	0	96	0	224

Table 9.4: Surface energy contributions of the (111) and (100) faces in eV for cuboctahedral, cubic and octahedral nanoclusters.

N_{atom}	(111)	(100)
13	0.0	16.05
55	16.13	32.10
147	36.28	72.22
309	64.50	128.40
561	100.78	200.62
923	145.13	288.89
63	0.0	64.20
171	0.0	144.45
365	0.0	256.79
665	0.0	401.24
19	16.13	0.0
44	36.28	0.0
85	64.50	0.0
146	100.78	0.0
231	145.13	0.0
344	197.53	0.0
489	258.00	0.0
670	326.54	0.0

Table 9.5: Total energies calculated with DFT, corresponding chemical potentials relative to the bulk chemical potential and chemical potentials predicted with the stability model for all nanoparticles. The mean absolute error is 0.09 eV/atom, excluding Pt₁₃ and Pt₁₉. The maximum error is 0.32 eV/atom.

Metal	N_{atom}	E_{total} [eV]	μ_{metal} [eV/atom]	μ_{model} [eV/atom]
Ag	55	-133.67	0.78	1.03
Ag	147	-387.95	0.57	0.68
Ag	309	-854.20	0.44	0.51
Ag	561	-1599.29	0.36	0.41
Au	55	-164.04	0.90	1.07
Au	147	-475.27	0.65	0.72
Au	309	-1042.80	0.51	0.55
Au	561	-1949.97	0.41	0.44
Co	55	-334.04	1.29	1.48
Co	147	-944.75	0.94	1.00
Co	309	-2051.29	0.72	0.76
Cu	55	-180.97	0.95	1.22
Cu	147	-513.85	0.74	0.82
Cu	309	-1129.84	0.58	0.63
Cu	561	-2112.62	0.47	0.51
Ir	55	-417.02	1.96	1.98
Ir	147	-1202.23	1.37	1.35
Ir	309	-2618.22	1.07	1.03

Metal	N_{atom}	E_{total} [eV]	μ_{metal} [eV/atom]	μ_{model} [eV/atom]
Ir	561	-4864.30	0.88	0.83
Ni	55	-258.84	1.16	1.29
Ni	147	-733.41	0.88	0.89
Ni	309	-1602.59	0.68	0.69
Os	55	-525.61	2.13	2.42
Os	147	-1488.33	1.57	1.63
Os	309	-3235.44	1.22	1.23
Os	561	-5999.71	1.00	0.99
Pd	55	-254.11	1.18	1.48
Pd	147	-727.07	0.85	0.98
Pd	309	-1585.96	0.67	0.74
Pd	561	-2945.42	0.55	0.60
Pt	13	-56.11	2.55	3.01
Pt	55	-295.94	1.48	1.60
Pt	147	-854.15	1.05	1.09
Pt	309	-1868.81	0.82	0.83
Pt	561	-3477.16	0.67	0.68
Pt	923	-5817.75	0.56	0.57
Pt	19	-91.42	2.05	2.42
Pt	44	-237.31	1.47	1.66
Pt	85	-480.95	1.21	1.27
Pt	146	-855.70	1.00	1.04
Pt	231	-1387.70	0.86	0.88
Pt	344	-2104.11	0.75	0.77
Pt	670	-4198.94	0.60	0.61
Pt	63	-339.13	1.48	1.72
Pt	171	-989.15	1.08	1.16
Pt	365	-2197.59	0.84	0.90
Pt	489	-3032.10	0.66	0.72
Pt	665	-4100.90	0.70	0.73
Rh	55	-344.53	1.59	1.85
Rh	147	-988.42	1.13	1.24
Rh	309	-2152.20	0.89	0.94
Rh	561	-3997.66	0.73	0.76
Ru	55	-436.55	1.75	2.08
Ru	147	-1233.83	1.30	1.39
Ru	309	-2683.12	1.01	1.05
Ru	561	-4975.59	0.82	0.85
Al	55	-177.80	0.68	0.84
Al	147	-505.10	0.48	0.55
Al	309	-1091.77	0.38	0.41
Al	561	-2022.23	0.31	0.33
Mg	55	-59.36	0.62	0.83
Mg	147	-185.41	0.43	0.51

Metal	N_{atom}	E_{total} [eV]	μ_{metal} [eV/atom]	μ_{model} [eV/atom]
Mg	309	-418.89	0.34	0.36
Mg	561	-795.43	0.28	0.28

9.2 Extended data for adhesion energy calculation

Table 9.6: Strain of symmetric metal/oxide interfaces in %.

Surface	O- α -SiO ₂ (0001)			O- α -Al ₂ O ₃ (0001)	
	Metal	fcc(111)			fcc(111)
Metal supercell	2×2	$(\sqrt{3} \times \sqrt{3})R30^\circ$	$(\sqrt{13} \times \sqrt{13})R14^\circ$	$(\sqrt{3} \times \sqrt{3})R30^\circ$	$(\sqrt{13} \times \sqrt{13})R14^\circ$
Ag	16.12	0.54	4.66	4.22	8.48
Au	16.85	1.19	5.32	4.89	9.17
Cu	1.73	-11.91	-8.30	-8.69	-4.95
Ir	9.43	-5.22	-1.36	-1.75	2.25
Ni	-1.09	-14.35	-10.84	-11.22	-7.58
Pd	10.76	-4.07	-0.16	-0.56	3.49
Pt	11.65	-3.28	0.65	0.25	4.33
Os	9.15	-5.46	-1.60	-2.01	1.99
Rh	7.94	-6.53	-2.72	-3.11	0.84
Ru	7.46	-6.93	-3.13	-3.53	0.41

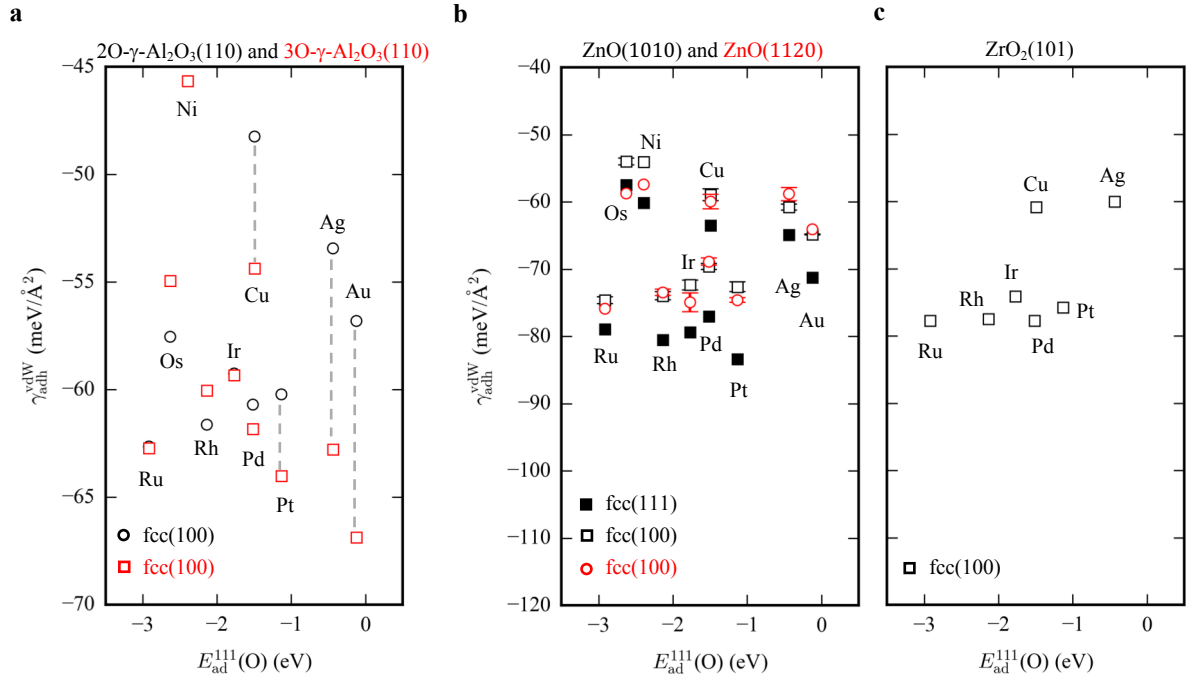


Figure 9.1: VdW-contribution to adhesion energies. (a) VdW-contribution with D3-zero damping to adhesion energies for the fcc(100)-surface of the hydroxylated γ -Al₂O₃ surfaces with two and three adsorbed water molecules per unit cell. (b) VdW-contribution with D3-zero damping contribution of adhesion energies for the (10 $\bar{1}$ 1) and (11 $\bar{2}$ 0)-surfaces of ZnO in wurtzite structure. (c) VdW-contribution with D3-zero damping of adhesion energies for the (101)-surface of tetragonal ZrO₂.

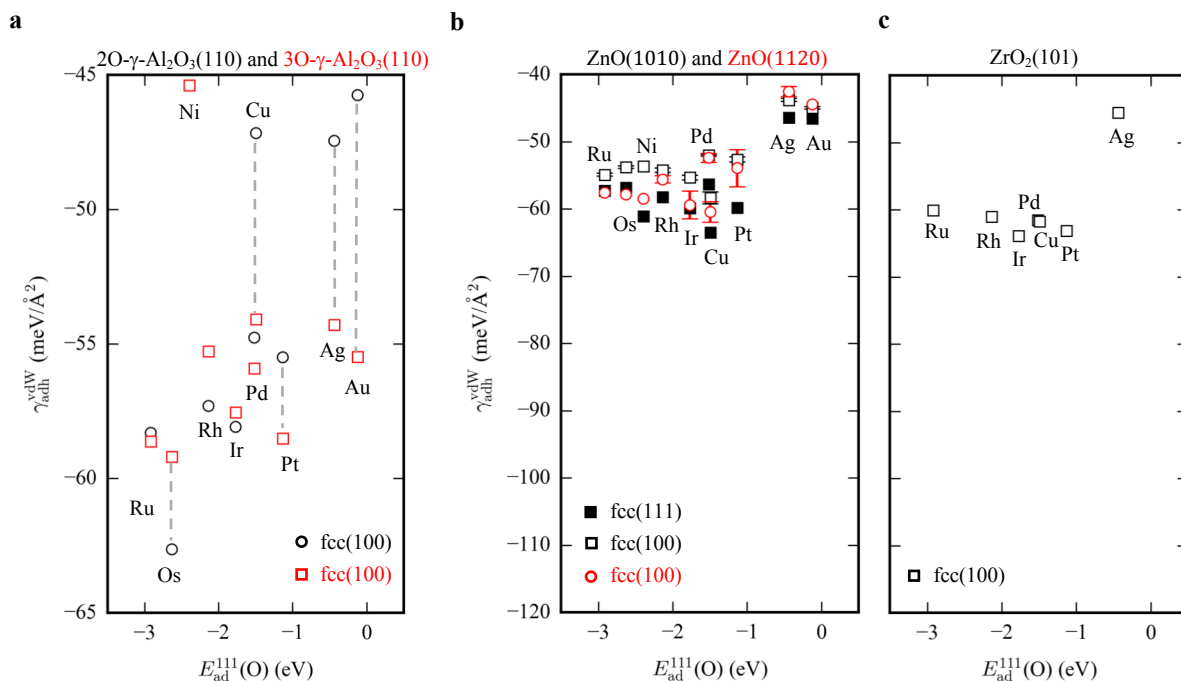


Figure 9.2: VdW-contribution to adhesion energies. (a) VdW-contribution with D3-BJ damping to adhesion energies for the fcc(100)-surface of the hydroxylated $\gamma\text{-Al}_2\text{O}_3$ surfaces with two and three adsorbed water molecules per unit cell. (b) VdW-contribution with D3-BJ damping contribution of adhesion energies for the $(10\bar{1}1)$ and $(11\bar{2}0)$ -surfaces of ZnO in wurtzite structure. (c) VdW-contribution with D3-BJ damping of adhesion energies for the (101) -surface of tetragonal ZrO_2 .

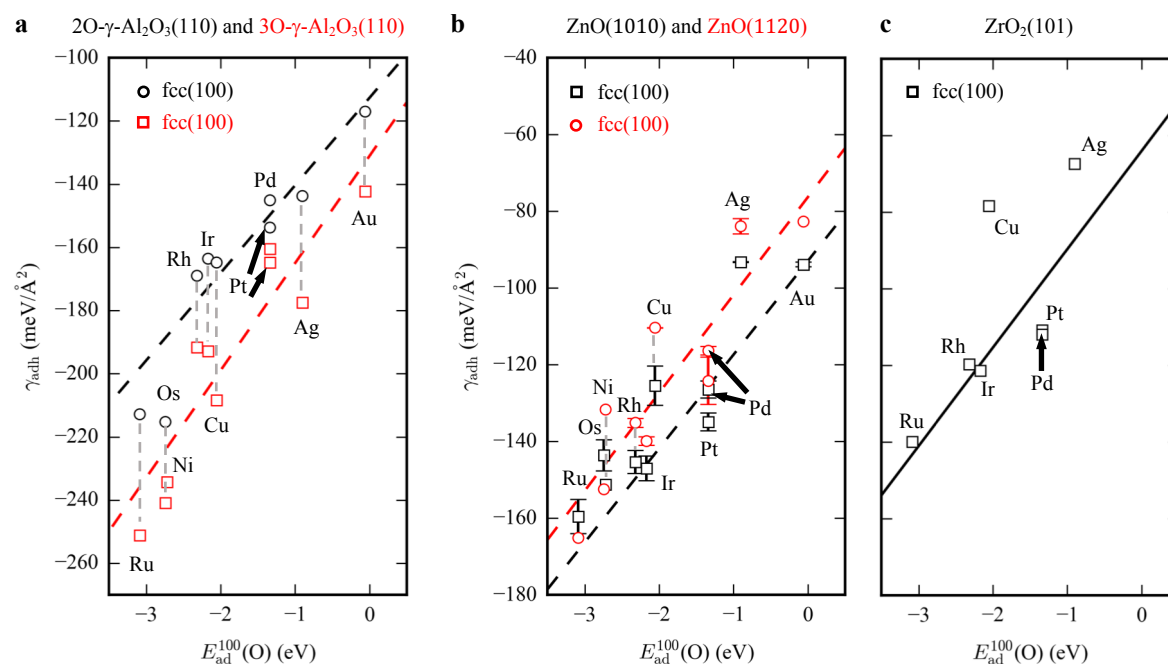


Figure 9.3: Adhesion energies as a function of oxygen adsorption energies on clean fcc(100) metal surfaces. (a) Adhesion energies between fcc(100)-surfaces and the oxidized $\gamma\text{-Al}_2\text{O}_3(110)$ surfaces derived from hydroxylated surfaces with two and three adsorbed water molecules per unit cell. (b) Adhesion energies for the $(10\bar{1}0)$ - and $(11\bar{2}0)$ -surfaces of ZnO in wurtzite structure. (c) Adhesion energies for the (101) -surface of tetragonal ZrO_2 .

Table 9.7: Strain of unsymmetric metal/oxide interfaces in %.

Surface	2O- γ -Al ₂ O ₃ (110)		3O- γ -Al ₂ O ₃ (110)		ZrO ₂ (101)	
Metal	fcc(100)		fcc(100)		fcc(100)	
Metal supercell	3 × 3		3 × 3		7 × 4	
	a	b	a	b	a	b
Ag	3.48	7.57	3.48	7.57	5.68	6.47
Au	4.13	8.24	4.13	8.24	6.34	7.13
Cu	-9.34	-5.76	-9.34	-5.76	-7.41	-6.73
Ir	-2.48	1.37	-2.48	1.37	-0.41	0.33
Ni	-11.85	-8.38	-11.85	-8.38	-9.98	-9.31
Pd	-1.29	2.60	-1.29	2.60	0.80	1.55
Pt	-0.50	3.42	-0.50	3.42	1.61	2.37
Os	-2.73	1.11	-2.73	1.11	-0.67	0.07
Rh	-3.81	-0.01	-3.81	-0.01	-1.77	-1.03
Ru	-4.24	-0.46	-4.24	-0.46	-2.21	-1.48

Surface	TiO ₂									
Metal	fcc(100)								fcc(111)	
Oxide supercell	2 × 1		3 × 1		4 × 1		1 × 2		3 × 5	
Metal supercell	5 × 1		7 × 1		9 × 1		$(\sqrt{5} \times \sqrt{5})R27^\circ$		$7 \times 3\sqrt{3}$	
	a	b	a	b	a	b	a	b	a	b
Ag	9.64	-2.67	2.33	-2.67	-1.32	-2.67	-1.95	8.80	2.33	1.13
Au	10.33	-2.06	2.97	-2.06	-0.70	-2.06	-1.33	9.49	2.97	1.78
Cu	-3.94	-14.73	-10.35	-14.73	-13.55	-14.73	-14.09	-4.67	-10.35	-11.40
Ir	3.33	-8.28	-3.56	-8.28	-7.01	-8.28	-7.58	2.55	-3.56	-4.67
Ni	-6.61	-17.09	-12.83	-17.09	-15.95	-17.09	-16.47	-7.31	-12.83	-13.85
Pd	4.58	-7.16	-2.39	-7.16	-5.88	-7.16	-6.46	3.80	-2.39	-3.51
Pt	5.42	-6.42	-1.61	-6.42	-5.12	-6.42	-5.69	4.64	-1.61	-2.72
Os	3.06	-8.51	-3.81	-8.51	-7.25	-8.51	-7.81	2.30	-3.81	-4.91
Rh	1.92	-9.53	-4.88	-9.53	-8.27	-9.53	-8.85	1.14	-4.88	-5.99
Ru	1.46	-9.93	-5.30	-9.93	-8.68	-9.93	-9.24	0.71	-5.30	-6.39

Surface	ZnO(10 $\bar{1}$ 0)						ZnO(11 $\bar{2}$ 0)			
Metal	fcc(100)				fcc(111)		fcc(100)			
Oxide supercell	4 × 1		5 × 1		3 × 1		1 × 1		2 × 3	
Metal supercell	5 × 2		6 × 2		$2\sqrt{3} \times 2$		2 × 2		$3\sqrt{2} \times 4\sqrt{2}$	
	a	b	a	b	a	b	a	b	a	b
Ag	10.00	9.07	5.60	9.07	1.59	9.07	1.60	9.07	7.77	2.83
Au	10.68	9.75	6.26	9.75	2.24	9.75	2.24	9.75	8.44	3.47
Cu	-3.63	-4.45	-7.49	-4.45	-11.00	-4.45	-10.99	-4.45	-5.59	-9.91
Ir	3.66	2.78	-0.49	2.78	-4.24	2.78	-4.25	2.78	1.56	-3.10
Ni	-6.31	-7.10	-10.05	-7.10	-13.46	-7.10	-13.45	-7.10	-8.20	-12.41
Pd	4.92	4.03	0.72	4.03	-3.07	4.03	-3.09	4.03	2.79	-1.92
Pt	5.76	4.86	1.53	4.86	-2.28	4.86	-2.31	4.86	3.62	-1.13
Os	3.39	2.52	-0.75	2.52	-4.48	2.52	-4.50	2.52	1.30	-3.35
Rh	2.24	1.38	-1.84	1.38	-5.56	1.38	-5.55	1.38	0.17	-4.42
Ru	1.79	0.93	-2.28	0.93	-5.97	0.93	-5.98	0.93	-0.27	-4.84

Table 9.8: Calculated adhesion energies of the metal/oxide interfaces in $\text{meV}/\text{\AA}^2$.

Surface	O- α -SiO ₂ (0001)			3O- γ -Al ₂ O ₃ (110)	
Metal	fcc(111)			fcc(111)	
Metal supercell	2 × 2	($\sqrt{3} \times \sqrt{3}$)R30°	($\sqrt{13} \times \sqrt{13}$)R14°	($\sqrt{3} \times \sqrt{3}$)R30°	($\sqrt{13} \times \sqrt{13}$)R14°
Ag	-219.96	-190.41	-195.88	-251.77	-258.07
Au	-164.07	-146.90	-149.18	-196.95	-216.91
Cu	-243.12	-215.14	-228.33	-282.91	-308.28
Ir	-235.13	-224.36	-235.70	-398.92	-348.53
Ni	-248.07	-224.90	-	-340.84	-
Pd	-211.86	-181.82	-198.75	-281.49	-286.48
Pt	-202.76	-184.00	-195.98	-315.45	-289.45
Os	-281.74	-249.65	-245.78	-460.47	-373.82
Rh	-255.89	-219.46	-234.45	-372.25	-345.01
Ru	-298.01	-268.43	-251.79	-441.62	-392.24

Surface	TiO ₂					2O- γ -Al ₂ O ₃	3O- γ -Al ₂ O ₃
Metal	fcc(100)				fcc(111)	fcc(100)	fcc(100)
Oxide supercell	2 × 1	3 × 1	4 × 1	1 × 2	3 × 5	1 × 1	1 × 1
Metal supercell	5 × 1	7 × 1	9 × 1	($\sqrt{5} \times \sqrt{5}$)R27°	7 × 3 $\sqrt{3}$	3 × 3	3 × 3
Ag	-75.95	-81.19	-81.67	-84.61	-73.52	-143.69	-177.48
Au	-64.74	-68.64	-69.07	-70.45	-61.48	-117.01	-142.27
Cu	-110.29	-	-	-	-	-164.76	-208.34
Ir	-108.99	-105.88	-126.74	-125.37	-93.54	-163.51	-192.80
Ni	-	-	-	-	-	-	-234.17
Pd	-97.69	-98.26	-	-103.32	-99.01	-153.71	-160.46
Pt	-89.86	-91.93	-86.25	-94.24	-86.49	-145.02	-164.71
Os	-111.34	-107.72	-	-128.57	-81.45	-215.22	-240.84
Rh	-115.12	-105.62	-	-126.47	-118.41	-168.96	-191.66
Ru	-136.08	-	-	-187.68	-126.09	-212.72	-251.07

Surface	ZnO(10 $\bar{1}$ 0)			ZnO(11 $\bar{2}$ 0)		ZrO ₂ (101)
Metal	fcc(100)		fcc(111)	fcc(100)		fcc(100)
Oxide supercell	4 × 1	5 × 1	3 × 1	1 × 1	2 × 3	3 × 3
Metal supercell	5 × 2	6 × 2	2 $\sqrt{3}$ × 2	2 × 2	3 $\sqrt{2}$ × 4 $\sqrt{2}$	7 × 4
Ag	-93.35	-93.10	-91.34	-85.92	-81.91	-67.37
Au	-93.23	-94.43	-89.60	-82.65	-	-
Cu	-120.27	-130.51	-136.76	-110.43	-110.27	-78.35
Ir	-143.79	-150.27	-141.63	-140.96	-138.81	-121.29
Ni	-151.16	-	-161.54	-131.61	-	-
Pd	-124.26	-128.70	-133.31	-115.21	-117.43	-111.85
Pt	-132.58	-137.24	-137.33	-118.03	-130.35	-110.72
Os	-139.51	-147.65	-121.79	-152.48	-	-
Rh	-142.27	-148.34	-148.25	-134.02	-136.27	-119.60
Ru	-155.10	-163.96	-147.29	-165.09	-	-139.93

Table 9.9: Minimum and maximum M-O distance in Å for fcc(111)($\sqrt{13} \times \sqrt{13}R14^\circ$)/O- α -SiO₂(0001) and fcc(111)($\sqrt{13} \times \sqrt{13}R14^\circ$)/O- α -Al₂O₃(0001) and the derived, employed cutoff criterion in Å.

Metal	O- α -SiO ₂ (0001)		O- α -Al ₂ O ₃ (0001)		Employed cut-off criterion
	d_{\min}	d_{\max}	d_{\min}	d_{\max}	
Ag	2.15	2.22	2.07	2.30	2.60
Au	2.07	2.23	2.02	2.19	2.49
Cu	1.85	2.05	1.85	2.01	2.31
Ir	1.95	2.13	1.96	2.23	2.53
Ni	1.85	1.91	1.80	1.89	2.19
Pd	1.97	2.10	1.97	2.14	2.44
Pt	1.99	2.12	1.95	2.12	2.42
Os	1.95	2.15	1.97	2.20	2.50
Rh	1.94	2.07	1.94	2.11	2.41
Ru	1.94	2.10	1.95	2.12	2.42

Table 9.10: Obtained number of interfacial oxygen atoms N_O per supercell for all metal/interface combinations with the criterion mentioned in Table 9.9. fcc(111)($\sqrt{13} \times \sqrt{13}R14^\circ$)/O- α -SiO₂(0001) and fcc(111)($\sqrt{13} \times \sqrt{13}R14^\circ$)/O- α -Al₂O₃(0001) are used. The column labeled ideal, gives the number of oxygen atoms that one could derive from the number of surface oxygen atoms of the clean oxide surface. Where this number is close to the actual number, it was used as the actual concentration (last column).

Oxide surface	Metal surface	Metal supercell	Ag	Au	Cu	Ir	Ni	Pd	Pt	Os	Rh	Ru	ideal	used value
O- α -SiO ₂ (0001)	fcc(111)	$\sqrt{13}$	8	8	8	8	8	8	8	8	8	8	8	8
O- α -Al ₂ O ₃ (0001)	fcc(111)	$\sqrt{13}$	12	12	12	12	12	12	12	12	12	12	12	12
2O- γ -Al ₂ O ₃ (110)	fcc(100)	3 × 3	5	5	5	5	-	5	5	-	5	7	2	5.250
3O- γ -Al ₂ O ₃ (110)	fcc(100)	3 × 3	8	-	8	6	7	6	6	-	6	6	3	6.625
TiO ₂ (110)	fcc(100)	7 × 1	3	2	-	3	-	3	3	3	3	3	3	3
	fcc(111)	7 × 3	15	8	-	15	-	15	14	15	15	16	15	15
ZnO(10 $\bar{1}$ 0)	fcc(100)	5 × 2	4	2	4	4	4	4	4	4	4	4	4	4
	fcc(111)	2 × 2	3	1	3	3	3	3	3	3	3	3	3	3
ZnO(11 $\bar{2}$ 0)	fcc(100)	2 × 2	2	0	2	2	2	2	2	2	2	2	2	2
ZrO ₂ (101)	fcc(100)	3 × 3	11	-	9	16	-	14	14	-	14	18	9	13.714

Table 9.11: Interface energy, oxide energy, metal energy in eV and surface area in Å² for all calculated metal/oxide structures. In the case of the hydroxylated oxide, the surface area of the strain-free oxide surface is used and the number of hydroxyl groups per supercell and the stability difference between hydroxylated and oxidized surfaces per supercell given. For the stoichiometric interfaces the surface area depending on the metal lattice constant is given.

Surface	$E_{\text{Interface}}$	E_{Oxide}	E_{Metal}	Area	N_{OH}	$\Delta\gamma_{\text{ox-lat}}^{\text{ox}}$
2O- γ -Al ₂ O ₃ (110)/fcc(100)3x3/Ag	-805.82	-687.91	-131.37	67.11	4	142.76
2O- γ -Al ₂ O ₃ (110)/fcc(100)3x3/Au	-830.71	-686.26	-159.70	67.11	4	142.76
2O- γ -Al ₂ O ₃ (110)/fcc(100)3x3/Cu	-840.04	-678.10	-173.98	67.11	4	142.76

Surface	$E_{\text{Interface}}$	E_{Oxide}	E_{Metal}	Area	N_{OH}	$\Delta\gamma_{\text{ox-lat}}^{\text{ox}}$
2O- γ -Al ₂ O ₃ (110)/fcc(100)3x3/Ir	-1080.43	-694.35	-398.21	67.11	4	142.76
2O- γ -Al ₂ O ₃ (110)/fcc(100)3x3/Os	-1173.77	-694.27	-488.16	67.11	4	142.76
2O- γ -Al ₂ O ₃ (110)/fcc(100)3x3/Pd	-922.69	-694.33	-241.15	67.11	4	142.76
2O- γ -Al ₂ O ₃ (110)/fcc(100)3x3/Pt	-965.33	-693.87	-284.83	67.11	4	142.76
2O- γ -Al ₂ O ₃ (110)/fcc(100)3x3/Rh	-1008.84	-693.48	-327.12	67.11	4	142.76
2O- γ -Al ₂ O ₃ (110)/fcc(100)3x3/Ru	-1089.56	-693.02	-405.37	67.11	4	142.76
3O- γ -Al ₂ O ₃ (110)/fcc(100)3x3/Ag	-813.09	-705.01	-131.37	67.11	6	222.33
3O- γ -Al ₂ O ₃ (110)/fcc(100)3x3/Au	-837.54	-703.49	-159.70	67.11	6	222.33
3O- γ -Al ₂ O ₃ (110)/fcc(100)3x3/Cu	-846.80	-694.04	-173.98	67.11	6	222.33
3O- γ -Al ₂ O ₃ (110)/fcc(100)3x3/Ir	-1086.75	-710.81	-398.21	67.11	6	222.33
3O- γ -Al ₂ O ₃ (110)/fcc(100)3x3/Ni	-904.77	-680.24	-244.02	67.11	6	222.33
3O- γ -Al ₂ O ₃ (110)/fcc(100)3x3/Os	-1179.85	-710.73	-488.16	67.11	6	222.33
3O- γ -Al ₂ O ₃ (110)/fcc(100)3x3/Pd	-927.59	-710.87	-241.15	67.11	6	222.33
3O- γ -Al ₂ O ₃ (110)/fcc(100)3x3/Pt	-971.15	-710.47	-284.83	67.11	6	222.33
3O- γ -Al ₂ O ₃ (110)/fcc(100)3x3/Rh	-1014.65	-709.87	-327.12	67.11	6	222.33
3O- γ -Al ₂ O ₃ (110)/fcc(100)3x3/Ru	-1096.39	-709.37	-405.37	67.11	6	222.33
O- α -Al ₂ O ₃ (0001)/fcc(111)sqrt13/Ag	-1127.44	-1070.81	-109.60	79.38	12	414.39
O- α -Al ₂ O ₃ (0001)/fcc(111)sqrt13/Au	-1145.77	-1067.55	-134.45	79.38	12	414.39
O- α -Al ₂ O ₃ (0001)/fcc(111)sqrt13/Cu	-1173.06	-1076.28	-145.76	79.38	12	414.39
O- α -Al ₂ O ₃ (0001)/fcc(111)sqrt13/Ir	-1382.47	-1089.65	-338.61	79.38	12	414.39
O- α -Al ₂ O ₃ (0001)/fcc(111)sqrt13/Os	-1466.95	-1089.91	-420.82	79.38	12	414.39
O- α -Al ₂ O ₃ (0001)/fcc(111)sqrt13/Pd	-1240.33	-1087.75	-203.29	79.38	12	414.39
O- α -Al ₂ O ₃ (0001)/fcc(111)sqrt13/Pt	-1276.08	-1085.67	-240.88	79.38	12	414.39
O- α -Al ₂ O ₃ (0001)/fcc(111)sqrt13/Rh	-1321.69	-1090.47	-277.28	79.38	12	414.39
O- α -Al ₂ O ₃ (0001)/fcc(111)sqrt13/Ru	-1395.04	-1090.45	-346.90	79.38	12	414.39
O- α -Al ₂ O ₃ (0001)/fcc(111)sqrt3/Ag	-293.12	-271.55	-34.93	19.85	3	414.39
O- α -Al ₂ O ₃ (0001)/fcc(111)sqrt3/Au	-299.26	-271.08	-42.64	19.85	3	414.39
O- α -Al ₂ O ₃ (0001)/fcc(111)sqrt3/Cu	-295.38	-261.80	-46.32	19.85	3	414.39
O- α -Al ₂ O ₃ (0001)/fcc(111)sqrt3/Ir	-368.48	-271.99	-106.94	19.85	3	414.39
O- α -Al ₂ O ₃ (0001)/fcc(111)sqrt3/Ni	-307.72	-254.10	-65.22	19.85	3	414.39
O- α -Al ₂ O ₃ (0001)/fcc(111)sqrt3/Os	-394.30	-271.86	-131.66	19.85	3	414.39
O- α -Al ₂ O ₃ (0001)/fcc(111)sqrt3/Pd	-323.97	-272.45	-64.30	19.85	3	414.39
O- α -Al ₂ O ₃ (0001)/fcc(111)sqrt3/Pt	-336.78	-272.61	-76.28	19.85	3	414.39
O- α -Al ₂ O ₃ (0001)/fcc(111)sqrt3/Rh	-347.52	-271.06	-87.44	19.85	3	414.39
O- α -Al ₂ O ₃ (0001)/fcc(111)sqrt3/Ru	-369.79	-270.68	-108.71	19.85	3	414.39
O- α -SiO ₂ (0001)/fcc(111)2x2/Ag	-249.94	-211.27	-46.54	21.33	2	272.03
O- α -SiO ₂ (0001)/fcc(111)2x2/Au	-258.28	-210.46	-56.89	21.33	2	272.03
O- α -SiO ₂ (0001)/fcc(111)2x2/Cu	-275.46	-221.10	-61.74	21.33	2	272.03
O- α -SiO ₂ (0001)/fcc(111)2x2/Ir	-352.48	-217.47	-142.55	21.33	2	272.03
O- α -SiO ₂ (0001)/fcc(111)2x2/Ni	-300.99	-221.27	-86.99	21.33	2	272.03
O- α -SiO ₂ (0001)/fcc(111)2x2/Os	-386.66	-217.67	-175.54	21.33	2	272.03
O- α -SiO ₂ (0001)/fcc(111)2x2/Pd	-294.18	-216.42	-85.79	21.33	2	272.03
O- α -SiO ₂ (0001)/fcc(111)2x2/Pt	-309.08	-215.66	-101.66	21.33	2	272.03
O- α -SiO ₂ (0001)/fcc(111)2x2/Rh	-327.95	-218.52	-116.54	21.33	2	272.03

Surface	$E_{\text{Interface}}$	E_{Oxide}	E_{Metal}	Area	N_{OH}	$\Delta\gamma_{\text{ox-lat}}^{\text{ox}}$
O- α -SiO ₂ (0001)/fcc(111)2x2/Ru	-357.54	-218.81	-144.93	21.33	2	272.03
O- α -SiO ₂ (0001)/fcc(111)sqrt13/Ag	-956.92	-880.85	-109.60	85.3	8	272.03
O- α -SiO ₂ (0001)/fcc(111)sqrt13/Au	-976.78	-879.85	-134.45	85.3	8	272.03
O- α -SiO ₂ (0001)/fcc(111)sqrt13/Cu	-983.28	-868.28	-145.76	85.3	8	272.03
O- α -SiO ₂ (0001)/fcc(111)sqrt13/Ir	-1192.90	-884.43	-338.61	85.3	8	272.03
O- α -SiO ₂ (0001)/fcc(111)sqrt13/Os	-1275.85	-884.31	-420.82	85.3	8	272.03
O- α -SiO ₂ (0001)/fcc(111)sqrt13/Pd	-1054.86	-884.86	-203.29	85.3	8	272.03
O- α -SiO ₂ (0001)/fcc(111)sqrt13/Pt	-1092.00	-884.64	-240.88	85.3	8	272.03
O- α -SiO ₂ (0001)/fcc(111)sqrt13/Rh	-1130.26	-883.23	-277.28	85.3	8	272.03
O- α -SiO ₂ (0001)/fcc(111)sqrt13/Ru	-1200.83	-882.69	-346.90	85.3	8	272.03
O- α -SiO ₂ (0001)/fcc(111)sqrt3/Ag	-247.64	-221.21	-34.93	21.33	2	272.03
O- α -SiO ₂ (0001)/fcc(111)sqrt3/Au	-254.31	-221.10	-42.64	21.33	2	272.03
O- α -SiO ₂ (0001)/fcc(111)sqrt3/Cu	-250.37	-212.02	-46.32	21.33	2	272.03
O- α -SiO ₂ (0001)/fcc(111)sqrt3/Ir	-318.84	-219.67	-106.94	21.33	2	272.03
O- α -SiO ₂ (0001)/fcc(111)sqrt3/Ni	-264.58	-207.13	-65.22	21.33	2	272.03
O- α -SiO ₂ (0001)/fcc(111)sqrt3/Os	-343.95	-219.52	-131.66	21.33	2	272.03
O- α -SiO ₂ (0001)/fcc(111)sqrt3/Pd	-275.90	-220.29	-64.30	21.33	2	272.03
O- α -SiO ₂ (0001)/fcc(111)sqrt3/Pt	-288.26	-220.62	-76.28	21.33	2	272.03
O- α -SiO ₂ (0001)/fcc(111)sqrt3/Rh	-298.29	-218.74	-87.44	21.33	2	272.03
O- α -SiO ₂ (0001)/fcc(111)sqrt3/Ru	-320.28	-218.41	-108.71	21.33	2	272.03
TiO ₂ (110)/fcc(100)5x1/Ag	-466.67	-422.60	-40.92	41.49		
TiO ₂ (110)/fcc(100)5x1/Au	-474.99	-422.25	-50.01	42.01		
TiO ₂ (110)/fcc(100)5x1/Cu	-457.77	-399.84	-54.42	31.85		
TiO ₂ (110)/fcc(100)5x1/Ir	-550.78	-420.85	-125.91	36.86		
TiO ₂ (110)/fcc(100)5x1/Os	-579.13	-420.51	-154.53	36.68		
TiO ₂ (110)/fcc(100)5x1/Pd	-501.99	-422.11	-76.19	37.76		
TiO ₂ (110)/fcc(100)5x1/Pt	-515.71	-422.65	-89.61	38.38		
TiO ₂ (110)/fcc(100)5x1/Rh	-526.42	-418.68	-103.62	35.85		
TiO ₂ (110)/fcc(100)5x1/Ru	-550.78	-417.83	-128.11	35.54		
TiO ₂ (110)/fcc(100)7x1/Ag	-699.77	-637.94	-57.12	58.08		
TiO ₂ (110)/fcc(100)7x1/Au	-711.88	-637.91	-69.94	58.82		
TiO ₂ (110)/fcc(100)7x1/Ir	-807.52	-625.88	-176.17	51.60		
TiO ₂ (110)/fcc(100)7x1/Os	-846.60	-624.87	-216.20	51.35		
TiO ₂ (110)/fcc(100)7x1/Pd	-742.09	-630.28	-106.61	52.86		
TiO ₂ (110)/fcc(100)7x1/Pt	-763.08	-632.69	-125.45	53.73		
TiO ₂ (110)/fcc(100)7x1/Rh	-769.98	-619.60	-145.07	50.19		
TiO ₂ (110)/fcc(100)9x1/Ag	-929.64	-849.85	-73.68	74.68		
TiO ₂ (110)/fcc(100)9x1/Au	-945.98	-850.71	-90.05	75.62		
TiO ₂ (110)/fcc(100)9x1/Ir	-1059.35	-824.69	-226.25	66.34		
TiO ₂ (110)/fcc(100)9x1/Pt	-1004.17	-836.70	-161.51	69.08		
TiO ₂ (110)/fcc(100)sqrt5/Ag	-465.16	-420.72	-40.93	41.49		
TiO ₂ (110)/fcc(100)sqrt5/Au	-473.10	-420.24	-49.91	42.01		
TiO ₂ (110)/fcc(100)sqrt5/Ir	-551.41	-421.10	-125.69	36.86		
TiO ₂ (110)/fcc(100)sqrt5/Os	-579.98	-420.81	-154.46	36.68		

Surface	$E_{\text{Interface}}$	E_{Oxide}	E_{Metal}	Area	N_{OH}	$\Delta\gamma_{\text{ox-lat}}^{\text{ox}}$
TiO ₂ (110)/fcc(100)sqrt5/Pd	-502.18	-422.16	-76.11	37.76		
TiO ₂ (110)/fcc(100)sqrt5/Pt	-515.73	-422.54	-89.58	38.38		
TiO ₂ (110)/fcc(100)sqrt5/Rh	-527.18	-419.13	-103.52	35.85		
TiO ₂ (110)/fcc(100)sqrt5/Ru	-553.20	-418.37	-128.16	35.54		
TiO ₂ (110)/fcc(111)7x3sqrt3/Ag	-3564.15	-3187.96	-354.01	301.80		
TiO ₂ (110)/fcc(111)7x3sqrt3/Au	-3637.90	-3184.56	-434.55	305.63		
TiO ₂ (110)/fcc(111)7x3sqrt3/Ir	-4285.48	-3165.96	-1094.43	268.13		
TiO ₂ (110)/fcc(111)7x3sqrt3/Os	-4543.25	-3162.50	-1359.01	266.81		
TiO ₂ (110)/fcc(111)7x3sqrt3/Pd	-3863.22	-3179.69	-656.33	274.67		
TiO ₂ (110)/fcc(111)7x3sqrt3/Pt	-3988.05	-3186.11	-777.80	279.18		
TiO ₂ (110)/fcc(111)7x3sqrt3/Rh	-4071.31	-3144.78	-895.65	260.79		
TiO ₂ (110)/fcc(111)7x3sqrt3/Ru	-4291.52	-3137.02	-1121.89	258.56		
ZnO(10 $\bar{1}$ 0)/fcc(100)5x2/Ag	-367.49	-277.91	-81.83	82.97		
ZnO(10 $\bar{1}$ 0)/fcc(100)5x2/Au	-384.44	-276.58	-100.03	84.03		
ZnO(10 $\bar{1}$ 0)/fcc(100)5x2/Cu	-402.20	-285.70	-108.84	63.69		
ZnO(10 $\bar{1}$ 0)/fcc(100)5x2/Ir	-548.95	-286.52	-251.83	73.72		
ZnO(10 $\bar{1}$ 0)/fcc(100)5x2/Ni	-445.00	-281.83	-154.07	60.21		
ZnO(10 $\bar{1}$ 0)/fcc(100)5x2/Os	-606.01	-286.72	-309.06	73.36		
ZnO(10 $\bar{1}$ 0)/fcc(100)5x2/Pd	-447.18	-285.42	-152.37	75.51		
ZnO(10 $\bar{1}$ 0)/fcc(100)5x2/Pt	-473.85	-284.47	-179.21	76.75		
ZnO(10 $\bar{1}$ 0)/fcc(100)5x2/Rh	-504.81	-287.39	-207.22	71.70		
ZnO(10 $\bar{1}$ 0)/fcc(100)5x2/Ru	-554.80	-287.55	-256.22	71.09		
ZnO(10 $\bar{1}$ 0)/fcc(100)6x2/Ag	-459.13	-351.82	-98.04	99.57		
ZnO(10 $\bar{1}$ 0)/fcc(100)6x2/Au	-480.03	-350.47	-120.04	100.83		
ZnO(10 $\bar{1}$ 0)/fcc(100)6x2/Cu	-493.82	-353.44	-130.40	76.43		
ZnO(10 $\bar{1}$ 0)/fcc(100)6x2/Ir	-674.34	-359.15	-301.89	88.46		
ZnO(10 $\bar{1}$ 0)/fcc(100)6x2/Os	-742.71	-359.22	-370.49	88.03		
ZnO(10 $\bar{1}$ 0)/fcc(100)6x2/Pd	-552.88	-358.47	-182.74	90.62		
ZnO(10 $\bar{1}$ 0)/fcc(100)6x2/Pt	-585.62	-357.78	-215.20	92.10		
ZnO(10 $\bar{1}$ 0)/fcc(100)6x2/Rh	-620.74	-359.36	-248.62	86.04		
ZnO(10 $\bar{1}$ 0)/fcc(100)6x2/Ru	-680.65	-359.29	-307.38	85.30		
ZnO(10 $\bar{1}$ 0)/fcc(111)2sqrt3x2/Ag	-285.25	-212.60	-67.40	57.49		
ZnO(10 $\bar{1}$ 0)/fcc(111)2sqrt3x2/Au	-300.07	-211.99	-82.86	58.22		
ZnO(10 $\bar{1}$ 0)/fcc(111)2sqrt3x2/Cu	-304.39	-208.72	-89.64	44.13		
ZnO(10 $\bar{1}$ 0)/fcc(111)2sqrt3x2/Ir	-430.54	-214.91	-208.40	51.07		
ZnO(10 $\bar{1}$ 0)/fcc(111)2sqrt3x2/Ni	-337.23	-203.49	-127.00	41.72		
ZnO(10 $\bar{1}$ 0)/fcc(111)2sqrt3x2/Os	-480.01	-214.87	-258.95	50.82		
ZnO(10 $\bar{1}$ 0)/fcc(111)2sqrt3x2/Pd	-346.99	-214.96	-125.06	52.32		
ZnO(10 $\bar{1}$ 0)/fcc(111)2sqrt3x2/Pt	-370.39	-214.85	-148.24	53.18		
ZnO(10 $\bar{1}$ 0)/fcc(111)2sqrt3x2/Rh	-392.49	-214.53	-170.59	49.67		
ZnO(10 $\bar{1}$ 0)/fcc(111)2sqrt3x2/Ru	-435.37	-214.33	-213.79	49.25		
ZnO(11 $\bar{2}$ 0)/fcc(100)2x2/Ag	-104.18	-68.67	-32.66	33.19		
ZnO(11 $\bar{2}$ 0)/fcc(100)2x2/Au	-111.21	-68.47	-39.96	33.61		
ZnO(11 $\bar{2}$ 0)/fcc(100)2x2/Cu	-114.67	-68.38	-43.48	25.48		

Surface	$E_{\text{Interface}}$	E_{Oxide}	E_{Metal}	Area	N_{OH}	$\Delta\gamma_{\text{ox-lat}}^{\text{ox}}$
ZnO(11 $\bar{2}$ 0)/fcc(100)2x2/Ir	-174.30	-69.60	-100.54	29.49		
ZnO(11 $\bar{2}$ 0)/fcc(100)2x2/Ni	-131.89	-67.14	-61.58	24.09		
ZnO(11 $\bar{2}$ 0)/fcc(100)2x2/Os	-197.50	-69.61	-123.42	29.34		
ZnO(11 $\bar{2}$ 0)/fcc(100)2x2/Pd	-133.93	-69.55	-60.90	30.21		
ZnO(11 $\bar{2}$ 0)/fcc(100)2x2/Pt	-144.85	-69.47	-71.76	30.70		
ZnO(11 $\bar{2}$ 0)/fcc(100)2x2/Rh	-156.27	-69.58	-82.85	28.68		
ZnO(11 $\bar{2}$ 0)/fcc(100)2x2/Ru	-176.72	-69.55	-102.47	28.43		
ZnO(11 $\bar{2}$ 0)/fcc(100)3sqrt2x4sqrt2/Ag	-626.06	-413.22	-196.53	199.14		
ZnO(11 $\bar{2}$ 0)/fcc(100)3sqrt2x4sqrt2/Cu	-687.49	-409.67	-260.97	152.87		
ZnO(11 $\bar{2}$ 0)/fcc(100)3sqrt2x4sqrt2/Ir	-1046.37	-418.15	-603.66	176.92		
ZnO(11 $\bar{2}$ 0)/fcc(100)3sqrt2x4sqrt2/Pd	-804.54	-417.95	-365.31	181.23		
ZnO(11 $\bar{2}$ 0)/fcc(100)3sqrt2x4sqrt2/Pt	-871.45	-417.57	-429.87	184.21		
ZnO(11 $\bar{2}$ 0)/fcc(100)3sqrt2x4sqrt2/Rh	-938.57	-417.82	-497.30	172.08		
ZrO ₂ (101)/fcc(100)7x4/Ag	-2288.87	-2044.13	-229.09	232.33		
ZrO ₂ (101)/fcc(100)7x4/Cu	-2376.37	-2057.80	-304.59	178.34		
ZrO ₂ (101)/fcc(100)7x4/Ir	-2799.18	-2070.05	-704.09	206.40		
ZrO ₂ (101)/fcc(100)7x4/Pd	-2517.29	-2067.45	-426.20	211.44		
ZrO ₂ (101)/fcc(100)7x4/Pt	-2590.35	-2064.62	-501.94	214.91		
ZrO ₂ (101)/fcc(100)7x4/Rh	-2676.26	-2072.10	-580.15	200.76		
ZrO ₂ (101)/fcc(100)7x4/Ru	-2817.53	-2072.29	-717.39	199.04		

Table 9.12: Adhesion energies in $\text{meV}\text{\AA}^2$ with adjusting the metal to the oxide lattice constant $\gamma_{\text{adh}}^{\text{oxide-lattice}}$ for selected metal/oxide interfaces and comparison to the corresponding interfaces in the metal lattice constant $\gamma_{\text{adh}}^{\text{metal-lattice}}$. The change in the adhesion energy $\Delta\gamma_{\text{adh}} = \gamma_{\text{adh}}^{\text{metal-lattice}} - \gamma_{\text{adh}}^{\text{oxide-lattice}}$ in $\text{meV}\text{\AA}^2$. The strain in % is the absolute maximum strain of the metal/oxide interface.

Surface	$\gamma_{\text{adh}}^{\text{oxide-lattice}}$	$\gamma_{\text{adh}}^{\text{metal-lattice}}$	$\Delta\gamma_{\text{adh}}$	Strain
O- α -Al ₂ O ₃ (0001)/fcc(111)sqrt3/Ag	-238.68	-251.77	-13.09	4.22
O- α -Al ₂ O ₃ (0001)/fcc(111)sqrt3/Au	-173.60	-196.95	-23.35	4.89
O- α -Al ₂ O ₃ (0001)/fcc(111)sqrt3/Cu	-289.54	-282.91	6.63	8.69
O- α -Al ₂ O ₃ (0001)/fcc(111)sqrt3/Ir	-406.39	-398.92	7.46	1.75
O- α -Al ₂ O ₃ (0001)/fcc(111)sqrt3/Ni	-358.36	-340.84	17.52	11.22
O- α -Al ₂ O ₃ (0001)/fcc(111)sqrt3/Os	-469.88	-460.47	9.41	0.56
O- α -Al ₂ O ₃ (0001)/fcc(111)sqrt13/Os	-368.46	-373.82	-5.36	1.99
O- α -Al ₂ O ₃ (0001)/fcc(111)sqrt3/Pd	-282.85	-281.49	1.35	0.25
O- α -Al ₂ O ₃ (0001)/fcc(111)sqrt3/Pt	-313.24	-315.45	-2.21	2.01
O- α -Al ₂ O ₃ (0001)/fcc(111)sqrt3/Rh	-379.49	-372.25	7.24	3.11
O- α -Al ₂ O ₃ (0001)/fcc(111)sqrt13/Rh	-339.59	-345.02	-5.43	0.84
O- α -Al ₂ O ₃ (0001)/fcc(111)sqrt3/Ru	-451.45	-441.62	9.83	3.53
O- α -Al ₂ O ₃ (0001)/fcc(111)sqrt13/Ru	-390.18	-392.25	-2.06	0.41
O- α -SiO ₂ (0001)/fcc(111)sqrt3/Ag	-189.01	-190.41	-1.41	0.54
O- α -SiO ₂ (0001)/fcc(111)sqrt3/Au	-142.31	-146.90	-4.59	1.19
O- α -SiO ₂ (0001)/fcc(111)sqrt3/Cu	-267.85	-215.14	52.71	11.91
O- α -SiO ₂ (0001)/fcc(111)2x2/Cu	-238.28	-243.12	-4.84	1.73
O- α -SiO ₂ (0001)/fcc(111)sqrt3/Ir	-250.41	-224.36	26.06	5.22

Surface	$\gamma_{\text{adh}}^{\text{oxide-lattice}}$	$\gamma_{\text{adh}}^{\text{metal-lattice}}$	$\Delta\gamma_{\text{adh}}$	Strain
O- α -SiO ₂ (0001)/fcc(111)sqrt3/Ni	-273.43	-224.61	48.82	14.35
O- α -SiO ₂ (0001)/fcc(111)2x2/Ni	-258.00	-248.07	9.93	1.09
O- α -SiO ₂ (0001)/fcc(111)sqrt3/Os	-277.51	-249.65	27.86	4.07
O- α -SiO ₂ (0001)/fcc(111)sqrt3/Pd	-203.19	-181.82	21.37	3.28
O- α -SiO ₂ (0001)/fcc(111)sqrt3/Pt	-201.32	-184.00	17.32	5.46
O- α -SiO ₂ (0001)/fcc(111)sqrt3/Rh	-244.23	-219.46	24.77	6.53
O- α -SiO ₂ (0001)/fcc(111)sqrt3/Ru	-293.16	-268.43	24.73	6.93
ZnO(11 $\bar{2}$ 0)/fcc(100)2x2/Ag	-79.59	-85.92	-6.33	9.07
ZnO(11 $\bar{2}$ 0)/fcc(100)2x2/Au	-79.26	-82.65	-3.39	9.75
ZnO(11 $\bar{2}$ 0)/fcc(100)2x2/Cu	-118.22	-110.43	7.78	10.99
ZnO(11 $\bar{2}$ 0)/fcc(100)2x2/Ir	-142.76	-140.96	1.80	4.25
ZnO(11 $\bar{2}$ 0)/fcc(100)2x2/Ni	-184.49	-131.61	52.88	13.45
ZnO(11 $\bar{2}$ 0)/fcc(100)2x2/Os	-166.92	-152.48	14.44	4.03
ZnO(11 $\bar{2}$ 0)/fcc(100)2x2/Pd	-114.15	-115.21	-1.06	4.86
ZnO(11 $\bar{2}$ 0)/fcc(100)2x2/Pt	-117.38	-118.03	-0.65	4.50
ZnO(11 $\bar{2}$ 0)/fcc(100)2x2/Rh	-136.27	-134.02	2.25	5.55
ZnO(11 $\bar{2}$ 0)/fcc(100)2x2/Ru	-172.83	-165.09	7.75	5.98
ZnO(10 $\bar{1}$ 0)/fcc(111)2sqrt3x2/Ag	-71.94	-91.34	-19.39	9.07
ZnO(10 $\bar{1}$ 0)/fcc(111)2sqrt3x2/Au	-55.25	-89.60	-34.35	9.75
ZnO(10 $\bar{1}$ 0)/fcc(111)2sqrt3x2/Cu	-106.29	-136.76	-30.47	11.00
ZnO(10 $\bar{1}$ 0)/fcc(111)2sqrt3x2/Ir	-94.15	-141.63	-47.49	4.24
ZnO(10 $\bar{1}$ 0)/fcc(111)2sqrt3x2/Ni	-111.98	-161.54	-49.56	13.46
ZnO(10 $\bar{1}$ 0)/fcc(111)2sqrt3x2/Os	-90.46	-121.79	-31.33	4.03
ZnO(10 $\bar{1}$ 0)/fcc(111)2sqrt3x2/Pd	-83.81	-133.31	-49.50	4.86
ZnO(10 $\bar{1}$ 0)/fcc(111)2sqrt3x2/Pt	-77.60	-137.33	-59.73	4.48
ZnO(10 $\bar{1}$ 0)/fcc(111)2sqrt3x2/Rh	-102.56	-148.25	-45.69	5.56
ZnO(10 $\bar{1}$ 0)/fcc(111)2sqrt3x2/Ru	-109.82	-147.29	-37.47	5.97
TiO ₂ (110)/fcc(100)sqrt5/Ag	-75.94	-84.61	-8.67	8.80
TiO ₂ (110)/fcc(100)sqrt5/Au	-62.31	-70.45	-8.15	9.49
TiO ₂ (110)/fcc(100)sqrt5/Ir	-116.99	-125.37	-8.38	14.09
TiO ₂ (110)/fcc(100)sqrt5/Os	-130.07	-128.57	1.50	16.47
TiO ₂ (110)/fcc(100)sqrt5/Pd	-98.31	-103.32	-5.01	5.69
TiO ₂ (110)/fcc(100)sqrt5/Pt	-88.63	-94.24	-5.61	7.81
TiO ₂ (110)/fcc(100)sqrt5/Rh	-119.96	-126.47	-6.51	8.85
TiO ₂ (110)/fcc(100)sqrt5/Ru	-144.88	-187.68	-42.80	9.24

Table 9.13: Interface energy, oxide energy, metal energy in eV and surface area in Å² for all calculated metal/oxide structures of Table 9.12 with adjusting the metal to the oxide lattice constant. In the case of the hydroxylated oxide, the surface area of the strain-free oxide surface is used and the number of hydroxyl groups per supercell and the stability difference between hydroxylated and oxidized surfaces per supercell given. For the stoichiometric interfaces the surface area depending on the metal lattice constant is given.

Surface	$E_{\text{interface}}$	E_{Oxide}	E_{Metal}	Area	N_{OH}	$\Delta\gamma_{\text{ox-lat}}^{\text{ox}}$
O- α -Al ₂ O ₃ (0001)/fcc(111)sqrt3/Ag	-293.51	-272.58	-34.56	19.85	3	-414.39
O- α -Al ₂ O ₃ (0001)/fcc(111)sqrt3/Au	-300.47	-272.58	-42.81	19.85	3	-414.39

Surface	$E_{\text{interface}}$	E_{Oxide}	E_{Metal}	Area	N_{OH}	$\Delta\gamma_{\text{ox-lat}}^{\text{ox}}$
O- α -Al ₂ O ₃ (0001)/fcc(111)sqrt3/Cu	-304.23	-272.58	-44.27	19.85	3	-414.39
O- α -Al ₂ O ₃ (0001)/fcc(111)sqrt3/Ir	-368.58	-272.58	-106.30	19.85	3	-414.39
O- α -Al ₂ O ₃ (0001)/fcc(111)sqrt3/Ni	-322.51	-272.58	-60.44	19.85	3	-414.39
O- α -Al ₂ O ₃ (0001)/fcc(111)sqrt3/Os	-394.46	-272.58	-130.92	19.85	3	-414.39
O- α -Al ₂ O ₃ (0001)/fcc(111)sqrt13/Os	-1467.20	-1090.38	-421.02	79.38	12	-414.39
O- α -Al ₂ O ₃ (0001)/fcc(111)sqrt3/Pd	-324.04	-272.58	-64.21	19.85	3	-414.39
O- α -Al ₂ O ₃ (0001)/fcc(111)sqrt3/Pt	-336.78	-272.58	-76.34	19.85	3	-414.39
O- α -Al ₂ O ₃ (0001)/fcc(111)sqrt3/Rh	-348.31	-272.58	-86.57	19.85	3	-414.39
O- α -Al ₂ O ₃ (0001)/fcc(111)sqrt13/Rh	-1321.39	-1090.38	-277.51	79.38	12	-414.39
O- α -Al ₂ O ₃ (0001)/fcc(111)sqrt3/Ru	-370.68	-272.58	-107.50	19.85	3	-414.39
O- α -Al ₂ O ₃ (0001)/fcc(111)sqrt13/Ru	-1394.97	-1090.38	-347.07	79.38	12	-414.39
O- α -SiO ₂ (0001)/fcc(111)sqrt3/Ag	-247.62	-221.22	-34.94	21.33	2	-272.03
O- α -SiO ₂ (0001)/fcc(111)sqrt3/Au	-254.48	-221.22	-42.79	21.33	2	-272.03
O- α -SiO ₂ (0001)/fcc(111)sqrt3/Cu	-257.36	-221.22	-42.99	21.33	2	-272.03
O- α -SiO ₂ (0001)/fcc(111)2x2/Cu	-275.51	-221.22	-61.77	21.33	2	-272.03
O- α -SiO ₂ (0001)/fcc(111)sqrt3/Ir	-317.82	-221.22	-103.83	21.33	2	-272.03
O- α -SiO ₂ (0001)/fcc(111)sqrt3/Ni	-274.32	-221.22	-59.83	21.33	2	-272.03
O- α -SiO ₂ (0001)/fcc(111)2x2/Ni	-301.02	-221.22	-86.86	21.33	2	-272.03
O- α -SiO ₂ (0001)/fcc(111)sqrt3/Os	-342.84	-221.22	-128.27	21.33	2	-272.03
O- α -SiO ₂ (0001)/fcc(111)sqrt3/Pd	-276.32	-221.22	-63.34	21.33	2	-272.03
O- α -SiO ₂ (0001)/fcc(111)sqrt3/Pt	-288.03	-221.22	-75.08	21.33	2	-272.03
O- α -SiO ₂ (0001)/fcc(111)sqrt3/Rh	-298.46	-221.22	-84.60	21.33	2	-272.03
O- α -SiO ₂ (0001)/fcc(111)sqrt3/Ru	-320.11	-221.22	-105.20	21.33	2	-272.03
ZnO(1120)/fcc(100)2x2/Ag	-105.78	-69.76	-33.38	33.19		
ZnO(1120)/fcc(100)2x2/Au	-113.44	-69.76	-41.02	33.61		
ZnO(1120)/fcc(100)2x2/Cu	-114.70	-69.76	-41.93	25.48		
ZnO(1120)/fcc(100)2x2/Ir	-173.81	-69.76	-99.84	29.49		
ZnO(1120)/fcc(100)2x2/Ni	-132.29	-69.76	-57.05	24.09		
ZnO(1120)/fcc(100)2x2/Os	-197.41	-69.76	-122.76	29.34		
ZnO(1120)/fcc(100)2x2/Pd	-133.92	-69.76	-60.72	30.21		
ZnO(1120)/fcc(100)2x2/Pt	-145.08	-69.76	-71.71	30.70		
ZnO(1120)/fcc(100)2x2/Rh	-155.72	-69.76	-82.05	28.68		
ZnO(1120)/fcc(100)2x2/Ru	-176.00	-69.76	-101.32	28.43		
ZnO(1010)/fcc(111)2sqrt3x2/Ag	-143.49	-105.72	-33.63	57.49		
ZnO(1010)/fcc(111)2sqrt3x2/Au	-150.78	-105.72	-41.84	58.22		
ZnO(1010)/fcc(111)2sqrt3x2/Cu	-152.09	-105.72	-41.68	44.13		
ZnO(1010)/fcc(111)2sqrt3x2/Ir	-212.39	-105.72	-101.86	51.07		
ZnO(1010)/fcc(111)2sqrt3x2/Ni	-168.68	-105.72	-57.54	41.72		
ZnO(1010)/fcc(111)2sqrt3x2/Os	-237.14	-105.72	-126.82	50.82		
ZnO(1010)/fcc(111)2sqrt3x2/Pd	-171.82	-105.72	-61.71	52.32		
ZnO(1010)/fcc(111)2sqrt3x2/Pt	-182.89	-105.72	-73.05	53.18		
ZnO(1010)/fcc(111)2sqrt3x2/Rh	-193.88	-105.72	-83.07	49.67		
ZnO(1010)/fcc(111)2sqrt3x2/Ru	-215.04	-105.72	-103.92	49.25		
TiO ₂ (110)/fcc(100)sqrt5/Ag	-469.62	-425.61	-40.86	41.49		

Surface	$E_{\text{interface}}$	E_{Oxide}	E_{Metal}	Area	N_{OH}	$\Delta\gamma_{\text{ox-lat}}^{\text{ox}}$
TiO ₂ (110)/fcc(100)sqrt5/Au	-478.73	-425.61	-50.49	42.01		
TiO ₂ (110)/fcc(100)sqrt5/Ir	-553.47	-425.61	-123.54	36.86		
TiO ₂ (110)/fcc(100)sqrt5/Os	-583.47	-425.61	-153.09	36.68		
TiO ₂ (110)/fcc(100)sqrt5/Pd	-504.84	-425.61	-75.52	37.76		
TiO ₂ (110)/fcc(100)sqrt5/Pt	-518.07	-425.61	-89.06	38.38		
TiO ₂ (110)/fcc(100)sqrt5/Rh	-531.39	-425.61	-101.48	35.85		
TiO ₂ (110)/fcc(100)sqrt5/Ru	-556.89	-425.61	-126.13	35.54		

List of Abbreviations

- AFM** atomic force microscopy
- BKL** Bortz–Kalos–Lebowitz
- DFT** density functional theory
- DFT-SAPT** DFT symmetry-adapted perturbation theory
- DSMC** Direct Simulation Monte Carlo
- GGA** generalized gradient approximation
- HF** Hartree-Fock
- kMC** kinetic Monte Carlo
- KS** Kohn-Sham
- LCAO** linear-combination-of-atomic-orbitals
- LDA** local density approximation
- MB** Maxwell-Boltzmann
- OR** Ostwald ripening
- PAW** projector augmented wave
- PD** particle density
- PM** particle migration and coalescence
- PSD** particle size distribution
- SMSI** strong metal support interaction
- STM** scanning tunneling microscopy
- TEM** transmission electron microscopy
- vdW** van-der-Waals
- WC** Wulff construction model

Acknowledgments

First of all I would like to thank Prof. Dr. Felix Studt for the chance to conduct my PhD in his group under his guidance. I would also like to thank him for all his financial support for traveling to present ongoing research at conferences and to visit Prof. Dr. Henrik Grönbeck in Sweden.

My special thanks go to Dr. Philipp Plessow for his major supervision during the last years. Without his knowledge, patience and support this thesis would not had been possible.

I also would like to acknowledge the support by the state of Baden-Württemberg through bwHPC (bwunicluster and JUSTUS, RV bw17D011) and the financial support from the Helmholtz Association.

Many thanks also to the people in my office, Sabrina, Tiago, Michal and Jonas for a good working atmosphere and discussions.

Last but not least I would like to thank my family, especially my partner Jerome, for not only supporting me scientifically by many challenging discussions about DFT and reading this thesis, but also for his mental support over the years.

List of publications

1. Dietze, E. M.; Plessow, P. N., Kinetic Monte Carlo Model for Gas Phase Diffusion in Nanoscopic Systems. *J. Phys. Chem. C* 2018, 122, 21, 11524-11531.
2. Dietze, E. M.; Abild-Pedersen, F.; Plessow, P. N., Comparison of Sintering by Particle Migration and Ripening through First-Principles-Based Simulations. *J. Phys. Chem. C* 2018, 122, 46, 26563-26569.
3. Dietze, E. M.; Plessow, P. N., Predicting the Strength of Metal–Support Interaction with Computational Descriptors for Adhesion Energies. *J. Phys. Chem. C* 2019, 123, 33, 20443-20450.
4. Goodman, E. D.; Johnston-Peck, A. C.; Dietze, E. M.; Wrasman, C. J.; Hoffman, A. S.; Abild-Pedersen, F.; Bare, S. R.; Plessow, P. N.; Cargnello, M., Catalyst deactivation via decomposition into single atoms and the role of metal loading. *Nature Catalysis* 2019, 2, 748-755.
5. Dietze, E. M.; Plessow, P. N.; Studt, F., Modeling the Size-Dependency of the Stability of Metal Nanoparticles. *J. Phys. Chem. C* 2019, 123, 41, 25464-25469.

Eidesstattliche Erklärung

Hiermit versichere ich eidesstattlich, dass ich die hier vorgelegte Dissertation selbstständig angefertigt habe und keine anderen Quellen und Hilfsmittel genutzt habe als die hier angegebenen. Die wörtlich und inhaltlich übernommenen Stellen wurden als solche kenntlich gemacht. Die Regeln zur Sicherung guter wissenschaftlicher Praxis des Karlsruher Instituts für Technologie (KIT) in der gültigen Fassung wurden beachtet und Primärdaten gemäß Abs. A(6) gesichert. Die elektronische Version der Arbeit stimmt mit der schriftlichen überein. Die Arbeit wurde in gleicher oder ähnlicher Form noch keiner anderen Prüfungsbehörde zur Erlangung eines akademischen Grades vorgelegt.

Karlsruhe, den 30.10.2019

Elisabeth M. Dietze